UNIVERSITÀ DEGLI STUDI DI CATANIA

IN CONVENZIONE

UNIVERSITÀ DEGLI STUDI DI PALERMO

DOTTORATO DI RICERCA IN

SCIENZA DEI MATERIALI E NANOTECNOLOGIE
XXX CICLO

FELICIA CAVALERI

PRINTING METHODOLOGIES FOR FUNCTIONAL BIOARRAYS

TUTOR: PROF. BRUNO PIGNATARO

COORDINATORE: PROF.SSA MARIA GRAZIA GRIMALDI

TESI PER IL CONSEGUIMENTO DEL TITOLO DI DOTTORE DI RICERCA

Ad Angelo

Contents

Abstract

In this thesis work, solution dispensing techniques, such as inkjet printing and dip pen nanolithography, have been employed for the realization of high resolution functional bioarrays in order to study intermolecular interactions in confined environments and microarray format.

In particular, inkjet printing was employed for the generation of picoliter-scale aqueous droplets stabilized against evaporation and molecular leakage by oil-confinement with mild surfactants to artificially reproduce scalable *cellular-like* compartments on a chip, realizing specialized small-volume systems to study the behaviour of interacting biomolecules. In this regards we show an unprecedented solution-based protein-binding assay based on arrays of oil-confined water droplets containing protein targets and labelled ligands. Detection of few molecular binding events in these compartments is obtained by employing the advanced fluorescence fluctuation technique Raster Image Correlation Spectroscopy, here employed to probe protein-ligand interactions in artificial aqueous droplets by mapping concentration and diffusion coefficients of fluorolabeled ligands at nanomolar concentrations with a femtoliter scale resolution. RICS was used for the first time to follow molecular dynamics and binding events within confined and scalable artificial single aqueous droplets. We called this new methodology CADRICS for Confined Aqueous Droplet Raster Image Correlation Spectroscopy.

It also described a novel printing approach to produce, for the first time, stable fL-scale aqueous droplets injected inside mineral oil for studying molecular confinement and crowding effects. We printed fL aqueous droplets into oil drops on solid substrates by a "field-free" approach, i.e. in absence of external electric fields and electrolytes, in which we designed a novel actuating waveform by picoliter sized nozzles. Printed fL droplets form an almost-regular circular pattern at the border of mineral oil drops, given their negligible frictional force in mineral oil phase; furthermore, molecules in such fL scale compartments form ring patterns at the surfactant/oil interface due to spontaneous adsorption phenomena at the interface which, bring to molecular concentration at the drop border. At the single droplet level, we show that molecular confinement leads to modify solute-solvent and solvent driven solute-solute interactions, resulting to a decreasing of fluorescence lifetime of environment-sensitive molecular systems, such as Streptavidin-Biotin or FITC dye, but not to a significant increasing of local viscosity-sensitive molecules (CCVJ dye) or environment insensitive dyes (Alexa dyes).

Confinement at ring pattern also leads to molecular crowding, likely due to co-adsorption at the aqueous/oil interface of biomolecules and surfactants. We exploit such confinement process by a model DNA molecular machine, finding out that fluorescence signal switching-on is triggered at lower DNA target concentrations with respect to macrovolumes, thus interaction is favored in confined and crowded conditions.

The final part of the thesis is focused on a strategy for the deposition of single-stranded oligonucleotide sequences on two different solid surfaces, glass and nylon, in form of ordered arrays, through Dip Pen Nanolithography, a contact printing method to dispense drops on femtoliter scale on solid supports. The spot size on micrometer and nanometer scales strictly depends on factors such as time of contact between tip and surface, humidity, and viscosity of molecular ink. The immobilized DNA sequence is succesfully hybridized with a complementary sequence labeled with a fluorophore. The resulting double-strand DNA molecule is suitable as specific molecular recognition substrate for human Topoisomerase.

Introduction

The realization of functional molecular platforms is at the moment one of the top research fields in sectors as physical chemistry of materials, analytical chemistry, bioengineering and pharmaceutical chemistry[1]. In particular, micro- and nano- patterning of biomolecular system with retention of biological activity on surfaces has been particularly investigated in these years.

In general, a bioarray can be defined as a 2D micro-/nano- ordered pattern of biomolecules on the surface of a substrate. Top-down made biological surfaces have profoundly influenced both life sciences and biotechnologies because of their ability to permit a simultaneous, low cost and high sensitivity detection of a large number (hundreds or even thousands) of molecular species in a single experiment[2,3]. Nowadays they are fundamental tools for research in areas as genomics, proteomics, drug screening, lab-on-chip diagnostic, food chemistry, environmental monitoring, forensic investigation, military defence, and so forth[4].

Bioarray fabrication technologies enable the realization of low cost, integrated and complex bio-arrays with high density of reaction sites on surface, requiring extremely small volumes, with respect to conventional assay methodologies, and higher detection sensitivity and throughput screening. Fabrication techniques for biomolecular arrays are typically categorized into top-down and bottom-up approaches. The top-down approach creates micro- or nanoscale structures from a starting biomaterial, whereas the bottom-up approach is based on super-molecular interactions of molecules to self-assemble structures of interest. The most common fabrication techniques are based on top-down approaches such as photolithography, electron beam lithography and focused ion beam lithography: conventional methods commercially available and widely implemented in manufacturing, but often limited by their high cost, difficult multiple-steps processes, and accessibility to the clean room facilities necessary for processing[5].

These limitations motivate the development of new, original unconventional micro- nano-fabrication methods with higher flexibility, ambient condition operations and lower costs, as for example nanoimprint lithography, soft lithography, scanning probe nanolithography (including dip-pen nanolithography). In any case, every bioarray fabrication technique targets the same objective: efficient deposition of uniform, dense arrays of probe molecules with low dispensed reagent consumption, preventing solution contamination and biomolecular damage.

A discriminant for patterning methodologies is constituted by the occurrence of contact between the dispensing device and the receiving surface. In contact printing techniques, a printing device comes in physical contact with the substrate to deposit biological material (e.g., pin printing and dip pen nanopatterning). Instead, in non-contact printing no physical contact between the device and the substrate occurs (e.g., photolithography, ink-jet printing, and laser writing). Moreover, each of these array fabrication techniques can be sub-classified as serial or parallel according to the

patterning strategy. Parallel methods enable the robust large area and high-throughput duplication of a pre-designed and not arbitrarily modifiable pattern on a surface. In serial deposition, serially repeated movements of the printing device permit to create patterns with high resolution and registration however, in principle, with limited fabrication throughput. Recently, it has been demonstrated the feasibility of 2-D cantilever arrays devices for dip pen nanolithography approaches for enabling a robust production of patterned structures over areas as large as square centimetres[6].

A more fundamental discriminant for patterning methodologies is constituted by the attainable lateral resolution. Accordingly, conventional micro- array fabrication techniques as pin printing, thermal or piezoelectric inkjet printing typically permit droplet volumes of 1-10 picoliters, spot resolution of 10-20 micron at the best - based on these resolution biochemical assays at the microscale permit to save time, costs and reagents with respect to established micro-well based assays time and reagent consuming that work with micro- nanoliter scale volumes[7]. Nanoarray based devices would still permit a dramatic further decrease in the cost of the assay since, in comparison to micro-arrays, still less volumes of reagents and analytes are required (down to the atto- liter scale), shorter response times are to be considered and importantly much higher sensitivity can be obtained reaching the sub-femtomolar level. At tens of nanometers patterning resolution, nanoarrays would even enable to probe the activity of biological entities at spots whose lateral dimensions would be the same or one higher order of magnitude compared to the biomolecules typical dimensions. The 10000 to 100000-fold increase in areal density, that could be achieved with the use of nanoscale patterns dispensing techniques (***Figure 1***), would allow an assay to screen for a correspondingly larger number of targets and a fixed number of targets to be screened with a correspondingly smaller sample volume, and in a shorter amount of time[8]. High-resolution patterning would greatly facilitate the development of high-throughput, high-resolution screening tools[2].

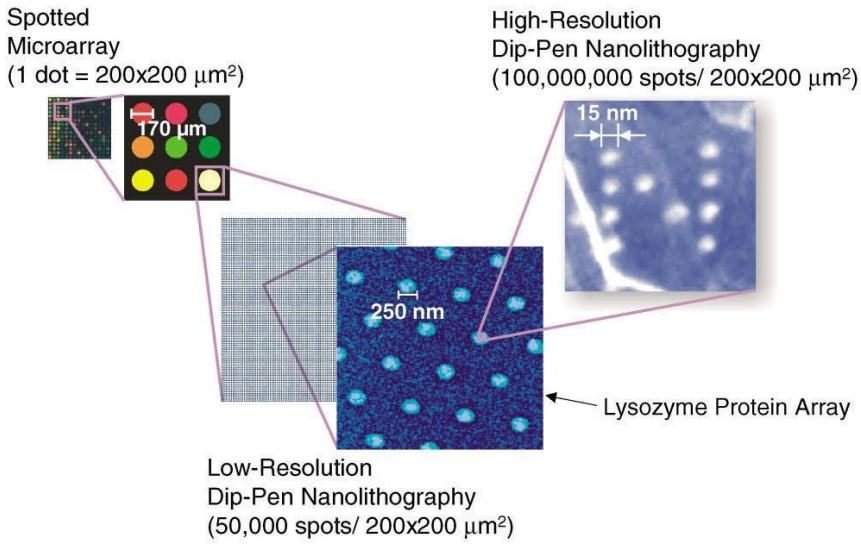

Figure 1: Scheme of the effect of patterning resolution in spot surface density for biological array fabrication[8].

The recent development of confined microreactors[1] in parallel with the field of nanofluidics[10] opens new perspectives in nano-biotechnology, nano-combinatorics and nano-medicine[11]. In this scenario, the realization of miniaturized aqueous compartments is an important challenge giving the opportunity to investigate intermolecular interactions in confined systems to monitor intermolecular and biological events at very low cost as well as to enhance sensing and catalytic properties[12].

On the other side, limiting the dimension of biological fluids and environments can affect the molecular behaviour[13].

Nature has chosen heterogeneous environments to carry out fundamental biochemical processes evolving into compartmentalization of aqueous compartments at the picoliter- and femtoliter scale in order to produce autonomous self-sustaining entities in eukaryotic cells[14]. This finally results in spatial and biochemical compartmentalization in the form of intracellular organelles each one with special tasks and roles[15]. Remarkably, compartmentalization leads to molecular confinement and crowding effects resulting in self-organization of local environments with distinctive properties including the protection of genetic material in the nucleus, the prevention of metabolic intermediates dispersion, the assembly of sub-cellular environments with different features, etc[16,17], given the higher preponderance of interactions with surface wall container[13].

Inspired by nature, molecular self-organization of heterogeneous environments inside artificial compartments[18] or molecular recognition-based stabilization at fluid-fluid interfaces[19] has been shown in picoliter-scale compartments by microfluidic setups or emulsification methods. Hansen et al. recently reported on the possibility to create heterogeneous environments[20] in artificial picoliter scale droplets by crowding. In such droplets, microenvironments of mRNA - translated from DNA

sequences- were stochastically generated since local mRNA since local production rates exceed the diffusion rates of macromolecules. Such heterogeneity leads to higher probability of molecular machinery staying in the same microenvironment, resulting in heterogeneous environments. Spatial confinement of molecules allows for enhanced functionality. Enhanced reactivity and superior stereo selectivities have been shown in confined environments[21]. M. Miyazaki et al.[22] showed that actin filaments are able to self-assemble into a single ring-shaped bundle in a cell-sized confined space in absence of any regulatory signals. The formation of the ring is dependent on volume of the droplet, meaning that if droplet radius is lower than persistence length of actin filaments, then actin filament is able to assembly at the interface with oil phase – this being possible only at femtoliter scale droplets. Folding of DNA G-quadruplexes is facilitated by confinement inside a DNA origami nanocage[23] and DNA walker traversing DNA hairpins confined on scalable microparticles surfaces leads to amplification of miRNA detection[24].

The ability to mimic on a chip such systems by a restricted volume (i.e. producing artificial "cellular-like" compartments) may allow for several scientific and technological breakthroughs through the systematic and statistically[25] significant investigation of intermolecular interactions in variable physiological conditions by modulating several important factors including dimension, pH, ionic strength, interfacial tension, viscosity, etc.[26,20,27–29].

In general, aqueous droplets can be produced by two different groups of methods: active generation in microfluidics setups and printing approaches. Aqueous droplets generation in oil phases by microfluidics can be carried out by electrical, thermal, magnetic, mechanical triggering[30] and has enabled an enormous amount of applications ranging from diagnostic to drug discovery[31]. In comparison with microfluidics setups, printing methods – such as pin printing, inkjet printing, pyroelectrodynamic printing, dip pen nanolithography - allow for higher simplicity and versatility having precise control on droplet volumes and composition[32] and have been applied to the production of biochips for various applications ranging from drug discovery to single cell studies and tissue engineering[33]. Among all printing approaches, inkjet printing constitutes an ideal fabrication tool for programmable confined aqueous compartments, since it enables biological materials to be printed at low cost and low consumption on solid or soft surfaces at speeds up to 2 orders of magnitude faster (10 spots/s) in comparison to conventional printing techniques, such as pin printing[7] with high positional accuracy and control of spot morphology. Remarkably, a careful optimization of the jetting parameters is usually needed in order to match with the printable ink properties and retain biological activity of the dispensed molecules[34]. The development of protein[35] or small molecules[36] microarrays - fabricated by printing methods - allows for high-throughput investigation of biomolecular interactions up to the single cell level[37–39]. The most of setups in conventional bioarrays are built in such a way that proteins and ligands are immobilized at solid supports[7], so that their structure could be affected by denaturation or conformational changes

compromising the specificity of molecular interactions[40]. Recently, droplets microarrays fabrication methods have permitted the realization of high-density, low volume (nanoliter up to femtoliter) solution phase assays[33,41–44]. These set-ups may allow recreating biological native conditions given that molecular interactions occur in solution phase and not at the solid/liquid interface. However, at these small scales, evaporation constitutes a predominant issue and high-boiling viscous additives such as glycerol have to be added to realize stable micro-compartments, as reported in the LUMDA chip[43] in which glycerol-rich liquid spots are assembled by sequentially printing different biomolecular components. However, glycerol drastically reduces protein dynamic behaviour in droplet and leads to slightly different results between macroscopic volumes and droplets arrays. In order to get evaporation-free microenvironments with a native-like nature, some experimental and theoretical studies dealt with injecting picoliter water-rich droplets in an oil phase[45,46]. However, these devices suffer from lack of control over oil-water interface along with high consumptions of biomolecules (millimolar concentrations)[26].

In general, ligand-protein binding assays[47,48] can be executed at solid-liquid interface by methods as different as radio ligand assays[49], surface plasmon resonance[50], protein microarrays[51] - or at aqueous liquid phase by methods such as fluorescence polarization[52], fluorescence anisotropy[53], nuclear magnetic resonance[54], mass spectrometry[55], isothermal titration calorimetry[56] and differential scanning calorimetry[57]. Notably, among the approaches that can be used to monitor reactions occurring in small volumes (nanoliter to picoliter volume), fluorescence-based methods have large advantages as they are non-invasive and are characterised by high sensitivity and specificity, enabling up to single-molecule detection[58]. Notably, the specific fluorescence method can be selected on the ground of the system properties and on the feature to be investigated.

In this thesis work, solution dispensing techniques, such as Inkjet printing and Dip Pen Nanolithography, have been employed to fabricate miniaturized devices suitable for intermolecular interactions studies.

We exploit inkjet printing to develop aqueous droplet arrays mimicking on a chip the basic nature of “cellular-like” compartments. Detection of few molecular binding events in these compartments is obtained by employing advanced fluorescence fluctuation techniques. In particular, Raster Image Correlation Spectroscopy (RICS) is here employed to probe protein-ligand interactions in artificial aqueous droplets with a femtoliter scale resolution at a nanomolar concentration. This method was designed to detect and quantify molecular dynamics in living cells, such as binding, concentration and diffusion properties of molecules diffusing in cytoplasm or in cellular compartments and gives information on dynamical events in each pixel also providing information on their location within the image[59,60,61]. In this scenario, RICS represents an ideal transduction method for monitoring molecular binding events in pico- to nano-liter volume droplets.

Droplets by inkjet printing are normally up to picoliter scale, being droplet size dependent on the

nozzle size, which is typically not below 10 μm. Recent approaches show the possibility to reduce droplets volume down to the attoliter scale by <10 μm nozzle radius[62] or by electric field aided hydrodynamically dispensing[63], however these approaches respectively can cause nozzle clogging or require electrolyte media support in the solution. Here we show a novel actuating waveform that permits to assemble fL aqueous droplets from 10 μm size nozzles, by a "field-free" piezoelectric inkjet. This approach permits to execute molecular confinement on model biomolecular systems and DNA molecular machines at the border of aqueous fL drops in presence of crowding. We investigated the effects of molecular confinement and crowding on DNA nanomachines, a combination which is still not so highly explored in DNA nanotechnology. Coupling of molecular crowding and confinement is investigated by fluorescence life time imaging (FLIM) on probe molecules, giving information on the fluorescence lifetime, that measures the exponential decay rate of a fluorophore from the its excited state to the radiative fluorescence emission.[64]

Finally, a DPN methodology for the realization of low cost biochips on cheap and flexible substrate, that could be a suitable solution for "Point-of-care" diagnosis, is reported. The first step for prevention and treatment of diseases is, indeed, the accurate diagnosis. However, proper diagnostic technologies are not available in developing countries due to the lack of reliable electrical power, refrigeration and trained personnel. For this reason, there is an urgent need of low cost, rapid assays not requiring any external support. By coupling such technologies to communication infrastructures, healthcare in areas without access to medical personnel would be possible. Flexible substrates like paper and nylon, are ideal for fabricating such devices since they are cheap, easy to degradate after use and compatible with most of existing printing technologies[65]. It was shown the possibility to efficiently deposit oligonucleotides by Dip Pen Nanolithography (DPN) onto glass surfaces[66]. In this thesis work is also reported a general methodology to deposite and anchor single-stranded oligonucleotides by DPN on two different solid surfaces, glass and nylon, in form of ordered arrays, useful for point-of-care diagnostic chips fabrication.

In order to facilitate the reading of this thesis, the work has been divided in three parts: the State of the Art, a General Part and the Experimental Part.

The first Part, Chapter 1, regards the state of the art of Microarray Applications in Life Science, with a first section focusing on High-Throughput Screening Methodologies and a second section on patterning methodologies with the different approaches of contact printing and non contact printing. The second Part is composed of two chapters. Chapter 2 gives general notions concerning Biopatterning Fabrication Methodologies at the micro- and nano-scale, with particular regard on Inkjet Printing and Dip Pen Nanolithography. Chapter 3 deals with Confocal Microscopy Detection Techniques; in particular Raster Image Correlation Spectroscopy (RICS) and Fluorescence Lifetime Imaging Microscopy (FLIM) are considered and discussed in detail.

The final Part concerns the Experimental Section of the thesis and consists of three chapters. Chapter 4 presents CADRICS methodology for the realization of bioarrays of small volume confined compartments for monitoring few molecular binding events by combining Inkjet Printing with Raster Image Correlation Spectroscopy. Chapter 5 shows a novel printing approach to produce stable fL-scale aqueous droplets inside mineral oil by picoliter-scale nozzles and in absence of external electrical fields. Inside these compartments is possible to study confinement and crowding effects on molecular systems. Chapter 6 describes the experimental procedure to realize by Dip Pen Nanolithography biochips of oligonucleotides on glass and on cheap and flexible substrate, such a nylon.

Each of these chapters provides information about materials, surface functionalization, patterning methodologies and investigation tools employed, finally providing a broad discussion concerning the obtained experimental results. Bibliography is provided at the end of each chapter. Finally, Conclusions and Acknowledgments are given.

Bibliography

1. Pignataro, B. Nanostructured molecular surfaces: advances in investigation and patterning tools. *J. Mater. Chem.* **19,** 3338–3350 (2009).
2. Hong, J., Edel, J. B. & deMello, A. J. Micro- and nanofluidic systems for high-throughput biological screening. *Drug Discov. Today* **14,** 134–146 (2009).
3. Ogaki, R., Alexander, M. & Kingshott, P. Chemical patterning in biointerface science. *Mater. Today* **13,** 22–35 (2010).
4. Albala, J. S. & Humpheiy-Smith, I. *Protein Arrays, Biochips, and Proteomics: The Next Phase of Genomic Discovery*. (Marcel Dekker, 2003).
5. Kim, S. M. & Suh, K. Y. Fabrication of biological arrays by unconventional lithographic methods. in *Frontiers in bioscience (Scholar edition)* 406–419 (2009).
6. Haaheim, J. R., Tevaarwerk, E. R., Fragala, J. & Shile, R. Dip Pen Nanolithography: a maturing technology for high-throughput flexible nanopatterning. in *Micro (MEMS) and Nanotechnologies for Defense and Security* (2007).
7. Arrabito, G. & Pignataro, B. Inkjet printing methodologies for drug screening. *Anal. Chem.* **82,** 3104–3107 (2010).
8. Ginger, D. S., Zhang, H. & Mirkin, C. A. The Evolution of Dip-Pen Nanolithography. *Angew. Chemie Int. Ed.* **43,** 30–45 (2004).
9. Elani, Y., Law, R. V & Ces, O. Vesicle-based artificial cells as chemical microreactors with spatially segregated reaction pathways. *Nat Commun* **5,** (2014).
10. Bocquet, L. & Charlaix, E. Nanofluidics, from bulk to interfaces. *Chem. Soc. Rev.* **39,** 1073–1095 (2010).
11. Riehemann, K. *et al.* Nanomedicine—Challenge and Perspectives. *Angew. Chemie Int. Ed.* **48,** 872–897 (2009).
12. Fabiano, S. & Pignataro, B. Selecting speed-dependent pathways for a programmable nanoscale texture by wet interfaces. *Chem. Soc. Rev.* **41,** 6859–6873 (2012).
13. Huan-Xiang Zhou,1 Germán Rivas, 2 and Allen P. Minton. Macromolecular Crowding and Confinement: Biochemical, Biophysical, and Potential Physiological Consequences. *Annu. Rev. Biophys.* **37,** 375–397 (2008).
14. Urban, P. L. Compartmentalised chemistry: from studies on the origin of life to engineered biochemical systems. *New J. Chem.* **38,** 5135–5141 (2014).
15. Rabe, K. S., Müller, J., Skoupi, M. & Niemeyer, C. M. Cascades in Compartments: En Route to Machine-Assisted Biotechnology. *Angew. Chemie Int. Ed.* **56,** 13574–13589 (2017).
16. Agapakis, C. M., Boyle, P. M. & Silver, P. A. Natural strategies for the spatial optimization of metabolism in synthetic biology. *Nat Chem Biol* **8,** 527–535 (2012).
17. Gorris, H. H. & Walt, D. R. Analytical Chemistry on the Femtoliter Scale. *Angew. Chemie Int. Ed.* **49,** 3880–3895 (2010).
18. Numata, M., Takigami, Y., Hirose, N. & Sakai, R. Two-dimensional self-assembly of amphiphilic porphyrins on a dynamically shrinking droplet surface. *Org. Biomol. Chem.* **12,** 1627–1632 (2014).

19. Maeda, Y., Wei, Z. & Matsui, H. Biomimetic Assembly of Proteins into Microcapsules on Oil-in-Water Droplets with Structural Reinforcement via Biomolecular-Recognition-Based Cross-Linking of Surface Peptides. *Small* **8,** 1341–1344 (2012).

20. Hansen, M. M. K. *et al.* Macromolecular crowding creates heterogeneous environments of gene expression in picolitre droplets. *Nat Nano* **11,** 191–197 (2016).

21. Dixon, C., Lamanna, J. & Wheeler, A. R. Printed Microfluidics. *Adv. Funct. Mater.* **27,** n/a-n/a (2017).

22. Miyazaki, M., Chiba, M., Eguchi, H., Ohki, T. & Ishiwata, S. Cell-sized spherical confinement induces the spontaneous formation of contractile actomyosin rings in vitro. *Nat Cell Biol* **17,** 480–489 (2015).

23. Shrestha, P. *et al.* Confined space facilitates G-quadruplex formation. *Nat Nano* **12,** 582–588 (2017).

24. JungC., B., A. & D., E. A stochastic DNA walker that traverses a microparticle surface. *Nat Nano* **11,** 157–163 (2016).

25. Weinmeister, R., Freeman, E., Eperon, I. C., Stuart, A. M. & Hudson, A. J. Single-Fluorophore Detection in Femtoliter Droplets Generated by Flow Focusing. *ACS Nano* **9,** 9718–9730 (2015).

26. Tu, Y. *et al.* Mimicking the Cell: Bio-Inspired Functions of Supramolecular Assemblies. *Chem. Rev.* **116,** 2023–2078 (2016).

27. Hansen, M. M. K. *et al.* Cell-Like Nanostructured Environments Alter Diffusion and Reaction Kinetics in Cell-Free Gene Expression. *ChemBioChem* **17,** 228–232 (2016).

28. Lentini, R., Yeh Martín, N. & Mansy, S. S. Communicating artificial cells. *Curr. Opin. Chem. Biol.* **34,** 53–61 (2016).

29. Kuchler, A., Yoshimoto, M., Luginbuhl, S., Mavelli, F. & Walde, P. Enzymatic reactions in confined environments. *Nat Nano* **11,** 409–420 (2016).

30. Chong, Z. Z. *et al.* Active droplet generation in microfluidics. *Lab Chip* **16,** 35–58 (2016).

31. Holmes, D. & Gawad, S. The Application of Microfluidics in Biology BT - Microengineering in Biotechnology. in (eds. Hughes, P. M. & Hoettges, F. K.) 55–80 (Humana Press, 2010). doi:10.1007/978-1-60327-106-6_2

32. Gudapati, H., Dey, M. & Ozbolat, I. A comprehensive review on droplet-based bioprinting: Past, present and future. *Biomaterials* **102,** 20–42 (2016).

33. Arrabito, G. & Pignataro, B. Solution Processed Micro- and Nano-Bioarrays for Multiplexed Biosensing. *Anal. Chem.* **84,** 5450–62 (2012).

34. Arrabito, G. *et al.* On the relationship between jetted inks and printed biopatterns: molecular-thin functional microarrays of glucose oxidase. *Langmuir Acs J. Surfaces Colloids* **25,** 6312–6318 (2009).

35. Templin, M. F. *et al.* Protein microarray technology. *Trends Biotechnol.* **20,** 160–166 (2002).

36. Ma, H. & Horiuchi, K. Y. Chemical microarray: a new tool for drug screening and discovery. *Drug Discov. Today* **11,** 661–668 (2006).

37. Sekula, S. *et al.* Multiplexed Lipid Dip-Pen Nanolithography on Subcellular Scales for the Templating of Functional Proteins and Cell Culture. *Small* **4,** 1785–1793 (2008).

38. Gandor, S. *et al.* A Protein-Interaction Array Inside a Living Cell. *Angew. Chemie Int. Ed.* **52,** 4790–4794 (2013).

39. Kusi-Appiah, A. E., Vafai, N., Cranfill, P. J., Davidson, M. W. & Lenhert, S. Lipid multilayer microarrays for in vitro liposomal drug delivery and screening. *Biomaterials* **33,** 4187–4194 (2012).

40. Zenobi, R. Single-Cell Metabolomics: Analytical and Biological Perspectives. *Science (80-.).* **342,** (2013).

41. Ueda, E., Geyer, F. L., Nedashkivska, V. & Levkin, P. A. DropletMicroarray: facile formation of arrays of microdroplets and hydrogel micropads for cell screening applications. *Lab Chip* **12,** 5218–5224 (2012).

42. Burchak, O. N., Mugherli, L., Ostuni, M., Lacapère, J. J. & Balakirev, M. Y. Combinatorial Discovery of Fluorescent Pharmacophores by Multicomponent Reactions in Droplet Arrays. *J. Am. Chem. Soc.* **133,** 10058–10061 (2011).

43. Arrabito, G., Galati, C., Castellano, S. & Pignataro, B. Luminometric sub-nanoliter droplet-to-droplet array (LUMDA) and its application to drug screening by phase I metabolism enzymes. *Lab Chip* **13,** 68–72 (2013).

44. Bao, B. *et al.* Patterning liquids on inkjet-imprinted surfaces with highly adhesive superhydrophobicity. *Nanoscale* **8,** 9556–9562 (2016).

45. Sun, Y., Chen, X., Zhou, X., Zhu, J. & Yu, Y. Droplet-in-oil array for picoliter-scale analysis based on sequential inkjet printing. *Lab Chip* **15,** 2429–2436 (2015).

46. Chen, X., Sun, Y., Xue, C., Yu, Y. & Hu, G. On the Successful Encapsulation of Water Droplets into Oil Droplets. *Procedia Eng.* **126,** 725–729 (2015).

47. Du, X. *et al.* Insights into Protein–Ligand Interactions: Mechanisms, Models, and Methods. *International Journal of Molecular Sciences* **17,** (2016).

48. Stockwell, B. R. Exploring biology with small organic molecules. *Nature* **432,** 846–854 (2004).

49. Maguire, J. J., Kuc, R. E. & Davenport, A. P. Radioligand Binding Assays and Their Analysis BT - Receptor Binding Techniques. in (ed. Davenport, P. A.) 31–77 (Humana Press, 2012). doi:10.1007/978-1-61779-909-9_3

50. Frostell, Å., Vinterbäck, L. & Sjöbom, H. Protein–Ligand Interactions Using SPR Systems BT - Protein-Ligand Interactions: Methods and Applications. in (eds. Williams, A. M. & Daviter, T.) 139–165 (Humana Press, 2013). doi:10.1007/978-1-62703-398-5_6

51. Sun, H., Chen, G. Y. J. & Yao, S. Q. Recent Advances in Microarray Technologies for Proteomics. *Chem. Biol.* **20,** 685–699 (2013).

52. Rossi, A. M. & Taylor, C. W. Analysis of protein-ligand interactions by fluorescence polarization. *Nat. Protoc.* **6,** 365–387 (2011).

53. Coussens, M. D. H. and A. Y. and T. P. and J. C. B. and A. J. and A. S. and N. P. Fluorescence polarization assays in high-throughput screening and drug discovery: a review. *Methods Appl. Fluoresc.* **4,** 22001 (2016).

54. Goldflam, M., Tarragó, T., Gairí, M. & Giralt, E. NMR Studies of Protein–Ligand Interactions BT - Protein NMR Techniques. in *Protein NMR Techniques* (eds. Shekhtman, A. & Burz, S. D.) 233–259 (Humana Press, 2012). doi:10.1007/978-1-61779-480-3_14

55. Ojanperä, I., Kolmonen, M. & Pelander, A. Current use of high-resolution mass

spectrometry in drug screening relevant to clinical and forensic toxicology and doping control. *Anal. Bioanal. Chem.* **403,** 1203–1220 (2012).

56. Freyer, M. W. & Lewis, E. A. Isothermal Titration Calorimetry: Experimental Design, Data Analysis, and Probing Macromolecule/Ligand Binding and Kinetic Interactions. in *Biophysical Tools for Biologists, Volume One: In Vitro Techniques* (ed. Biology, B. T.-M. in C.) **Volume 84,** 79–113 (Academic Press, 2008).

57. Chiu, M. & Prenner, E. Differential scanning calorimetry: An invaluable tool for a detailed thermodynamic characterization of macromolecules and their interactions. *J. Pharm. Bioallied Sci.* **3,** 39–59 (2011).

58. Joo, C., Balci, H., Ishitsuka, Y., Buranachai, C. & Ha, T. Advances in Single-Molecule Fluorescence Methods for Molecular Biology. *Annu. Rev. Biochem.* **77,** 51–76 (2008).

59. Digman, M. A. *et al.* Measuring Fast Dynamics in Solutions and Cells with a Laser Scanning Microscope. *Biophys. J.* **89,** 1317–1327 (2005).

60. Rossow, M. J., Sasaki, J. M., Digman, M. A. & Gratton, E. Raster image correlation spectroscopy in live cells. *Nat. Protoc.* **5,** 1761–1774 (2010).

61. Brown, C. M. *et al.* Raster image correlation spectroscopy (RICS) for measuring fast protein dynamics and concentrations with a commercial laser scanning confocal microscope. *J. Microsc.* **229,** 78–91 (2008).

62. Sekitani, T., Noguchi, Y., Zschieschang, U., Klauk, H. & Someya, T. Organic transistors manufactured using inkjet technology with subfemtoliter accuracy. *Proc. Natl. Acad. Sci.* **105,** 4976–4980 (2008).

63. Zhang, Y., Zhu, B., Liu, Y. & Wittstock, G. Hydrodynamic dispensing and electrical manipulation of attolitre droplets. *Nat. Commun.* **7,** 12424 (2016).

64. Berezin, M. Y. & Achilefu, S. Fluorescence Lifetime Measurements and Biological Imaging. *Chem. Rev.* **110,** 2641–2684 (2010).

65. Martinez, A. W., Phillips, S. T., Whitesides, G. M. & Carrilho, E. Diagnostics for the Developing World: Microfluidic Paper-Based Analytical Devices. *Anal. Chem.* **82,** 3–10 (2010).

66. Arrabito, G. *et al.* Biochips for Cell Biology by Combined Dip-Pen Nanolithography and DNA-Directed Protein Immobilization. *Small* **9,** 4243–4249 (2013).

I State of the Art

1 Microarrays Applications in Life Science

This chapter deals with the applications of micro- and nano- array technology in relevant fields of Life Sciences. The realization of high-speed, miniaturized, low-cost, and high throughput biological devices in the microarray format is a very important issue today due to its importance in fields as biosensing, drug screening, environmental monitoring, forensic investigation, military defence and so forth. Recently developed micropatterning techniques allow for high-throughput production of patterned multiplexed biological materials without the use of masks, stamps, ribbons, or other costly and time-consuming conventional processing equipment, like the ones considered in soft lithography techniques.

Nowadays one of the most outstanding fields of application for microarrays methodologies is the drug screening, an essential part of drug discovery process. Drug discovery is "a complex learning process whereby research efforts are directed toward assimilating new knowledge to create and develop a drug with specific therapeutic effects"[1]. The process can roughly be divided into an early and late phase. The early phase is mainly represented by target selection and lead discovery, whereas the later phase deals mainly with clinical evaluation and development (**Fig. 1.1**). Considering early phase drug discovery, target discovery, (targets are protein biomolecules such as receptors, enzymes and ion channels whose modulation can lead to effective disease treatment), consists in the identification and validation of suitable drug targets for therapeutic intervention[2], while lead discovery is the identification of novel chemical molecules that act on those targets through the employment of high-throughput screening (HTS) methodologies.

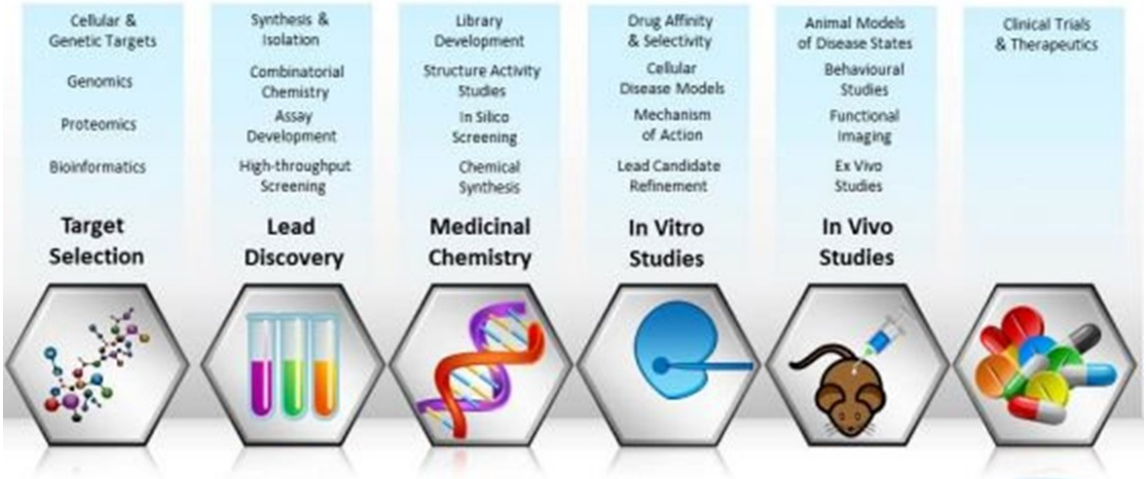

Figure 1.1: Phases of drug discovery and development

Drug discovery process is today critically dependent upon the ability to identify chemical compounds ("hits") acting on specific targets, that is drug screening is one of the bottlenecks in the process of drug discovery. Many new possible drug targets are discovered every day thanks to genomics and proteomics researches, while new chemical compounds are daily synthesized by high-throughput synthesis. So, there is an urgent need to find high throughput screening (HTS) methodologies to profile the activity of large numbers of chemicals against hundreds of biological targets in a fast, low-cost fashion.

The recent development of microarray and microfluidic technologies has permitted the development of high-density, low volume assays to achieve this goal. In particular, the reduction in cost, rather than increase in throughput, is the primary driving force within most HTS groups to move to higher density, lower volume assays[3–5].

1.1 High-Throughput Screening Methodologies

With many possible drug targets discovered every day and new chemical compounds synthesized daily by drug companies, the lead identification has become more dependent upon the enabling technologies of screening and identifying the lead compounds. There is an urgent need to find new ways to profile the activity of large numbers of chemicals against hundreds of biological targets in a fast, low-cost fashion. Robust, rapid, low-cost, sensitive, miniaturized and efficient high-throughput screening methods are required to examine a huge number of initial candidates and thus minimize the attrition of chemical entities in the costly clinical phase of drug development.

These requirements have strongly encouraged the advancement and the development of high-throughput screening technologies. To further increase the throughput and reduce the cost of chemicals and targets, the miniaturization and low-cost preparation of biological assays have been the trend in today's array development and laboratory automation. These demands have encouraged the advancement of microplate-based HTS technologies including small molecules library design and assembly, robotics, assay development and data handling. Today, libraries containing millions of compounds are routinely screened with single compounds of high purity in 384-, 1536-, 3456-well formats[6].

Modern microchip technologies offer other platforms for HTS, such as microarrays and microfluidics devices that permit to exploit miniaturized and ultrasensitive assays. Microarrays are composed of biomolecules attached to a surface in defined locations. They permit the simultaneous analysis of thousands of chemical compounds within a single experimental step and have become popular tools in drug discovery and life science research. Biomolecules commonly immobilized on microarrays include oligonucleotides, polymerase chain reaction products, proteins, lipids, peptides. The success of microarrays technology in genomic and proteomic research has given new

impetus to miniaturization, providing unprecedented capabilities for parallel functional analyses of hundred or even thousands of bioentities. During the past few years, a variety of chemical compound microarrays and protein microarrays (biochips) with different surface chemistries and activation strategies have emerged[7]. On the other hand, microfluidic devices perform screening assays in a continuous fashion. These devices require a series of mechanical components (i.e. pumps, mixers, valves etc.) for introducing reagents and samples, moving fluids within a microchannel network, combining and mixing reactants.

1.1.1 Chemical compound microarrays

Chemical microarrays, (also called small-molecule microarrays), are devices composed of different chemical compounds arrayed on a surface[8]. They are capable of evaluating the activity of a large number of chemical structures against hundreds of biological targets (**Fig. 1.2**).

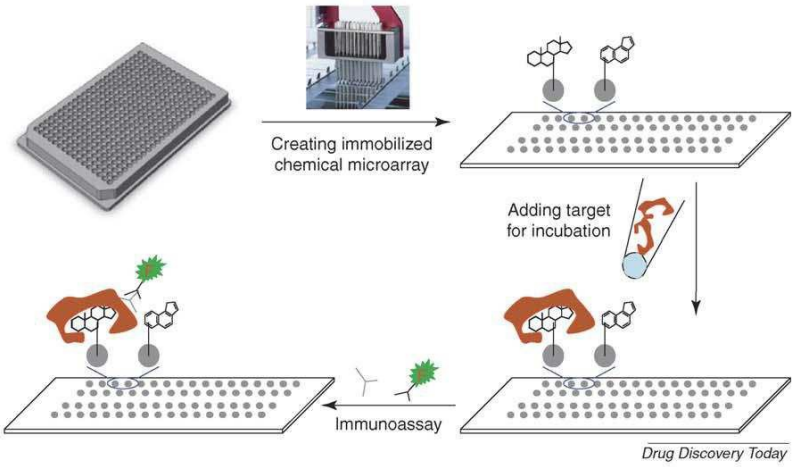

Figure 1.2: Example of small molecule microarray. Chemical compounds synthesized with the same linking functional group are arrayed and covalently immobilized on the surface of microarray chips. Biological targets are added to the chip, this is followed by several washing steps to eliminate non-specific binding. The compounds that bind to the target with high affinity are then identified by immunoassays.

The development of these devices has been a slow process. One of the major problems for their development is that compounds with different structures and properties are screened in a solution phase, and individual reactions need to be isolated in wells. When reactions are reduced to microarray size, no automatic liquid handling system can process these reactions individually, separately and sequentially if each reaction is still kept in a solution phase. Therefore, chemical microarray technology, which directly links chemicals to the chip surface, was introduced[9]. However, compared with DNA and protein microarray technologies, no general linking chemistry can be established to immobilize compounds having different structures and functional groups on the same chip surface. To avoid the potential complicated immobilization process, microarrays

with dry compounds have been developed. This technology can deposit any chemical compound library on the same chip surface in a dry form. However, different compounds possessing different dissolution rates can create problems with reaction uniformity and endpoint data comparison. Given that there are > 10^{40} potential low molecular weight chemical compounds available in theory, one might imagine that many difficulties could be encountered with the approaches outlined above. To avoid these problems, a new solution-phase chemical compound microarray has been created. In this format each compound is individually arrayed on a glass surface - with a reaction buffer containing a low concentration of glycerol to prevent evaporation. Therefore, as in conventional well-based screening, the chemical compounds and biological targets are always in reaction solutions, which are activated with biological targets by delivering analytes using non-contact deposition technology. With this approach all compounds and peptide libraries can be microarrayed, and activated by biological targets in the form of pure protein or cell lysate. By performing assays in solution, the enzyme reaction can be performed in a more native-like environment, and the proteins will retain their native structure and activity. Each microarray spot acts as an individual reaction center. Since reactions take place in homogeneous environments, it is possible to extract kinetic parameters such as K_m, V_{max}, and k_{cat}. In fact, these microarray-generated parameters were quantitatively similar to those derived from well-based assays. Furthermore, taking advantage of miniaturization pays off in larger scale HTS: the total cost of microarray-based reactions could be significantly reduced compared with standard low volume 384-well-based assays[10].

1.1.2 Protein microarrays

Protein microarrays are devices realized by arraying proteins onto a surface; they have emerged as a promising approach for a wide variety of applications including the study of protein-protein, protein-small molecule, enzyme-substrate, and antibody-antigen interactions[11].

Three types of protein microarrays are currently used to study the biochemical activities of proteins: analytical microarrays, functional microarrays, and reverse phase microarrays. Analytical microarrays are typically used to profile a complex mixture of proteins in order to measure binding affinities and protein expression levels of the proteins in the mixture. In this technique, a library of antibodies, aptamers, or affibodies is arrayed on a glass microscope slide. The array is then probed with a protein solution. Antibody microarrays are the most common analytical microarray and can be used to monitor differential expression profiles and for clinical diagnostics. Functional protein microarrays are different from analytical arrays and are composed of arrays containing full-length functional proteins or protein domains. These protein chips are used to study the biochemical activities of an entire proteome in a single experiment. They are used to study numerous protein interactions, such as protein-protein, protein-DNA, and protein-RNA interactions. A third type of

protein microarray, related to analytical microarrays, is known as a reverse phase protein microarray (RPA). In RPA, cells are isolated from various tissues of interest and are lysed. The lysate is arrayed onto a nitrocellulose slide using a contact pin microarrayer. The slides are then probed with antibodies against the target protein of interest, and the antibodies are typically detected with chemiluminescent, fluorescent, or colorimetric assays. Reference peptides are printed on the slides to allow for protein quantification of the sample lysates.

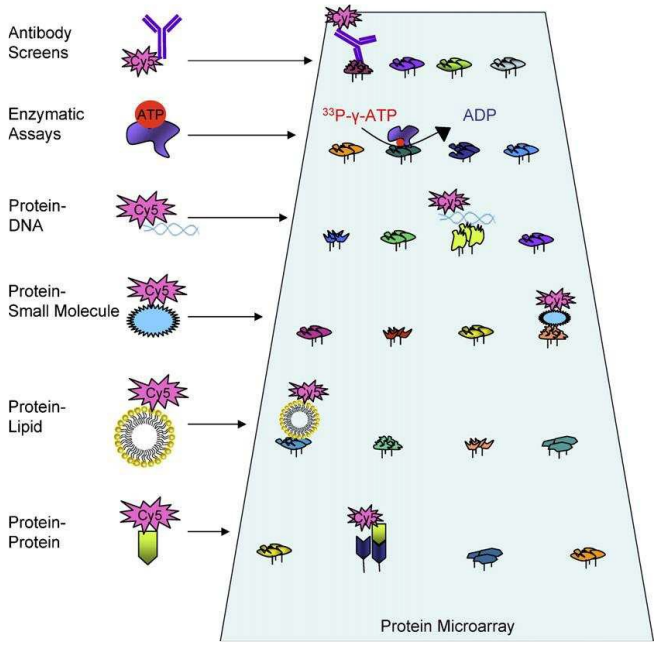

Figure 1.3: Representative samples of the different assays performed on functional protein microarrays are shown. Proteins are immobilized at high spatial density onto a surface. While Cy5 is the fluorophore shown, many other fluorophores can be used for detection[12].

The ability of protein biochips for identification and characterization of entire interconnecting protein pathways and networks in cells gives the possibility to expand the comprehension of physiological processes and essential diseases mechanisms so leading to the rational and speed identification of new drugs and drug targets. The critical need for more rapid identification of novel drug targets, and for obtaining high-quality information early in the target validation process is a major driver for the pharmaceutic industry. This technology could become a fundamental tool for the analysis of cell physiology as a set of linked networks and has the potential to lead to a systematic approach that is capable of assessing rapidly and in parallel the state of each component in the network.

Compared to DNA microarrays, protein array technologies have additional challenges with the image analysis, primarily due to both low signal-to-noise ratio and limited number of abundant protein signal spots to align grids. A protein array image usually consists of one or multiple blocks of arrays.

The variety of array formats, spot shapes, and intensity profiles makes it quite challenging to extract spot signal correctly. In addition, the different substrates, printing mechanisms and protocols, staining/blocking processes, and broad applications result in varied kinds of complex images which make it difficult to develop an algorithm to be applied to all scenarios.

Proteome microarrays are an excellent way to discover drug targets. The rate of drug development can be accelerated by screening potential drug candidates against their putative protein targets, while at the same time, ensuring that the candidates exhibit no cross-reactivity with secondary proteins.

Microarrays can be used for screening small molecule binders to protein targets while simultaneously analysing its binding to other cellular proteins that may be structurally and functionally related to the protein of interest. Entire proteomes printed on a chip can be probed with small molecules in one experiment to discover interactions. Fundamental issues in protein chips fabrication are: substrate surface preparation, protein handling, detection methods and data acquisition.

Proteins can be attached to various kinds of surfaces via diffusion, adsorption/absorption, covalent bonding and affinity interactions (**Fig.1.4**).

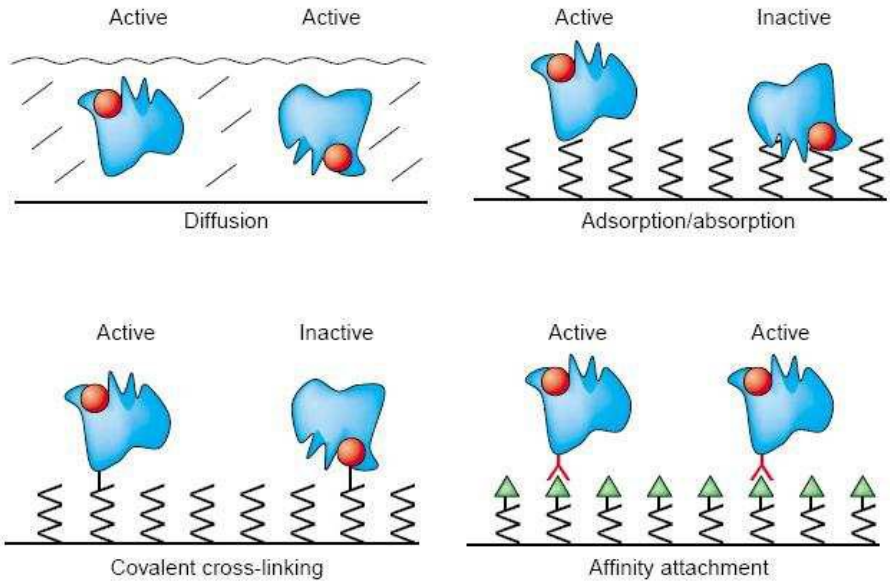

Figure 1.4: Comparison of protein attachment methods. Except from affinity attachment, proteins are usually laid on the surface in a random fashion, which may alter their native conformation, reducing their biological activity, or make them inaccessible to probes[13].

Protein diffusion in 3D gels and agarose thin films is a methodology with high binding capacity without requiring protein modification. However, gel fabrication can be quite tough and expensive. Protein adsorption/absorption is used with surfaces which have a high inherent binding energy to proteins in general. The most common of these substrates are hydrophobic plastics such as

polystyrene, to which most proteins physically adsorb by van der Waals, hydrophobic and hydrogen-bonding interactions. This type of physical adsorption is used to immobilize "capture antibodies" in enzyme-linked immunosorbent assays (ELISA). This immobilization is very simple to perform, because it does not require any modification of the protein for its attachment to the surface. The disadvantage is that proteins can be inactivated because of surface-induced denaturation and steric occlusion.

Protein covalent linking to surfaces is the most used protein attachment method for protein biochips. The immobilization procedure must be optimized to obtain the maximum surface coverage preventing the biological molecule denaturation and/or the loss of its specific properties, e.g., for an enzyme its enzymatic activity. The surface-linked protein must be oriented on the surface such that the active site or binding site faces away from the protein thin film and can therefore interact optimally with proteins in the biological sample. This is most easily achieved when using recombinant proteins, in which amino-, carboxy- or His-tag terminal tags are introduced to realize highly specific affinity interactions. Proteins fused with a high-affinity tag at their amino or carboxy terminus are linked to the surface via this tag, and hence, all of the attached proteins should orient uniformly away from the surface. For non recombinant proteins, one must take advantage of existing functional groups on the protein, as for example the amino or hydroxyl groups. For silicon dioxide surfaces, for example, a bifunctional silane crosslinker is used to form a self-assembled monolayer (SAM) which possesses one functional group that reacts with hydroxyl surface groups, and another free one that can either react with primary amine groups of proteins or can be used to react with a liker molecule which is reactive towards primary amine groups of protein.

1.1.3 Detection methods

Fluorescent dyes are the most prevalent methods for detecting binding of proteins on microarrays, although chemiluminescence and colorimetric methods are alternative ways whose use is increasing. Fluorescence detection methods are generally the preferred methodology in research lab, because they are simple, safe, extremely sensitive and can have very high resolution[12]. The most used fluorescent dyes include Cy3 and Cy5, the same dyes that have found application in DNA arrays. However, the expensive instrumentations required for fluorescence methods, such as laser confocal microarray scanner have limited the wide applications of DNA and protein microarray technologies, especially in clinical diagnosis. Chemiluminescence has been used for detecting antigen binding on microarrays using biotinylated secondary antibodies in conjunction with Streptavidin-conjugated peroxidase. Colorimetric-based detection methods are attractive because the experimental setups are relatively low-cost and simple. Colorimetric detections can be carried out with inexpensive imaging equipment such as a CCD camera and a computer software

for data analysis. While these aspects are beneficial because they drastically reduce the cost and procedural complexity of the experimental setup, colorimetric methods sometimes suffer from lower detection limits, respect to fluorescence methods. Liang et al. have used a colorimetric nanogold probe coupled with silver enhancement (gold–silver detection) to produce black image of microarray spots, which can be easily detected with a commercial CCD camera. In order to study the kinetics of biomolecular interactions, however, real-time detection methods will be useful.
Capture agents binding of protein analytes in a sample is detected by scanning the array, using either a scanning confocal laser or a charged coupled device (CCD) camera-based reader. Once the array image has been captured, computer software is used to obtain background corrected intensity values of each of the spots after gridding the elements of the array. Background signal can be measured in a local (area around individual spots) or global (area outside of the grid) way. Next, a set of corrections (normalization) are usually defined to account for factors such as variation in sample quality, sample labeling, and other sources of systematic and biological variation which may be reflected in the raw data produced. The method used for normalization is a critical choice, one which can impact efforts to compare accuracy and precision between different arrays.

1.2 Patterning Methodologies

The success of microarray technology in genomic and proteomic research has given new impetus to miniaturization methods that facilitate evaluation of a large number of chemical structures against hundreds of biological targets. Key parameters include the number of different probe sites (spots) per unit area and the number of probe molecules per unit area within an individual probe site (the molecular density per each spot). The probe sites and their spacing should be as small as possible in order to get high-density array, while allowing efficient molecular recognition.
According to spot formation techniques, methods are classified as “contact printing” and “non contact printing”[14]. Contact printing is a widely used technology, comprising methods such as contact pin printing and microstamping. These methods are reproducible and require little maintenance, but have low-throughput array fabrication. Non-contact printing techniques are newer methodologies, and comprise photochemistry based methods, laser writing, electrospray deposition, and inkjet technologies. Microarray fabrication is a biological fluid dispensing process. Drops of biological solutions are deposited in an addressable arrangement of spots on a substrate surface. The spots must be homogeneous and dense, yet spatially discrete. Any patterning technique should minimize cost and the required volume of solution, while preventing solution contamination and biomolecular damage.

1.2.1 Contact printing

Contact printing techniques are quite diffused in microarray technology. Tipical micropatterning methods are contact Pin Printing and Microstamping. There exist still poor developed nanoscale contact patterning methodologies such as Dip Pen Nanolithography and Nanoscale Dispensing by hollow tips.

Pin Printing

Pin printing is the most used biopatterning technique and it was also the first one to be introduced[15]. The uniformity in spot formation depends on sample viscosity, pin surface properties and substrate properties. Spot dimensions depend on the print velocity, on the solution surface tension and on the solution wettability on the substrate surface. Pin is realized using metals or silicon.

There exist two pin printing typologies: solid pin printing and split pin printing (**Fig. 1.5** and **1.6**).

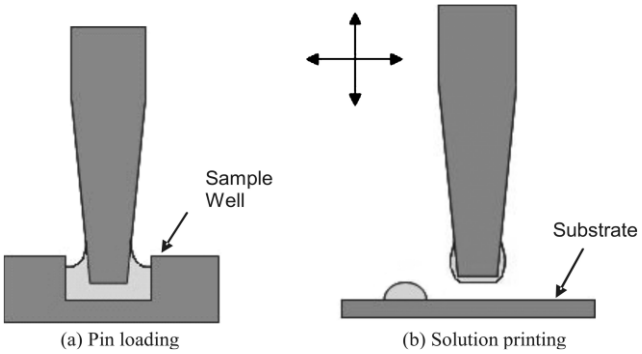

Figure 1.5: Solid pin printing process. (a) Pin is immersed in the sample solution to load the sample to the pin (b) The pin contacts substrate surface to dispense the sample.[14]

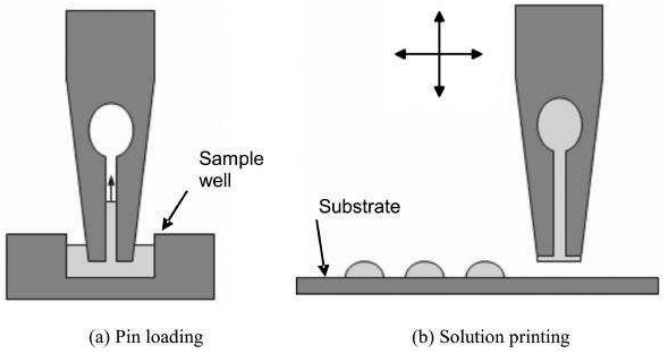

Figure 1.6: Split pin printing process. (a) Split pin (ink stamp) is loaded with solution from well plate by capillary force action. (b) Multiple spot printing with a single load.[14]

In solid pin printing, pin is immersed in the sample solution to load the sample to the pin. The pin contacts substrate surface to dispense the sample. The procedure is quite easy but several time-consuming sample reloads are needed in order to realize a single microarray.

In split pin printing, pins are loaded with solution from well plate by capillary force action into the pins microchannels (their diameter ranges between 10-100 mm). As surface tension forces dominate over inertial forces at the microscale, the gravity effect is negligible. When the pin touches a substrate surface, picoliter-nanoliter volumes of fluid are transferred onto the surface. To overcome surface tension and drive the fluid onto the tip during deposition, the pin is accelerated and then decelerated as it strikes the surface. Because of the pin-substrate contact, the pin tends to degradate after several prints. When a pin is used to print multiple solutions, it must be washed and cleaned to avoid cross contamination. The load-print-wash process is repeated until the desired number of biological spots is printed on the substrate surface. Notwithstanding pin printing being the most known array fabrication methodology, it is a tedious and time-consuming process.

Microstamping

An alternative to pin printing is microstamping (**Fig. 1.7**). With microstamps, hundreds of spots are printed in parallel, enabling high-throughput microarray fabrication[16]. The microstamping process is simple and cheap: a sample is first adsorbed on the patterned surface of a stamp and then transferred to a substrate by physical contact. In order to obtain good contact, microstamps are generally made from elastomeric materials, such as poly (dimethylsiloxane) (PDMS), which conform to surface roughness under an applied load. Mold masters are fabricated by photolithography to define a pattern of the stamp. Then, an uncured liquid elastomer (e.g., PDMS) is cast on the master. After curing, the stamp is released from the master. One limitation of elastomeric microstamp fabrication procedure is the necessity of using photolithography and clean room facilities to form the stamp molds. A problem of microstamping is that the amount of sample transferred from the stamp to the substrate is not well controlled and depends on both surface and sample properties. Additionally, for the same amount of printed sample, microstamping requires larger initial sample volumes, as only a small amount of solution in a well is adsorbed onto the stamp surface, and only a small fraction of the adsorbed solution is transferred from the stamp to the substrate, due to strong non-specific adsorption to the hydrophobic stamp material. Likewise, if microstamps are to be reused, the washing process is more tedious than for pins because of non-specific adsorption.

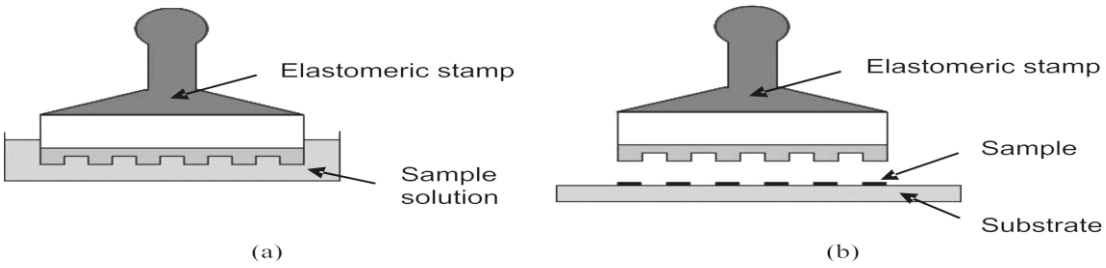

Figure 1.7: Microstamping process[14].

Dip Pen Nanolithography

An extension of the pen concept to micro- and nanoscale cantilevers is direct write Dip Pen Nanolithography (DPN). In the DPN process, molecular inks coated on an AFM tip are transferred to a substrate, while the tip is moved along a surface[17]. Features size less than 15 nm can be realized by molecular self-assembly of the ink on the substrate. Espinosa and coworkers have demonstrated a novel microfluidic AFM probe called the nanofountain probe (NFP) which has sub-100 nm patterning capability. It consists of a hollow tip, integrated microchannels and on-chip reservoir. When an ink is fed into the reservoir, it is driven by capillary action through the microchannel of the tip to form a liquid-air interface around the tip core. Molecules are transferred by diffusion from the interface to a substrate and a water meniscus is formed by capillary condensation.

Dip pen nanolithography is discussed in details in the next chapter.

Nanoscale dispensing system (NADIS)

Biological dispensing at the nanoscale can be achieved by modifying a commercially available AFM probe. By using focused ion beam (FIB) milling, it has been possible to open a nanoscale aperture at the tip apex to make a loading area for the liquid. Upon contact with the surface, incredibly small volume (few tens of zeptoliters) of the liquid at the end of the cantilever is directly transferred to the surface in an event typically requiring less than 1 ms. Capillary fluid flow instantly replenishes the volume at the gap, and the device is ready to write the next feature[18]. Compared to DPN, NADIS provides a more versatile technique since (i) a single cantilever can carry a volume equivalent to typically millions of spots, (ii) it can deposit any soluble molecule, and (iii) the liquid transfer is entirely controlled by aperture size and surface energies.

1.2.2 Non contact printing

Contact printing methods include several techniques, but all involving contact between the substrate surface and a stamp or pin. In contrast, in non contact printing, there is no physical contact between the printing device and the surface. These methods vary considerably from photochemistry-based methods to laser writing to fluid droplet dispensing. There are two main advantages to non-contact printing: reduced contamination and higher throughput.

Since the printing device and the substrate never experience physical contact, the possibility of contamination is greatly reduced and the need to constantly clean the printing device between uses is eliminated. Furthermore, non-contact printing methods hold the greatest potential for increasing microarray fabrication throughput, because many non-contact methods deposit solutions in parallel, allowing entire arrays to be produced simultaneously.

Among non contact printing techniques, the most useful ones are: photochemistry-based printing,

electro-printing, laser writing and droplet dispensing. The first methodology is commonly employed in high-throughput DNA microarrays fabrication. The main drawback is the risk of biomolecular denaturation due to the involved photochemical stresses.

The second and the third methods are not so commonly employed. Instead, droplet dispensing seems to be the best way to realize biomolecular arrays. It can be classified into three types: motion controlled pin printing, electrospray deposition (ESD), and inkjet printing. Among these, the most promising one is inkjet printing because it offers the advantage of straightforward, high-speed, high throughput fabrication process without the use of masks, stamps or other costly and time-consuming conventional processing equipment. This technique deals with the generation of a pressure pulse within a confined liquid leading to the ejection of a drop from a micrometric orifice. The drop will finally hit the surface of a convenient substrate. This non contact patterning methodology will be discussed in details in the next chapter.

Bibliography

1. Clementi, F. & Fumagalli, G. *General and Molecular Pharmacology: Principles of Drug Action*. (2015).
2. Terstappen, G. C. & Reggiani, A. In silico research in drug discovery. *Trends Pharmacol. Sci.* **22,** 23–26 (2001).
3. Wölcke, J. & Ullmann, D. Miniaturized HTS technologies – uHTS. *Drug Discov. Today* **6,** 637–646 (2001).
4. Laurell, T., Nilsson, J. & Marko-Varga, G. The Quest for High-Speed and Low-Volume Bioanalysis. *Anal. Chem.* **77,** 264 A-272 A (2005).
5. Lemmo, A. V, Rose, D. J. & Tisone, T. C. Inkjet dispensing technology: applications in drug discovery. *Curr. Opin. Biotechnol.* **9,** 615–617 (1998).
6. Hong, J., Edel, J. B. & deMello, A. J. Micro- and nanofluidic systems for high-throughput biological screening. *Drug Discov. Today* **14,** 134–146 (2009).
7. Huels, C., Muellner, S., Meyer, H. E. & Cahill, D. J. The impact of protein biochips and microarrays on the drug development process. *Drug Discov. Today* **7,** S119-24 (2002).
8. Ma, H. & Horiuchi, K. Y. Chemical microarray: a new tool for drug screening and discovery. *Drug Discov. Today* **11,** 661–668 (2006).
9. Gosalia, D. N. & Diamond, S. L. Printing chemical libraries on microarrays for fluid phase nanoliter reactions. *Proc. Natl. Acad. Sci.* **100,** 8721–8726 (2003).
10. Ma, H., Horiuchi, K. Y., Wang, Y., Kucharewicz, S. A. & Diamond, S. L. Nanoliter Homogenous Ultra-High Throughput Screening Microarray for Lead Discoveries and IC50 Profiling. *Assay Drug Dev. Technol.* **3,** 177–187 (2005).
11. Zhu, H. & Snyder, M. Protein arrays and microarrays. *Curr. Opin. Chem. Biol.* **5,** 40–45 (2001).
12. Hall, D. A., Ptacek, J. & Snyder, M. Protein microarray technology. *Mech. Ageing Dev.* **128,** 161–167 (2007).
13. Zhu, H. & Snyder, M. Protein chip technology. *Curr. Opin. Chem. Biol.* **7,** 55–63 (2003).
14. Barbulovic-Nad, I. *et al.* Bio-Microarray Fabrication Techniques—A Review. *Crit. Rev. Biotechnol.* **26,** 237–259 (2006).
15. Wang, X. H., Istepanian, R. s. H. & Hua Song, Y. *Microarray image enhancement by denoising using Stationary Wavelet Transform*. *NanoBioscience, IEEE Transactions on* **2,** (2004).
16. Renault, J. P. *et al.* Fabricating Arrays of Single Protein Molecules on Glass Using Microcontact Printing. *J. Phys. Chem. B* **107,** 703–711 (2003).
17. Piner, R. D., Zhu, J., Xu, F., Hong, S. & Mirkin, C. A. 'Dip-Pen' Nanolithography. *Science (80).* **283,** 661 LP-663 (1999).
18. Fang, A., Dujardin, E. & Ondarçuhu, T. Control of Droplet Size in Liquid Nanodispensing. *Nano Lett.* **6,** 2368–2374 (2006).

II General Part

2 Biopatterning Fabrication Methodologies

This chapter presents the state of the art in the field of bioarray fabrication methods, especially focusing on the solution-based approaches. Specifically, Inkjet printing and Dip Pen Nanolithography (DPN) techniques are described in detail. In particular, as far as the ink-jet printing is concerned, details on the piezoelectric technology for biological array fabrication, mechanisms of droplet formation and impact on hard and soft surfaces are provided. As to the Dip Pen Nanolithography, writing mechanism is analyzed focusing on the difference between diffusive and liquid ink depositions. Evolution in high-throughput patterning by employing 1D and 2D pen arrays are also presented.

2.1 Inkjet Printing

Inkjet printing is a flexible, gentle and robust micropatterning technique featured with rapidity and cost-effectiveness, not requiring the use of masks, stamps or other costly and time-consuming conventional processing equipment[1,2]. Inkjet printing has been implemented in many different designs and has a wide range of potential applications: fundamentally, inkjet printing is divided into the continuous and the drop-on-demand inkjet methods. The latter is the most popular, in which a series of electrical signals is employed to control the actuation at the moment of drop ejection. Depending on the mechanism used in the drop formation process, the technology can be categorized into four major methods: thermal, piezoelectric, electrostatic, and acoustic inkjet. Most, of the drop-on-demand inkjet printers use either the thermal or piezoelectric principle[3]. However, for Life Science applications thermal inkjet mode is not the best choice because of the heat stress that would affect printed bio-materials; then piezoelectric dispensing remains the most used method[4,5].

2.2 Piezoelectric Inkjet Printing

Piezoelectric inkjet printing is a thermally constant process that is carried out at a constant temperature. The piezoelectric print-head consists of a piezoelectric transducer, nozzles, manifolds, ink pumping, chambers, and fluid inlet passages. When a voltage is applied to a piezoelectric transducer, typically lead zirconate titanate (PZT), the transducer deforms and creates mechanical vibrations. The electric signal applied to the piezoelectric is called waveform: a complex pattern of

electrical impulses consisting in a series of square waves. Each square wave is characterized by a voltage value Vi, a time interval ti and a slope pi. The absolute value of the voltage is correlated to the entity of the compression inside the fluid chamber. The slope is correlated to the compression rate, while the time interval is correlated to the time the piezoelectric transducer remains in a defined position. These vibrations create acoustic waves, which in turn force ink out of the chamber through the nozzle. Piezoelectric print heads (**Fig. 2.1**) are categorized based on the deformation mode of the transducer in squeeze mode (a), bend mode (b), push mode (c), or shear mode (d).

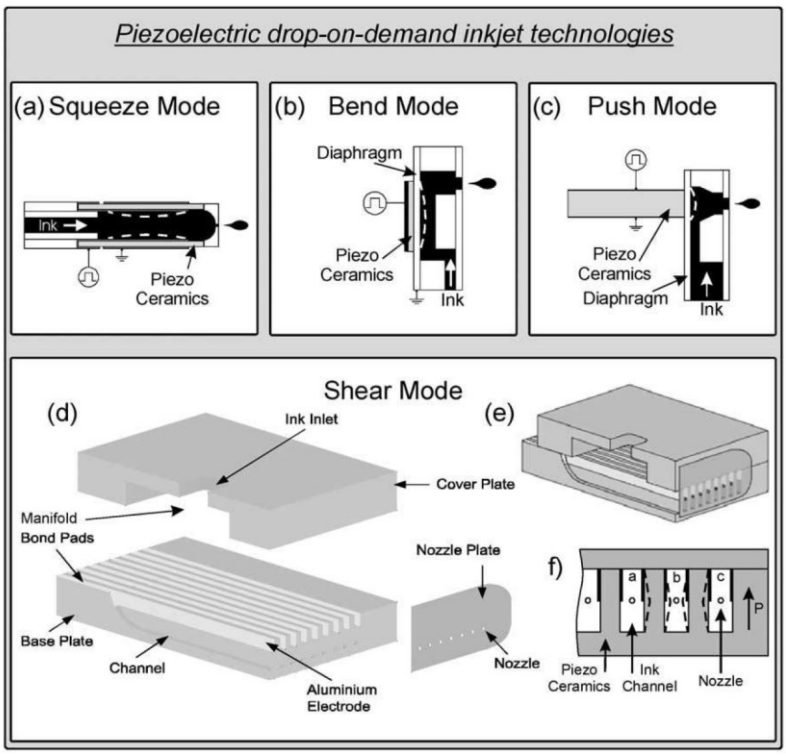

Figure 2.1: Piezoelectric drop-on-demand technologies[3].

The volume of the emitted droplet is in relation to the nozzle size typically lying in the picoliter to nanoliter range. During droplet formation, energy is distributed between viscous flow, the drop surface tension, and the drop kinetic energy. In turn, this leads to a liquid jet resolving into a droplet hitting the substrate surface. Unlike other patterning methods, ink-jet printing has the great advantage to allow precise and controlled parallel deposition of small volumes (typically picoliter to nanoliter range) of multiple biological materials using independent jets (i.e. independent controlled micro-channels) on almost any possible type of substrates solid, gel, liquid surfaces being a contactless in nature. Moreover, the hardware integration with automated translation stages enable precise pattern placement and registration for preparing multilayer patterns with different printed biomaterials. Several papers report on the realization of multiplexed arrays via

piezodispensing nanoliter to picoliter droplets for realizing accurate biomolecular assays involving DNA hybridization on functionalized surfaces[6,7] and characterize interactions involving delicate proteins: in particular MacBeath set up a high throughput microarray-based strategy for measuring the equilibrium dissociation constant of different recombinant PDZ domains for fluorescently labelled peptides[8,9]. M.S. Hasenbank et al.[10] showed multi-protein patterning ink-jet printing for setting-up a biosensor assay.

The method involved a two sequential patterning steps, consisting in the initial deposition onto gold-coated surface of a mixed thiol layer (BAT/PEG thiol solution) to provide oriented binding capabilities in a non-fouling background and a second deposition of multiple biotinylated proteins (b-HRP and b-BSA). Antibodies specific to each of the two proteins were introduced in a development step in the SPR microscope in order to execute detection. Highly specific binding of the antibodies to the immobilized proteins was observed. In addition, Sukumaran et al. showed the advantage given by the combination of enzyme encapsulation techniques in alginate and microarraying methods for an integrated screening platform for CYP450 [11] while Lee et. al prepared a miniaturized 3D cell-culture array for high-throughput toxicity screening of drug candidates and their cytochrome P450-generated metabolites[12].

Together with heterophase assays, piezo inkjet droplet formation enables droplet microarray fabrication: an innovative technique that permits to conduct enzymatic assays in liquid droplets. Accordingly, this approach was firstly developed by Gosalia et al.[13] who arrayed chemical compounds inside nanoliter droplets of glycerol and by aerosol deposition, added reagents and water to assemble different multiple biochemical reactions without requiring chemical linkage of the protein to the surface. They were able to execute kinetic profiling of protease mixtures, protease-substrate interactions and high throughput reactions showing the suitability of the method by the identification of an inhibitor of caspases 2, 4 and 6. Based on this approach, Mugherli et al. set-up a robust microarray platform in which multiple reactions are conducted in piezo deposited nanoliter droplets maintained on a glass slide for the in situ preparation of derivatives of thousands of derivatives of phenylboronic acid and their successive activity screening on the NS3/4A protease of the hepatitis C virus[14] and, in a subsequent paper they were able to identificate new type of fluorescent pharmacophores by multicomponent reactions using combinatorial synthesis and screening of chemical libraries in droplet microarrays[15].

In particular, the assembly by a multicomponent reaction is a unique potential for synthesizing thousands of structurally different fluorescent molecules. Since they are based upon a druglike scaffold, these fluorophores maintain their molecular recognition potential and, thus their suitability as bioimaging probes. Despite its simplicity, inkjet printing deposition has some drawbacks. Nozzles tendency to produce undesirable satellite droplets that contaminate surrounding spots and thus, reduce printing resolution. In addition, it is difficult to completely flush

printing nozzles before a new solution is loaded. This problem is more serious in piezoelectric printers since the nozzle is separated from the ink reservoir and all linking channels must be flushed clean. In addition, droplets experience high shear rates while passing through the nozzle and impacting the substrate surface: under these shear rates, there is a risk of denaturing biomolecules in the solution[16]. Accordingly, for achieving high resolution and good morphology spots and avoid the formation of undesirable satellites together with the primary droplet, its rheological properties have to be optimized being those of typical biological solutions (that have low viscosities and high surface tensions), with the addition of viscous, surfactant and bio-compatible additives in the buffer solution. In this sense, it has been shown that additives like glycerol can increase fluid viscosity at a sufficient level in order to permit satellites free droplet formation and retaining of the biological activity[17].

The main stages of drop-on-demand drop formation are ejection and stretching of liquid, pinch-off of liquid thread from the nozzle exit, contraction of liquid thread, breakup of liquid thread into primary drops and satellites, and recombination of primary drop and satellites. The final phase of the process consists in the impact of the ejected droplet towards the substrate.

2.2.1 Droplet formation and ejection

When the piezoelectric transducer expands, liquid in the nozzle is accelerated and pushed out of the nozzle orifice. Initially, the meniscus extends outward until a liquid column with a round leading edge is formed. After a short time, the liquid flow rate from the nozzle decreases. The speed of liquid at the nozzle exit falls until no additional liquid flows into the column. The volume of the liquid column remains constant, and the inertia of the liquid extends the column: during the stretching of the liquid column, the liquid at the tail necks. This necking position remains at the nozzle exit, and the radius of the liquid thread here continuously thins. Finally, the tail of the liquid thread pinches off from the nozzle exit, creating a free liquid thread with a bulbous head. The time required for the ejected fluid to stretch and then pinches off from the nozzle exit is called pinch-off time. Subsequently, recoil of the free liquid thread occurs because pressure is high in the tail tip at pinch-off so that the tail recoils toward the head of the drop. During the shrinkage of the liquid thread, the liquid thread tends to break up into two parts, a primary drop and a free secondary and unsymmetrical liquid threads that may shrink into a smaller drop or satellite, or break up into two or more parts. So the breakup of the free liquid thread leads to the generation of a primary drop and satellite(s)[18]. During the contraction of the liquid thread after it has pinched o from the nozzle, two modes of breakup are possible: end-pinching where the liquid thread pinches off from an almost spherical head, and multiple breakups of the liquid thread due to capillary waves. The evolution of the liquid thread depends on the length of the liquid thread at pinch-off, which increases with voltage. For the shorter water threads, a capillary wave is not observed, and satellite formation

results from end-pinching.

For longer water threads, a wave-like instability typically occurs along the thread. As the amplitude of the capillary wave increases, the liquid thread breaks up at several locations at slightly different times, forming several satellites. The longer the liquid thread, the more satellites are formed. Multiple breakups evolving from the wave-like instabilities complicate the printing performance due to the generation of satellites and are unfavorable for drop-on-demand formation. Multiple breakups

and end-pinching both originate from the growth of disturbances along the liquid thread. Using the results from the linear instability analysis, it is possible to derive the following equation that permits to quantify the pinch off time:

$$t_b = \frac{1}{\alpha^*_{max}} \left(\frac{\rho R^3_{noz}}{\gamma} \right)^{1/2} ln \left(\frac{R_{noz}}{\epsilon_{max}} \right) = C \frac{t_{ca}}{\alpha^*_{max}}$$

where $C = ln(R_{noz} / \varepsilon_{max})$ and $t_{ca} = (\rho R^3_{noz} / \gamma)^{1/2}$ is referred to as the capillary time. α_{max} is the fastest temporal growth rate of the disturbance along the surface of the thread. ε_{max} is the (typically unknown) initial amplitude of the disturbance corresponding to α^*_{max} . This is the expression for α^*_{max}:

$$\alpha^*_{max} = \left\{ \left[\frac{1}{2} x^2_{max} (1 - x^2_{max}) + \frac{9}{4} Oh^2 x^4_{max} \right]^{1/2} - \frac{3}{2} Oh x^2_{max} \right\}$$

where *Oh* is the Ohnesoger number ($Oh = \mu/(\rho\sigma D^{1/2})$, ($\mu$, ρ, σ are respectively dynamic viscosity, density and surface tension of the printed liquid), and $x^2_{max} = 1/(2+\sqrt{18}\ Oh)$. According to these equations, the breakup time of a liquid thread should only depend on the capillary time and α^*_{max}. The *Ci* coefficients can be associated to the breakup times. These coefficients are defined as follows:

$$C_i = \frac{t_{bi} - t_e}{t_{ca} / \alpha^*_{max}}$$

In this expression, the ejection time t_e is subtracted from the breakup time because typically little stretching occurs in the ejected liquid during the ejection stage, as the ratio of the surface area to volume of the ejected liquid is almost constant during the ejection-stage. *C1* (the first breakup) refers to t_{b1}, the time required for the pinch-o of the liquid thread, while *C2* (the second breakup) refers to the end-pinching. After the liquid snaps o from the nozzle exit and becomes a free- flying thread, the thread tail recoils rapidly under the action of the surface tension.

The expression for retraction speed is given by this equation:

$$v_r = \left(\frac{2\gamma}{\rho r_0}\right)^{1/2}$$

where r_0 is the radius of the liquid thread. Being the radius of the liquid thread scaled by the radius of the nozzle, R_{noz}, then

$$v_r \approx a v_{ca}$$

where a is a constant and $v_{ca} = (R_{noz})^{1/2}$, referred to as the capillary speed. The evolution of the free-flying liquid thread depends on the liquid and driving voltage. If the driving voltage is sufficiently low, no satellites are formed. At higher voltages, the breakup of the free-flying liquid thread occurs, and satellites form.

2.2.2 Droplet impact on solid and liquid surfaces

Droplet impact phenomena considerably differ in function of the aggregation state of the receiving surface, being it solid or liquid. The main dimensionless groups governing drop impact here employed for the discussion are the Weber number *We*, the Ohnesorge number *Oh* and the Reynolds number *Re* [19]:

$$We = (\rho D_0 (U_0)^2)/\sigma,$$
$$Oh = \mu/(\rho\sigma D^{1/2})$$
$$Re = \sqrt{We}/Oh$$

where ρ is the density of the fluid, D_0 and U_0, respectively, are the diameter and the velocity of the droplet before impact, μ is the dynamic viscosity and σ is the fluids surface tension. The typical operating regime for ink-jet printing operation is characterized by high Reynolds numbers ($O(10) < Re < O(10^3)$) and intermediate to high Weber number ($O(1) < We < O(10^2)$).

The Weber and Reynolds numbers for the droplet generation process are equal to those of the impact process. In order to obtain sufficient ballistic accuracy of a droplet, the Weber number of droplet generation should be typically We > ~ 1, while the integrity of the droplet determinates an upper limit on the Weber number. In other words, excessively slow jetting drops could lead to an inaccurate trajectory, while a high drop speed may lead to the formation of undesirable tails along with drop satellites. The piezo-acustic generation mechanism must have Re > ~ 1 in order to prevent excessive viscous damping, while the need for some damping of the fluid after droplet generation puts un upper bound on the Reynolds number[20].

The impact of the droplet on a solid substrate can be subdivided in three phases[20]. In the initial impact phase, the droplet hits the substrate with air bubbles entering inside the droplet at the very moment of impact. In second phase, the radial extent of the droplet-substrate interface becomes of the order of magnitude of the initial droplet radius and there is a rapid radial fluid flow in which a

blob of fluid is formed near the contact line. After the fluid has reached its maximum radial extent, oscillations set in after a rebound in which the droplet remains intact as one volume. In the case of high-contact angle surfaces and large Weber numbers, the droplet can move beyond its equilibrium advancing contact angle. When the droplet has low speed (We < 1), the droplet deforms as a whole and flattens somewhat, already during the first stage of impact - this behaviour being explained by considering capillary force as the important driving mechanism for spreading. For these impacts, the time scales for capillary-driven spreading and deformation of the whole droplet are the same. The final radius becomes larger for experiments with a larger Weber number and is a function of the surface contact angle. At high Weber numbers (We > 8), in the first stage of impact the upper part of the droplet remains undisturbed. Then for high speed impacts, the time scale for spreading R0/U0 becomes considerably smaller than the time scale for deformation of the droplet by surface tension. In the third phase, the fluids come to rest in a process of rebound followed by inertial oscillations, damped by viscous dissipation. A high amount of the initial energy in the droplet before spreading is dissipated by viscosity through the oscillations. The value of the final radius can be calculated by considering an energy balance based on surface energy, kinetic energy, and viscous dissipation in the following form:

$$\frac{2}{3}\pi R_0^3 \rho U_0^2 + 4\pi R_0^2 \sigma = \pi R_f^2 (f_s \sigma + \sigma_{ls} - \sigma_{sv}) + \triangle E_u$$

where R_f is the final radius after impact has completed, f_s is the ratio of the fluid-vapor surface and the fluid-solid surface, and ΔE_u is the dissipated energy in the impact process by viscosity, σ_{ls} and σ_{sv} are the surface energies of the liquid-solid and solid-vapour interfaces, respectively.

After impact, the fluid flow velocity is zero and the droplet has taken the shape of a spherical cap with contact angle θ, which can take values between the equilibrium advancing contact angle θ_{adv} and the receding contact angle θ_{rec}. A special case is constituted by the impact of a droplet on a porous substrate: in this case, the liquid in the droplet is imbibed due to capillary suction in an initially dry and undeformed substrate: then deformation of the substrate occurs as the liquid fills the pore space.

The drop impact on a liquid surface is a slightly more complicated case; a good review dealing with the physics underneath is the one of Anderson[21]. Briefly, a fundamental parameter for the impact on a liquid surface is the droplet velocity. At low impact velocities (10^{-2} - 1 m/s) practically no rim is visible, and the droplet is simply deposited on the liquid film. At velocities of the order of 1-30 m/s, the motion initiated by the drop is virtually unconstrained and capable of pushing apart a significant liquid mass under the impact site (conditions of droplet spreading): the drop takes the shape of lamellae with a visible outer rim. At higher impact velocities (conditions of droplet splashing), the lamellae take the shape of crowns consisting of a thin liquid sheet with an unstable free rim at the top, from which numerous small secondary droplets are ejected. The threshold for a

droplet splashing in a train of frequency *f* is given this expression:

$$V_{0S} = 18\left(\frac{\sigma}{\pi}\right)^{\frac{1}{4}} \nu^{\frac{1}{8}} f^{\frac{3}{8}}$$

where π, ν and σ denote liquid density, kinematic viscosity, and surface tension, respectively. Drop spreading occurs at the impact velocities $V_0 < V_{0S}$, whereas at $V_0 > V_{0S}$ splashing and formation of a crown and multiple secondary droplets occur. Following the impact, mixing between the droplet and the liquid surface occurs: this phenomenology is strictly dependent upon the molecular diffusion in liquids and then, assuming Brownian motion ($x_2 = 2D \bullet \tau$, where x is the distance traveled, D is the coefficient of diffusion, and is τ is the time), it depends upon the dimension - and then the volume - of the considered droplet. For example, a small molecule like fluorescein needs about 36 s to diffuse across 215 µm (that is a 10 nL droplet), but only 3.6 ms for diffusing on a 2.15 µm droplet (10 fL volume)[22].

2.3 Nano tip printing technique: Dip Pen Nanolithography (DPN)

Nano Tip printing techniques are an ensemble of methodologies that permit to achieve submicron resolution, high spot density and more complex arrays, being initially developed from the atomic force microscope (AFM), the master tool for nanoscale investigation of materials surfaces. These methods are able either to perform adding process of molecules to a substrate - i.e. Dip Pen Nanolithography - or removing self-assembled molecules nanoshaving.

Nanoshaving is a destructive method, thus not allowing direct multiple features patterning, but it can be adapted by using careful experimental procedures. Accordingly, Tinazli et al.[23] set-up a proof-of-concept double protein nanopattern experiment: they developed a write, read and erase method in which uniformly oriented His-tagged proteins immobilized on a NTA-functionalized (i.e. oligoethylene alkyl thiols with nickel-N-nitrilotriacetic acid moieties) surfaces are removed with an AFM tip in contact oscillation mode and replaced simultaneously or sequentially with other His-tagged proteins. The above presented methods enable multiplexing, but they are quite laborious and not robust enough for high-throughput biological applications.

Introduced by Mirkin et al. in 1999 [24], Dip Pen Nanolithography is a powerful atomic force microscope based constructive patterning technique that permits to fabricate nano- and micro- scale patterns in ambient conditions along with high registration and recently high-throughput capabilities. Dip pen nanolithography enables the realization of devices as diverse as nano-scale electronic circuits, chemical sensors, micro- nano- arrays of organic and biological molecules for cell biology studies and so forth. The method is based on the ink transportation from an ink-coated AFM tip to a receiving surface. Two possible deposition mechanisms exist diffusive or liquid. In

the diffusive regime, the tip is dipped into the ink solution with subsequent solvent evaporation leading to molecules coated on the DPN tip to be deposited on the surface substrate by the naturally occurring water meniscus at the interface with the receiving surface (**Fig. 2.2**).

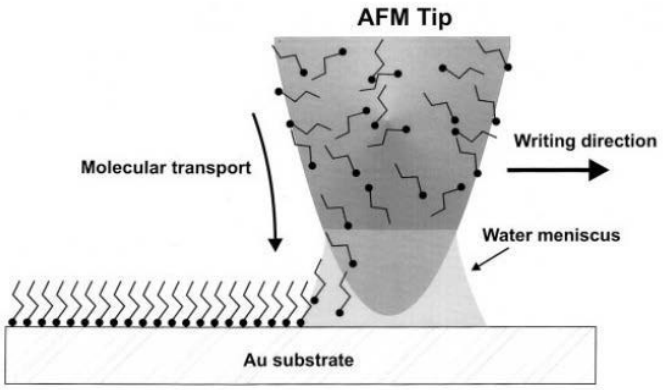

Figure 2.2: Schematic representation of DPN for molecular inks. A water meniscus forms between the AFM tip, coated with the organic molecule ODT, and the Au substrate. The dimension of the meniscus is controlled by relative humidity affecting the molecular transport rate and the lateral resolution[24].

The ink deposition rate is then directly function of the molecular diffusion rate, which is molecule-specific; this feature complicating the implementation of multiplexed-patterning[25] [28]. Moreover, the patterned feature size depends on temperature, relative humidity, tip/surface dwell-time, ranging from micro- till nano- scale (< 100 nm). Specifically, the molecular or liquid aggregation state of the ink gives rise to significant changes in deposition mechanism. In the present section, the physical mechanisms involved in the DPN deposition process are discussed by summarizing the experimental and theoretical results obtained so far.

2.3.1 Molecular inks

Molecular inks are composed of small molecules coated onto a DPN tip and are dispensed to the surface through a water meniscus that forms naturally when the tip is brought in contact to the surface. Molecular dynamic simulations have also indicated the existence of such a nucleating process. Also, a thin aqueous film (of the order of one or two molecular layers) is believed to adhere on all surfaces under ambient conditions, which can also aid in the formation of a capillary bridge.

On the other side, a liquid ink is a material that is always liquid at the deposition conditions. The liquid deposition properties are determined by the surface energies of interactions between the liquid and the tip, the liquid and the surface, and the viscosity of the liquid itself. The crucial point for the transfer of material from a tip to a substrate is the formation of a liquid bridge (or meniscus) between the tip and the sample due to the capillary condensation. This meniscus plays a fundamental role since it forms the transfer path for the ink molecules. Its size increases with

increasing humidity and by decreasing the distance between the tip and the sample. This point has been estimated by computer simulations and confirmed by experiments of environmental scanning electron microscopy as well as by STM. The shape of the meniscus is also influenced by the hydrophilic/hydrophobic character of the substrate. In case of hydrophilic surface, the small contact angle leads to a spreading of the meniscus, so providing a larger volume meniscus which is beneficial for the material transfer. On hydrophobic surfaces, however, the contact area of the meniscus is reduced, so limiting the cross section of the water bridge and then reducing the material transfer. Double ink DPN experiments with MHA (hydrophilic) and ODT (hydrophobic) were performed for verifying this process. Firstly, a dot pattern was produced with one molecular ink. Afterwards, a second pattern was deposited on the top of the first one using the complementary ink. For ODT the deposition rate was increased when patterning on top of the hydrophilic MHA as compared to deposition on the bare gold substrate.

MHA patterning exactly showed the opposite trend, i.e. higher transfer rate on naked gold surface as compared to on top of hydrophobic ODT.

The formation of the meniscus also has pronounced consequences on the tip-sample interactions due to capillary forces that can determine tip abrasion leading to lager radii of curvature. This, in turn changes the contact area and the size of the meniscus leading to changes in the ink transport from the tip to the sample. A full theoretical approach, based on the experimental data has been developed for estimating the amount of the force[26]. Custom made modification of the radius of curvature by laser ablation allowed investigating the influence of the tip size on the deposition. A sub-proportional increase in the deposition rate was observed for increasing size of the tip - for tips showing radii between 40 and 500 nm - leading to larger feature sizes during the patterning process. Assumed the meniscus to be the natural pathway for molecular ink deposition from the tip to the surface, the material transfer itself depends upon several experimental parameters. As was mentioned above, higher humidity leads to a larger meniscus. This feature can be quite advantageous for transferring hydrophilic molecules (as MHA), while for hydrophobic inks (i.e. ODT) there is no increase in the rate of diffusion to the surface. Instead, the transfer rate seems to remain constant or even to decrease slightly with increasing humidity. This observation is attributed to the dissociation of the ink molecules from the cantilever and their subsequent dissolution in the meniscus fluid. For hydrophobic compounds however, this transition is not favourable. Notwithstanding the dependence of the meniscus on the humidity, even under 0 % relative humidity (i.e. nitrogen-purged atmosphere) a residual water layer is present on the surface[27] which is enough for the formation of a meniscus, and deposition had in fact been carried out successfully under these conditions. Since the material transport is based on desorption, solubilisation and diffusion, a strong dependence on the temperature can be expected. Simulations investigating the deposition of ODT during short contact times were performed: it was found that

most of the transferred material comes from the ruptured meniscus. An increase in temperature from 300 to 500 K led to an increase in the deposited amount by a factor of three. The transfer rate also varies over the course of the experiment[28] even if all environmental parameters are kept constant.

The presence of ink already on the surface can slow the transport rate for additional ink. A further consequence of this observation is that the exact nature of the substrate used for a particular DPN experiment can affect the behaviour of the ink during patterning. Although DPN enables the fabrication of nanopatterns of diverse chemical nature on a wide selection of substrates, the transfer of material from the tip to the surface is successful if the choice of ink fits the substrate properties. The main requirement in this respect is the similarity in the hydrophilicity/hydrophobicity of the involved materials. In order to improve this compatibility, use of a surfactant can be required for the effective transport of molecules to the surface.

Studies on the transport of maleimide-linked biotin to mercaptosilane modified glass substrates investigated the effect on deposition abilities of small amounts of Tween-20 (a non-ionic surfactant) in the ink solution. The surfactant was found to decrease the contact angle with increasing concentration, leading to a larger spreading of the meniscus and, hence, promoting the transfer of the hydrophilic biotin derivative on the surface[29]. Once the ink molecule has been transferred to the surface, surface diffusion will determine the material spreading and then the final shape of the pattern. The diffusion can occur in two different ways, termed as serial pushing and hopping down process. In the case of serial pushing mode, a newly transferred molecule will displace a molecule that has been previously deposited, pushing it outward. This displacement continues for other molecules till the pattern boundary is reached. In the case of hopping down, the molecules that are transferred to the substrate are immediately bound strongly to the surface. New molecules thus diffuse on the top of the first monolayer and then hop down to the substrate once they reach the board of the patterned area, again becoming bound to the substrate. Commonly, a mixture of these two processes will occur, the extent of the contribution of each of these mechanism being determined by the molecule-substrate binding energy and the number of binding sites: according to simulation, low binding energies will lead to fractally shaped structures, intermediate energies will lead to patterns related to the substrate anisotropy whereas high binding energies lead to circular shapes. The process of ink dispensing on surface depends on the specific diffusion rate of the molecule, this complicating the deposition of different molecules[25], and hence, preventing implementation of robust multiplex patterning processes.

2.3.2 Liquid inks

A liquid ink is a material that is defined as always liquid at the deposition conditions. Molecules are always dissolved in a liquid during the deposition conditions - this being advantageous especially for patterning biomolecules as they would always remain in their natural hydrated state. The deposition mechanism is function of the surface tension occurring between the liquid and the tip, the liquid and the surface and the viscosity of the liquid[24]; these interactions finally determining a lateral resolution in the micron range scale and not nanoscale. Viscosity is the crucial parameter for the ink writing: higher viscosity leads to lower flow rate from the tip to the surface permitting to pattern for a long time without need of re-inking the tips. Raising ink viscosity also permits to decrease the written features dimensions (till about one micron) and, importantly, to increase the number of spots, so allowing to pattern on large areas (mm^2). Relative humidity affects the meniscus size formed between tip and surface. Importantly, unlike molecular inks, multiplexed depositions can be easily realized since the deposition rates are mainly governed by the liquid properties and not by specific molecular diffusion: this significantly simplifying multiple features patterning on the microscale resolution. In this way, the ink diffusion is molecule independent; different molecules can be printed con temporarily producing same features sizes. Considering that expensive, high-resolution technologies would be required to acquire data from nano-scale arrays, since conventional fluorescence detectors have a resolution down to 1 μm, this method is already able to fulfil the needs of accessible and easy-implementable multiplexed biological assays in array format[30]. The liquid must not have an affinity to the surface that is neither too weak nor too strong. If surface affinity is too weak, the deposition will not occur and if it is too strong, the liquid will transfer from tip to surface as the tip immediately contacts the surface, resulting in uncontrollable ink spreading. These interactions limit the minimum feature size of the liquid ink to about 1 μm, depending on the contact angle of the liquid to the surface. The meniscus between the tip and the surface is essentially composed of the actual liquid to deposit, and not by the water meniscus found in the molecular diffusion mechanism of the diffusive ink-DPN.

Despite several basic studies concerning molecular ink are reported in literature, like for instance[27,31], as far as we know, there are no good comprehensive basic investigations regarding liquid ink transfer mechanism. Thus far, successful control in liquid ink printing has been possible through using additives such as glycerol, agarose and even hexane for PDMS polymer printing to influence viscosity, wettability and the ink-surface interactions[32–34]. With the benefit of a solid knowledge platform about liquid DPN printing mechanism, we can anticipate the liquid-ink deposition to be the prime method of choice for enabling multi patterning biological molecules in friendly conditions and at low cost in order to realize robust complex array devices. In the following sections, a survey of the current state of the art DPN-based fabrication methods for biological applications is presented.

2.3.3 Serial multiplexed printing via single tips

Proof-of-concept multiple biomolecular printing by DPN in diffusive conditions has already been shown in literature for single tips in a serial printing approach, notably a tedious procedure suffering from intrinsic slowness and extremely low-throughput. Demers et al. used a DNA diffusive ink (containing 90% dimethyformamide/10% water solution) coated on a 3-amino propyl trimethoxysilane functionalized tip to produce covalently anchored arrays via DPN of modified oligonucleotide sequences on metallic and insulating substrates[35], showing the possibility to execute double-feature DNA array. **Figure 2.3a** shows the epifluorescence image of two different fluorophore-labeled sequences (Oregon Green 488-X and Texas Red-X) hybridized to the respective complementary sequences deposited on SiOx.

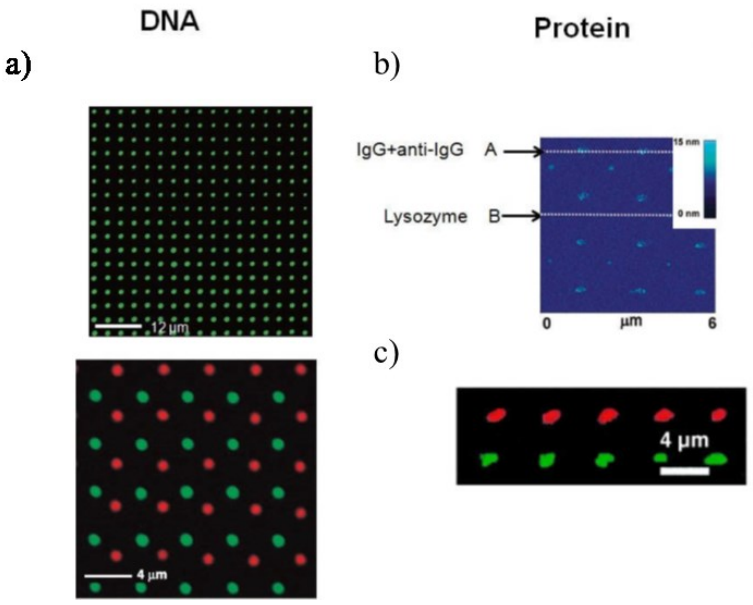

Figure 2.3: a) serial patterning of two different DNA sequences hybridized to their complementary fluorolabeled DNA sequences (Oregon Green 488-X and Texas Red-X) by single pen DPN on SiOx[35]. b) dual protein array made up of IgG and then lysozyme features by serial deposition[36]. c) serial deposition of Antirabbit IgG (Alexa Fluor 594 -red) and antihuman IgG (Alexa Fluor 488 - green) on silicon surfaces[37].

As concerns protein printing, Lee et al.[36] generated dual protein nanoarrays on gold surfaces by serially generating rabbit IgG nanoarrays and then lysozime features in between the IgG spots (**Fig. 2.3b**). Importantly, they functionalized tip surface with a monolayer of PEG which prevents adsorption of proteins on the reflective Au surface of the cantilever by soaking the gold-coated cantilever in symmetric 11-mercapto-undecylpenta(ethylene glycol)disulphide (PEG). To prove the biorecongnition properties of the IgG in the spots, the array was incubated with a solution containing anti-rabbit IgG: a height increase due to the anti-rabbit IgG binding was observed only on the rabbit IgG features and not on the lysozyme patterned areas. Lim et al.[37] employed a modified AFM tip covered with 2-[methoxypoly(ethyleneoxy) propyl] trimethoxysilane (Si-PEG),

that forms a biocompatible and hydrophilic layer, that was dipped in a buffer solution containing the protein of interest with glycerol at 5% - this one to increase the hygroscopicity of the solution. They showed multiple protein-ink capabilities by serially patterning two different fluorophore-labeled proteins, antirabbit IgG (Alexa Fluor 594) and antihuman IgG (Alexa Fluor 488) on an aldehyde-derivatized surface (**Fig. 2.3c**). Recently, C. Xang et al. combined bias-assisted DPN with aptamer-protein recognition (Aptamers are nucleic acids which are able to bind specifically to their targets, which range from small organic molecules to proteins) to fabricate dual protein-protein patterns[38]. Two different types of aptamber arrays to anchor PDGF-BB and thrombin were successfully fabricated by two-step bias lithography and two-step assembling of thiol-functionalized aptamers. Thanks to biorecognition between the two proteins (PDGF-BB and thrombin) and the respective specific aptamers, a multicomponent protein pattern with two different proteins was realized.

2.3.4 Hollow tip nanodispensing in multiplexing

Dip Pen Nanopatterning suffers from the limit of periodic ink refilling, both in liquid and diffusive cases. In this sense, Hollow tip Nanodispensing, also called Nanofountain Probes (NFB) constitute a natural evolution of DPN coat and write technique towards a continuous ink delivery mode in contact mode. Liquid molecular inks stored in an on-chip reservoir are constantly fed through integrated microchannels to apertured dispensing tips by capillary action, this allowing continuous delivery either to a substrate. Like in liquid DPN, solutions are deposited in liquid state, with an attainable lateral resolution consistently from the micrometer till the sub 100 nm scale. The deposition mechanism can be interpreted as liquid diffusion
to the surface as in DPN, also if application of electric fields between the pen and the surface have been show to permit a more consistent fluid dispensing via electrophoretic (EPF) or electro-osmotic ow (EOF) as described by Loh et al.[39]. Consistent control of the spot size at the nanoscale can be achieved by employing hollow AFM probes milled by focused ion beam lithography[40] as Kaisei et al. recently showed in depositing liquid droplets with a volume in zeptoliters scale by applying an electric field between the liquid and a conductive surface[41]. As already shown with DPN, also nanofountain probes enable scalability to 1- and 2-D probe arrays for enhancing the throughput. Moldovan et al. fabricated 1D nanofountain pens array with twelve cantilever probes with microfluidic channels connecting two on-chip reservoirs (that can be filled with two different inks) to volcano-shaped nanofountain pens[42]; in a recent evolution of this system, authors showed the possibility, in principle, to dispense till four different biological inks - each of them inking six pens[39]. As a perspective, NFP could be expanded to 2D arrays by optimization of suitable a network of reservoirs and microchannels with the advantage that NFP cantilevers having protruding tips that eliminate the need for tilting cantilevers against the substrate surface minimize

the problems associated with 2D DPN probe alignment[43].

Since microfluidics elements of NFP are enclosed, multiple inks can be used in adjacent channels without cross contamination and negligible evaporation rates; however big issues derive from easy pen clogging and difficult channel cleaning procedures. This methodology is still prone to advancements and optimization; in fact, solving these hurdles, it could become a broad-applicable liquid nanodeposition tool with applications in direct in vitro single cell injection[44].

Bibliography

1. Sumerel, J. *et al.* Piezoelectric ink jet processing of materials for medicaland biological applications. *Biotechnol. J.* **1,** 976–987 (2006).
2. Boland, T., Xu, T., Damon, B. & Cui, X. Application of inkjet printing to tissue engineering. *Biotechnol. J.* **1,** 910–917 (2006).
3. Brünahl, J. & Grishin, A. M. Piezoelectric shear mode drop-on-demand inkjet actuator. *Sensors Actuators A Phys.* **101,** 371–382 (2002).
4. Lemmo, A. V, Rose, D. J. & Tisone, T. C. Inkjet dispensing technology: applications in drug discovery. *Curr. Opin. Biotechnol.* **9,** 615–617 (1998).
5. Arrabito, G. & Pignataro, B. Inkjet printing methodologies for drug screening. *Anal. Chem.* **82,** 3104–3107 (2010).
6. Beier, M. & Hoheisel, J. D. Versatile derivatisation of solid support media for covalent bonding on DNA-microchips. *Nucleic Acids Res.* **27,** 1970–1977 (1999).
7. Fixe, F., Dufva, M., Telleman, P. & B V Christensen, C. *Functionalization of Poly(Methyl Methacrylate) (PMMA) as a Substrate for DNA Microarrays*. *Nucleic acids research* **32,** (2004).
8. Stiffler, M. A., Grantcharova, V. P., Sevecka, M. & MacBeath, G. Uncovering Quantitative Protein Interaction Networks for Mouse PDZ Domains Using Protein Microarrays. *J. Am. Chem. Soc.* **128,** 5913–5922 (2006).
9. Gordus, A. & MacBeath, G. Circumventing the Problems Caused by Protein Diversity in Microarrays: Implications for Protein Interaction Networks. *J. Am. Chem. Soc.* **128,** 13668–13669 (2006).
10. Hasenbank, M. S. *et al.* Demonstration of multi-analyte patterning using piezoelectric inkjet printing of multiple layers. *Anal. Chim. Acta* **611,** 80–88 (2008).
11. Sukumaran, S. M., Potsaid, B., Lee, M., Clark, D. S. & Dordick, J. S. Development of a Fluorescence-Based, Ultra High-Throughput Screening Platform for Nanoliter-Scale Cytochrome P450 Microarrays. *J. Biomol. Screen.* **14,** 668–678 (2009).
12. Lee, M.-Y. *et al.* Three-dimensional cellular microarray for high-throughput toxicology assays. *Proc. Natl. Acad. Sci.* **105,** 59–63 (2008).
13. Gosalia, D. N. & Diamond, S. L. Printing chemical libraries on microarrays for fluid phase nanoliter reactions. *Proc. Natl. Acad. Sci.* **100,** 8721–8726 (2003).
14. Mugherli, L. *et al.* In Situ Assembly and Screening of Enzyme Inhibitors with Surface-Tension Microarrays. *Angew. Chemie Int. Ed.* **48,** 7639–7644 (2009).
15. Burchak, O. N., Mugherli, L., Ostuni, M., Lacapère, J. J. & Balakirev, M. Y. Combinatorial Discovery of Fluorescent Pharmacophores by Multicomponent Reactions in Droplet Arrays. *J. Am. Chem. Soc.* **133,** 10058–10061 (2011).
16. Nishioka, G. M., Markey, A. A. & Holloway, C. K. Protein Damage in Drop-on-Demand Printers. *J. Am. Chem. Soc.* **126,** 16320–16321 (2004).
17. Barbulovic-Nad, I. *et al.* Bio-Microarray Fabrication Techniques—A Review. *Crit. Rev. Biotechnol.* **26,** 237–259 (2006).
18. Dong, H., Carr, W. W. & Morris, J. F. An experimental study of drop-on-demand drop

formation. *Phys. Fluids* **18,** 72102 (2006).

19. Schiaffino, S. & Sonin, A. A. Molten droplet deposition and solidification at low Weber numbers. *Phys. Fluids* **9,** 3172–3187 (1997).

20. van Dam, D. B. & Le Clerc, C. Experimental study of the impact of an ink-jet printed droplet on a solid substrate. *Phys. Fluids* **16,** 3403–3414 (2004).

21. Anderson, D. M. Imbibition of a liquid droplet on a deformable porous substrate. *Phys. Fluids* **17,** 87104 (2005).

22. Chiu, D. T., Lorenz, R. M. & Jeffries, G. D. M. Droplets for Ultrasmall-Volume Analysis. *Anal. Chem.* **81,** 5111–5118 (2009).

23. Tinazli, A., Piehler, J., Beuttler, M., Guckenberger, R. & Tampé, R. Native protein nanolithography that can write, read and erase. *Nat. Nanotechnol.* **2,** 220 (2007).

24. Piner, R. D., Zhu, J., Xu, F., Hong, S. & Mirkin, C. A. 'Dip-Pen' Nanolithography. *Science (80-.).* **283,** 661 LP-663 (1999).

25. Hampton, J. R., Dameron, A. A. & Weiss, P. S. Double-Ink Dip-Pen Nanolithography Studies Elucidate Molecular Transport. *J. Am. Chem. Soc.* **128,** 1648–1653 (2006).

26. Fabié, L., Durou, H. & Ondarçuhu, T. Capillary Forces during Liquid Nanodispensing. *Langmuir* **26,** 1870–1878 (2010).

27. Weeks, B. L. & DeYoreo, J. J. Dynamic Meniscus Growth at a Scanning Probe Tip in Contact with a Gold Substrate. *J. Phys. Chem. B* **110,** 10231–10233 (2006).

28. Hampton, J. R., Dameron, A. A. & Weiss, P. S. Transport Rates Vary with Deposition Time in Dip-Pen Nanolithography. *J. Phys. Chem. B* **109,** 23118–23120 (2005).

29. Jung, H., Dalal, C. K., Kuntz, S., Shah, R. & Collier, C. P. Surfactant Activated Dip-Pen Nanolithography. *Nano Lett.* **4,** 2171–2177 (2004).

30. Irvine, E. J., Hernandez-Santana, A., Faulds, K. & Graham, D. Fabricating protein immunoassay arrays on nitrocellulose using Dip-pen lithography techniques. *Analyst* **136,** 2925–2930 (2011).

31. Rozhok, S., Piner, R. & Mirkin, C. A. Dip-Pen Nanolithography: What Controls Ink Transport? *J. Phys. Chem. B* **107,** 751–757 (2003).

32. Hernandez-Santana, A., Irvine, E., Faulds, K. & Graham, D. Rapid prototyping of poly(dimethoxysiloxane) dot arrays by dip-pen nanolithography. *Chem. Sci.* **2,** 211–215 (2011).

33. Senesi, A. J., Rozkiewicz, D. I., Reinhoudt, D. N. & Mirkin, C. A. Agarose-Assisted Dip-Pen Nanolithography of Oligonucleotides and Proteins. *ACS Nano* **3,** 2394–2402 (2009).

34. Li, H. *et al.* Nanoscale-Controlled Enzymatic Degradation of Poly(L-lactic acid) Films Using Dip-Pen Nanolithography. *Small* **7,** 226–229 (2011).

35. Demers, L. M. *et al.* Direct Patterning of Modified Oligonucleotides on Metals and Insulators by Dip-Pen Nanolithography. *Science (80-.).* **296,** 1836 LP-1838 (2002).

36. Lee, K.-B., Lim, J.-H. & Mirkin, C. A. Protein Nanostructures Formed via Direct-Write Dip-Pen Nanolithography. *J. Am. Chem. Soc.* **125,** 5588–5589 (2003).

37. Lim, J.-H. *et al.* Direct-Write Dip-Pen Nanolithography of Proteins on Modified Silicon Oxide Surfaces. *Angew. Chemie Int. Ed.* **42,** 2309–2312 (2003).

38. Xing, C., Zheng, Z., Zhang, B. & Tang, J. Nanoscale Patterning of Multicomponent

Proteins by Bias-Assisted Atomic Force Microscopy Nanolithography. *ChemPhysChem* **12,** 1262–1265 (2011).

39. Loh, O. Y. *et al.* Electric field-induced direct delivery of proteins by a nanofountain probe. *Proc. Natl. Acad. Sci. U. S. A.* **105,** 16438–16443 (2008).

40. Fang, A., Dujardin, E. & Ondarçuhu, T. Control of Droplet Size in Liquid Nanodispensing. *Nano Lett.* **6,** 2368–2374 (2006).

41. Yamada, K. K. and N. S. and K. K. and K. M. and H. Nanoscale liquid droplet deposition using the ultrasmall aperture on a dynamic mode AFM tip. *Nanotechnology* **22,** 175301 (2011).

42. Espinosa, N. M. and K.-H. K. and H. D. A multi-ink linear array of nanofountain probes. *J. Micromechanics Microengineering* **16,** 1935 (2006).

43. Kim, K.-H. *et al.* Direct Delivery and Submicrometer Patterning of DNA by a Nanofountain Probe. *Adv. Mater.* **20,** 330–334 (2008).

44. Loh, O. *et al.* Nanofountain-Probe-Based High-Resolution Patterning and Single-Cell Injection of Functionalized Nanodiamonds. *Small* **5,** 1667–1674 (2009).

3 Confocal Microscopy Detection

In this thesis complementary advanced methods based on fluorescence microscopy were employed. These methods were used to quantitatively monitor molecular interactions within confined environment simultaneously with morphological information. Fluorescence and Laser Scanning Confocal Microscopy are briefly described together with Raster Image Correlation Spectroscopy here used to measure diffusion coefficient and molecular concentration at nanoscale and the Fluorescence Lifetime Imaging Microscopy here used to monitor molecular scale changes occurring in model systems within confined environment.

3.1 Principles of Fluorescence

Fluorescence is the emission of light by molecules of particular species (*fluorophores*), after they were excited by exposure to light of a different wavelength. The quantum mechanical processes involved in fluorescence are illustrated by the Jablonski diagram[1] (**Fig. 3.1)**. The singlet ground, first, and second electronic states are depicted by *S0*, *S1*, and *S2*, respectively. At each of these electronic energy levels the fluorophores can exist in a number of vibrational energy levels, depicted by 0, 1, 2, etc. In this Jablonski diagram a possible number of interactions are excluded, such as quenching, energy transfer and solvent interactions. The transitions between states are depicted as vertical lines to illustrate the instantaneous nature of light absorption. Transitions occur in about 10^{-15} s, a time too short for significant displacement of nuclei, according to the Franck-Condon principle.

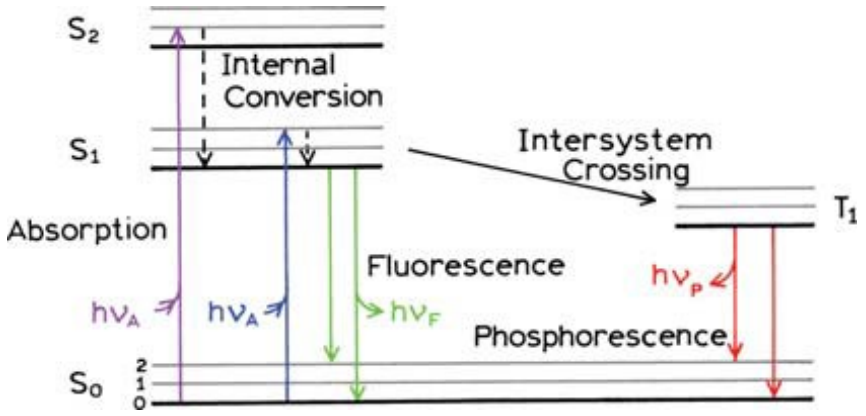

Figure 3.1: A typical Jablonski diagram[1].

Following light absorption, several processes usually occur. A fluorophore is usually excited to some higher vibrational level of either *S1* or *S2*. With a few rare exceptions, molecules in condensed phases rapidly relax to the lowest vibrational level of S1. This process is called internal

conversion and generally occurs within 10^{-12} s or less. Since fluorescence lifetimes are typically near 10^{-8} s, internal conversion is generally complete prior to emission. Hence, fluorescence emission generally results from a thermally equilibrated excited state, that is, the lowest energy vibrational state of *S1*. Return to the ground state typically occurs to a higher excited vibrational ground state level, which then quickly (10^{-12} s) reaches thermal equilibrium.

Molecules in the *S1* state can also undergo a spin conversion to the first triplet state *T1*. Emission from *T1* is termed phosphorescence, and is generally shifted to longer wavelengths (lower energy) relative to the fluorescence. Conversion of *S1* to *T1* is called intersystem crossing. Transition from *T1* to the singlet ground state is forbidden, and as a result the rate constants for triplet emission are several orders of magnitude smaller than those for fluorescence.

Examination of the Jablonski diagram reveals that the energy of the emission is typically less than that of absorption. Fluorescence typically occurs at lower energies or longer wavelengths. This leads to distinct absorption and emission spectra separated by the *Stokes shift*. This is very convenient for fluorescence spectroscopy and microscopy, because the excitation light – if its wavelength is chosen carefully – can be spectrally separated from the fluorescence emission by optical filters, allowing even the detection of light from a single fluorophore.

In condensed phases, after absorption of a photon, almost all excited molecules rapidly relax to the lowest vibrational level of the first excited state, from which they return to the ground state via: nonradiative or radiative decay process. The radiative decay rate Γ depends on the electronic properties of an isolated fluorophore. Molecular interactions, such as dynamic (or collisional) quenching and FRET, are accounted for in the nonradiative decay rate k_{nr}.

Figure 3.2 is a simplified version of a Jablonski diagram that best represented the meanings of quantum yield and lifetime, perhaps the most important characteristics of a fluorophore.

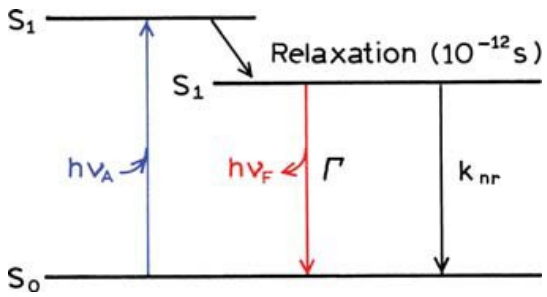

Figure 3.2: A simplified Jablonski diagram to illustrate the meaning of quantum yields and lifetimes[1].

The fluorescence quantum yield is the number of emitted photons relative to the number of absorbed photons. The rate constants Γ and k_{nr} both depopulate the excited state. The fraction of fluorophores that decay through emission, and hence the quantum yield, is given by:

$$Q = \frac{\Gamma}{\Gamma + k_{nr}} \tag{3.1}$$

The quantum yield can be close to unity if the radiationless decay rate is much smaller than the rate of radiative decay, that is $k_{nr} < \Gamma$. Substances with the largest quantum yields, approaching unity, display the brightest emissions.

The lifetime of the excited state is defined by the average time the molecule spends in the excited state prior to return to the ground state. It determines the time available for the fluorophore to interact with or diffuse in its environment, and hence the information available from its emission and is defined as:

$$\tau = \frac{1}{\Gamma + k_{nr}} \tag{3.2}$$

The lifetime of the fluorophore in the absence of nonradiative processes is called natural lifetime, and is given by:

$$\tau_n = \frac{1}{\Gamma} \tag{3.3}$$

The emission probability is constant in time, which results in an exponential fluorescence intensity decay for an ensemble of fluorophores:

$$I(t) = I_0 e^{-\frac{t}{\tau}} \tag{3.4}$$

where I_0 is the emission intensity for $t = 0$ and τ is the lifetime.

Fluorescence lifetime is an intrinsic property of a fluorophore and is insensitive to a variety of intensity-based artifacts. Factors such as variations in excitation source intensity, detection gain setting, optical loss in the optical path and/or sample, variation in sample fluorophore concentration, photobleaching and microscope focusing will all affect measured fluorescence intensities, but will leave the intrinsic excited-state fluorophore lifetime unchanged[2]. Quenching of the excited state by external factors decreases the fluorescence lifetime that is sensitive to the fluorophore's microenvironment, including factors such as temperature, pH, oxygen concentration, polarity, molecular associations (binding), ion concentration, and relaxation through collisional (dynamic) quenching and FRET, and is therefore used as a parameter for biological sensors[3].

Fluorescence quenching is generally classified into two primary types: static and dynamic (**Fig. 3.3)**[4]. Static quenching occurs due to the formation of nonfluorescent complexes via the interaction between fluorophores and other molecules in solution known as quenchers. Fluorescence lifetime imaging is insensitive to static quenching, as other unbound (hence still fluorescent) fluorophores retain their fluorescent properties. On the other hand, dynamic (or collisional) quenching happens during the fluorescence decay process, when some excited-state fluorophores are de-excited upon

contact with the quenchers and follow a nonradiative decay process, which leads to a faster decay of excited-state fluorophore population and hence a shorter fluorescence lifetime.

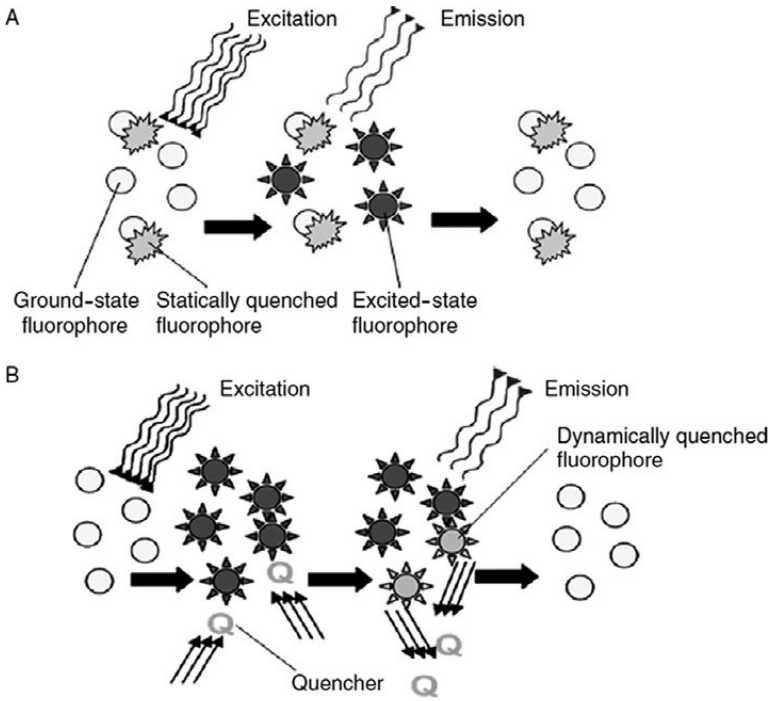

Figure 3.3: Static quenching (A) occurs due to the formation of nonfluorescent complexes from the interaction between fluorophores and other molecules in solution known as quenchers. On the other hand, dynamic quenching (B) happens during the decay process, when excited-state fluorophores are de-excited upon contact with the quenchers. As a result, detected lifetime will be shortened[4].

Therefore, changes of lifetime values are interpreted in terms of molecular interactions[5,6] and is a valuable tool to assess changes of the local molecular environment in the direct vicinity of fluorescently labeled molecules. Depending on the structure of the fluorophore, dyes can be sensitive to very different parameters. Examples are monitoring the concentration of Calcium ions (Ca^{2+})[7,8,9], pH[10,11,12], oxygen[13,14,15], NADH [16,17] or Chloride (Cl^-) [18,19].

A special case for the influence of the local environment on fluorescence lifetime is Förster Resonance Energy Transfer (FRET), where the donor dye is quenched by the presence of an acceptor dye. Förster Resonance Energy Transfer (FRET) has become a valuable standard tool in cell biology to localize molecular interactions. The phenomenon of energy transfer from the donor fluorophore to a suited acceptor molecule in close proximity results in excitation of the acceptor without acceptor exciting laser light. FRET then causes a decrease in the donor emission and an increase in acceptor emission. Energy transfer can only occur when the donor emission and the acceptor excitation spectrum overlap and donor and acceptor fluorophore are in close proximity, usually less than 10 nm. Applying an intramolecular labelling approach, the distance between the dye and the quencher or FRET acceptor can also vary along with different conformations of the

labeled biomolecule. In this way, intramolecular changes, e.g. due to folding or action of molecular motors, are detectable.

From a mechanistic point of view, mainly FRET sensors are used, but also electron transfer is a suitable quenching mechanism and even more sensitive to conformational changes. Many dyes are quenched by the DNA base guanosin, which can be exploited in DNA hairpin sensors. They become unquenched when the probe binds to a DNA with a complementary sequence[20]. In protein studies, mainly tryptophan is known as an effective quencher which allows for analysis of protein dynamics[21].

3.2 Laser Scanning Confocal Microscopy (LSCM)

Fluorescence confocal microscopy is an imaging methods which brings optical microscopy resolution close to theoretical limits imposed by diffraction of light. It several advantages over conventional optical microscopy, including the ability to control depth of field, the elimination or reduction of background information away from the focal plane that leads to image degradation, and the capability to collect serial optical sections from thick specimens. The basic key to the confocal approach is the use of spatial filtering techniques to eliminate out-of-focus light or glare in specimens whose thickness exceeds the immediate plane of focus. The image has less haze and better contrast than that of a conventional microscope and represents a thin cross-section of the specimen. Thus, apart from allowing better observation of fine details it is possible to build three-dimensional reconstructions of a volume of the specimen by assembling a series of thin slices taken along the vertical axis[22].

There has been a tremendous explosion in the popularity of confocal microscopy in recent years, due in part to the relative ease with which extremely high-quality images can be obtained from specimens prepared for conventional fluorescence microscopy, and the growing number of applications in cell biology that rely on imaging both fixed and living cells and tissues. In fact, confocal technology is proving to be one of the most important advances ever achieved in optical microscopy.

When fluorescent specimens are imaged using a conventional widefield optical microscope secondary fluorescence emitted by the specimen that appears away from the region of interest often interferes with the resolution of those features that are in focus. This occurs in thick samples (micron scale). In a conventional widefield microscope, the entire specimen is illuminated by a mercury or xenon lamp, and the image can be viewed directly by eye or projected directly onto an image capture device or photographic film. In LSCM measures the illumination is achieved by scanning a laser beam across the specimen, and the light coming from each illuminated area as a function of time is collected by the detector in selected spectral range and the image is digitalised

pixel by pixel. This method has facilitated imaging of living specimens, enabled the automated collection of three-dimensional data and time lapses, and improved the images obtained of specimens using multiple labeling.

3.2.1 Confocal microscope configuration

The confocal principle in laser scanning microscope is presented in **figure 3.4**. Coherent light emitted by the laser system (excitation source) passes through a pinhole aperture that is situated in a conjugate plane (confocal) with a scanning point on the specimen and a second pinhole aperture positioned in front of the detector (a photomultiplier tube). This pinhole aperture is at the basis of confocal measurements as it cut all out of focus contributions. As the laser is reflected by a dichromatic mirror and scanned across the specimen in a defined focal plane, fluorescence emitted from points on the specimen (in the same focal plane) pass back through the dichromatic mirror and are focused as a confocal point to the detector pinhole aperture.

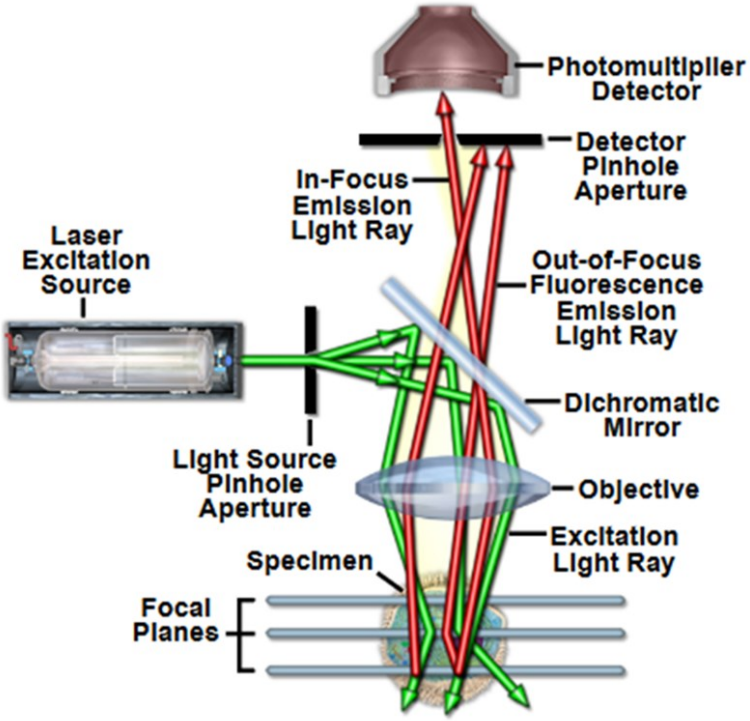

Figure 3.4: Principal light pathways in confocal microscope configuration[23].

The fluorescence signal that occurs at points above and below the objective focal plane is not confocal with the pinhole (termed *Out-of-Focus Light Rays*) and forms extended Airy disks in the aperture plane. Because only a small fraction of the out-of-focus fluorescence emission is delivered through the pinhole aperture, most of this extraneous light is not detected by the photomultiplier and does not contribute to the resulting image.

Today, lasers are usually chosen as illumination sources for a confocal microscope, because the

coherent light that they produce can be collimated very accurately with a Gaussian beam shape and can therefore also be used to create a diffraction limited illumination spot in the focal plane. Furthermore, their highly monochromatic light can easily be filtered out to separate excitation from emission light. An objective designed to have an immersion medium, typically water or a special immersion oil, between the objective surface and the glass cover slip, is preferably used to focus the light into the sample. That way, interfaces with a high difference in refractive index can be avoided, which increases the numerical aperture N_A. N_A is a dimensionless quantity that specifies the maximum angle that the objective can still observe. A high N_A is preferable to focus the light into the sample, because the size of the focus is reciprocal to N_A. Since above and below the focal plane, increasingly large areas of the sample are also illuminated by the defocused excitation light, a second optical element is necessary to implement confocal microscopy.

The aim of confocal microscopy is to achieve an optimized optical resolution in all three spatial dimensions compared to standard light microscopy. Its basic concept is to observe the fluorescence intensity consecutively in very small pixels of the sample, out of which a complete raster image or even a three dimensional sample reconstruction can be composed. This is achieved by combining a strongly focused illumination with fluorescence detection through a very small aperture, the *confocal pinhole*. The minimal size that the light can be focused to determines the optical resolution of the system. The focal size and thereby the optical resolution R is limited by the Abbe limit to a diameter of around 200 nm, depending on the wavelengths used.

3.2.2 Properties of confocal microscopy

The primary advantage of laser scanning confocal microscopy is the ability to serially produce thin (0.5 to 1.5 μm) optical sections through fluorescent specimens that have a thickness ranging up to 50 μm or more. The image series is collected by coordinating incremental changes in the microscope fine focus mechanism (using a stepper motor) with sequential image acquisition at each step. Image information is restricted to a well-defined plane, rather than being complicated by signals arising from remote locations in the specimen. Contrast and definition are dramatically improved over widefield techniques due to the reduction in background fluorescence and improved signal-to-noise. Furthermore, optical sectioning eliminates artifacts that occur during physical sectioning and fluorescent staining of tissue specimens for traditional forms of microscopy. The non-invasive confocal optical sectioning technique enables the examination of both living and fixed specimens under a variety of conditions with enhanced clarity.

Furthermore, advances in confocal microscopy have made possible *multi-dimensional views* of living cells and tissues that include image information in the x, y, and z dimensions as a function of time and presented in multiple colours (using two or more fluorophores).

Additional advantages of scanning confocal microscopy include the ability to adjust magnification

electronically by varying the area scanned by the laser without having to change objectives. This feature is termed the *zoom factor*, and is usually employed to adjust the image spatial resolution by altering the scanning laser sampling period.

CoIt has to be taken in account that the presence of pinhole limits the number of photons that reach the detector so that perfect imaging may occur only with bright and stable sample as the laser sources used for exciting the sample may induce phototoxicity.

3.3 Raster Image Correlation Spectroscopy (RICS)

Raster image correlation spectroscopy (RICS) is a new technique for measuring molecular dynamics and concentrations of fluorescence molecules from microscopy images. This technique in principle can be applied on every commercial confocal systems[24]. RICS is a space-time fluorescence correlation technique designed to detect and quantify molecular dynamics in living cells, such as binding, concentration and diffusion properties of molecules diffusing in cytoplasm or in cellular compartments and gives information on dynamical events in each pixel also providing information on their location within the image[24,25,26,]. Recent advances in the speed and sensitivity of LSCM allow then measuring properties such as protein dynamics and aggregation from the careful analysis of these images.

Intensity fluctuations within a focal volume in a biological system can arise from a number of phenomena including the diffusion of molecules through the illumination volume, protein conformational changes, and protein binding to immobile or large cellular structures. To capture and distinguish the subtle differences in the intensity fluctuations due to these cellular phenomena, the ideal correlation technique would have a spatial resolution limited only by light diffraction and would be sensitive to the very wide range of dynamics observed in living cells.

Due to the nature of the scanning mechanism LSCM fluorescence images inherently capture a wide range of dynamic information potentially providing details about underlying biological processes within the cell. As the laser performs the raster scanning movement, it creates a space–time matrix of pixels within the image. Since the temporal and spatial sampling of the laser beam during the raster scanning is known, that is, the time the laser samples each pixel (pixel dwell time); time between scan lines and time between images. Therefore, the images contain information on the microsecond time scale for pixels along the horizontal scanning axis, millisecond time scale along the vertical scanning axis or between scan lines, and on the sub-second to second or longer time scale between successive images. Using the RICS correlation technique it is possible to generate spatial-temporal maps of dynamics occurring on the microseconds to milliseconds time scale across the cell. If the RICS analysis is performed in combination with temporal image correlation spectroscopy (t-ICS)[27], performed between images within an image time series on the seconds time

scale (or longer), then the two methods provide dynamic information from microseconds to minutes or hours. Molecular diffusion coefficients and concentration information is extracted from raster scanned images using RICS analysis.

RICS can be performed on standard confocal images taken from commercial LSCMs opening up this type of analysis to a large number of researchers. In general, commercial LSCMs are sensitive, their operation is automatic and their performance has been optimized due to the large number of manufacturers, their large scale use and long term availability in the marketplace. However, in general the light detection of LSCMs is analogue in which the current of a photomultiplier detector is integrated and sampled at a specific frequency.

3.3.1 RICS basic theory

RICS analysis is performed on images acquired through raster scanning. Laser scanning microscopes generate images by measuring fluorescence intensity across an area one pixel at a time, (a 'pixel' in this context does not have the same definition as a pixel in computer graphics, but rather refers to a localized intensity measurement). The value of a pixel is obtained by illuminating a region of the sample with the focal volume of a laser beam and measuring the intensity of the emitted fluorescence. The laser beam is then moved to a new location and a new pixel is recorded. Each pixel can be considered to correspond to a region of the sample, with its width (called the pixel size) defined by the distance the beam moves between measurements. This means that the size of a pixel is separate and independent from the size of the focal volume of the laser beam[28,29]. The 'raster' in RICS refers to the order in which these pixels are collected to generate an image. The top left pixel is measured first. Thereafter, the top row of pixels is collected from left to right. The laser then travels back to the left of the image without collecting any pixels and begins a second row. Rows are collected in this manner from top to bottom until an entire image is obtained. (**Fig. 3.5**). Because each pixel is collected at a different time, there is temporal information included in each individual image. This is referred to as the 'hidden time structure' and can be used to extract temporal information from the image[30,25].

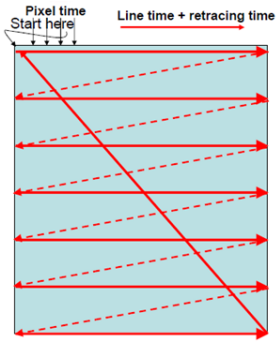

Figure 3.5: Red lines indicate the path of the laser beam in a raster scan during an image capture with an LSCM. Red dashed lines indicate the path where the laser is off and makes a fast shift.

Image autocorrelation is calculated on each image using equation 3.5[31]:

$$G(\xi,\psi) = \frac{\langle \delta i(x,y)\, \delta i\,(x+\xi, y+\psi)\rangle_{x,y}}{\langle i(x,y)\rangle_{x,y}\langle i(x,y)\rangle_{x,y}} \tag{3.5}$$

where $i(x, y)$ is the intensity at each pixel of the image, ξ and ψ are the x and y spatial correlation shifts and $\delta(i) = i - \langle i\rangle$ and $\langle\ldots\rangle$x,y is the spatial average of the image.

The image correlations of all the frames are averaged and the result is fit with an equation relating the correlation to the diffusion coefficient and particle concentration, allowing to derive two fundamental parameters for the molecular dynamic, the molecular diffusion coefficient D and the autocorrelation function amplitude G_0, inversely proportional to the average number of fluorescent particles.

Briefly for raster scanning the spatial component of the correlation function decays due to movement of the laser beam scanning ($S(\xi,\psi)$) is expressed as[24,26]:

$$S(\xi,\psi) = \exp\left(-\frac{\frac{1}{2}\left[\left(\frac{2\xi\delta_r}{\omega_0}\right)^2 + \left(\frac{2\psi\delta_r}{\omega_0}\right)^2\right]}{\left(1+\frac{4D(\tau_p\xi+\tau_l\psi)}{\omega_0^2}\right)}\right) \tag{3.6}$$

where ξ , ψ are the x and y spatial lags in pixels, δr (δx and δy) is the pixel size, τ_p (typically 2 - 20 μs) is the pixel dwell time in x, τ_l is the time between lines in y (typically 1 - 4 ms), ω_0 is the e^{-2} radius of the point spread function of the laser beam (the beam waist). The component of the temporal autocorrelation function (ACF) due to diffusion is the traditional correlation function:

$$G(\xi,\psi) = \frac{\gamma}{N}\left(1+\frac{4D(\tau_p\xi+\tau_l\psi)}{\omega_0^2}\right)^{-1}\left(1+\frac{4D(\tau_p\xi+\tau_l\psi)}{\omega_z^2}\right)^{-1/2} \tag{3.7}$$

where N is the number of particles in the focal volume; D the diffusion coefficient; γ is a shape factor due to uneven illumination across the focal volume and is 0.3535 for a 3D Gaussian under ideal conditions[32]. Also for a 3D Gaussian profile the z-axis beam radius, w_z, is set to 3 ω_0. Thus, $G_{RICS}(\xi,\psi)$ is broken up into two parts: $G(\xi,\psi)$, equation (3.7), which is related to molecular dynamics, and $S(\xi,\psi)$, equation (3.6), which is related to scanning optics. The overall ACF, $Gs(\xi,\psi)$ is given by:

$$G_{RICS}(\xi,\psi) = S(\xi,\psi)\,G(\xi,\psi) \tag{3.8}$$

Equations 3.6 and 3.7 are the most basic form of this function[25,30]. Variations on this equation that

account for factors such as two-photon excitation and membrane-bound diffusion are described elsewhere[25,33].

It should be noted that multiple images are acquired from RICS analysis for two reasons: (i) so that background subtraction can be performed and (ii) to improve the signal-to-noise ratio. Correlation analysis is not performed between images in RICS. This means that all available temporal information comes from within each image.

3.3.2 RICS analysis

In this thesis Raster Image Correlation Spectroscopy is employed to probe protein-ligand interactions in artificial aqueous droplets with a femtoliter scale resolution at a nanomolar concentration. Aqueous droplets are imaged using a laser scanning confocal microscope and collected images are analysed by RICS. In this scenario, RICS represents an ideal transduction method for monitoring molecular binding events in pico- to nano-liter volume droplets.

Beside the very well-known advantages of fluorescence methods, specific properties of RICS allow for the accurate quantification and mapping of molecular diffusion coefficients, in order to estimate fractions of free fluorolabeled ligands and of fluorolabeled ligands bound to the protein[34] at nanomolar concentrations. Blinking and photobleaching events are reduced in with respect to similar techniques like single point Fluorescence correlation Spectroscopy because of the reduced exposition time to laser light of single area and measurable diffusion range is quite wide (from microseconds to seconds) and it is possible to use it to distinguish diffusion from binding, so that a wide range of experiments can be designed for different applications[26].

RICS allows to execute molecular binding assays at lower concentrations and in principle, it would permit to analyse concentrations as low as 2-3 nM [24]. Remarkably, RICS method or other microscopy based fluctuation techniques can be used to monitor cellular events like molecular dynamics in focal adhesions in cells[33,35]. These techniques could be applied also in microfluidic devices to investigate single cell mechano-biology by analysing, for instance, the intracellular signalling exerted by mechano-sensitive ion channels[36].

We here use RICS for the first time to follow molecular dynamics and binding events within confined and scalable artificial single aqueous droplets. Quantitative information on diffusing objects at the nanoscale is obtained simultaneously with spatial information at diffraction limited resolution, so that unsought drop modifications, spatial heterogeneity in the samples or leakage can be readily monitored. RICS allows analysing either the whole drop volume, part of it or the measurement can be extended to multiple different drops in array in a single image.

From the collected images it's possible to generate spatio-temporal maps of dynamics occurring on the microseconds to milliseconds time scale and calculate the spatio-temporal correlation of fluorescence intensity fluctuations (**Fig. 3.6**). They are related to the Brownian motion of particles

in the sample and can arise from a number of phenomena including the entry and transit of molecules through the focal volume, protein conformational changes, molecular binding, aggregation events. So fluctuations reveal the mobility of molecules, and indirectly molecular events, such as the complex formation, within sub-regions of the image.

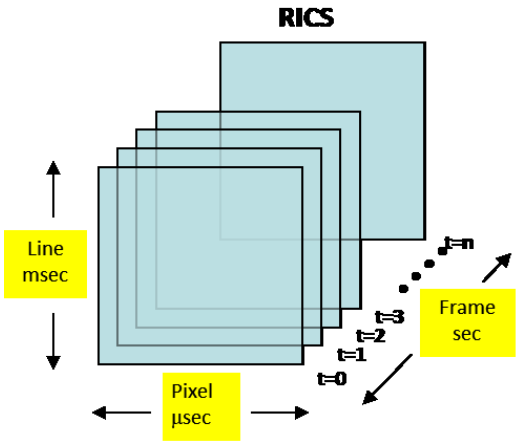

Figure 3.6: Collected images from a laser confocal scanning. For raster-scan patterns, the correlation of a series of images appears on three different timescales: pixels are microseconds-apart in the horizontal direction, milliseconds-apart along the vertical axis (line-to-line), and seconds-apart between successive frames (modified from [25]).

The observation volume is moved across the investigated system and fluorescence intensity is measured in each pixel; the technique is based on the fact that during a raster scan a fast diffusing molecule, for example the free labelled biotin molecule, will be observed across more pixels if compared to a slower one, as the complex between streptavidin and labelled biotin. The higher the diffusion coefficient of molecules in solution more quickly the correlation function decays at short distances (pixels), but is maintained at greater distances (**Fig. 3.7**).

In particular, the analysis of the spatial autocorrelation function using a free diffusion model allows to derive two fundamental parameters for the molecular dynamic, D the molecular diffusion coefficient and G_0 the value of the autocorrelation function amplitude, inversely proportional to the average number of fluorescent particles in the volume under examination.

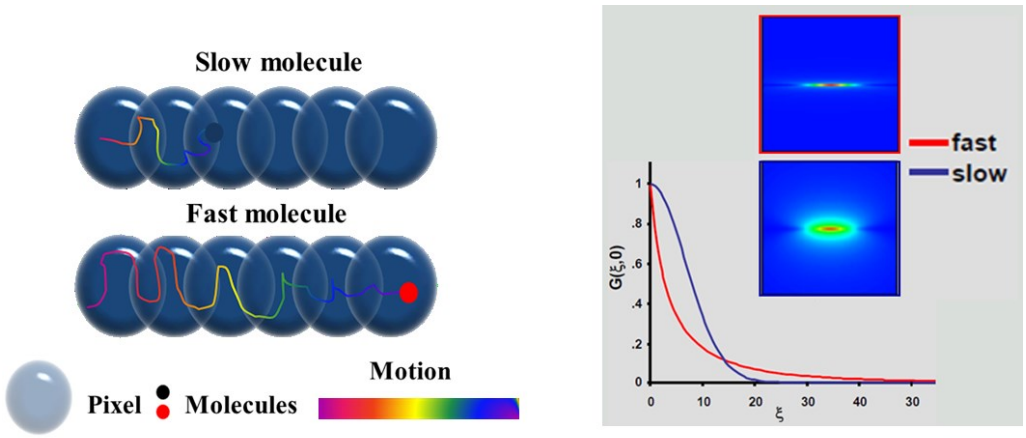

Figure 3.7: Schematic representation of basic idea of RICS technique: during a raster scan a fluorescent particle that moves faster will be observed across more pixels compared to a slower particle. Spatio-temporal correlation of fluorescence intensity fluctuations is calculated from the image and occurs in a scale that depends on the rate of diffusion. In the graph simulated function for molecules with high diffusion coefficient (red line) and low diffusion coefficient (blue line).

3.4 Fluorescence Lifetime Imaging Microscopy (FLIM)

Fluorescence lifetime imaging microscopy (FLIM) is a method for mapping the spatial distribution of nanosecond excited state lifetimes with microscopic spatial resolution, providing a useful tool to detect, visualize and investigate structure and function of biological systems. However, intensity-based measurements are vulnerable to artifacts such as variation in excitation source intensity, detector gain setting, optical loss in the optical path and/or sample, variation in sample fluorophore concentration, photobleaching, and microscope focusing. Further, fluorophores with similar excitation and emission spectra may be impossible to differentiate with steady-state fluorescence intensity imaging.

The fluorescence lifetime is the property describing on average how rapidly an excited-state fluorophore decays, in particular, is the time the fluorophore remains in the excited state before returning to the ground state.

One challenge is that the employed fluorophores need to be distinguishable and have commonly used spectral characteristics. This limits the number of useful fluorescent markers. The analysis of the fluorescence lifetime can help to overcome these limitations, consequently, more fluorophores can be monitored and separated simultaneously within a sample. Additionally, the fluorescence lifetime enables to discriminate label fluorescence from the fluorescence background of the sample (e.g., cell or tissue) and thereby allows a higher detection efficiency and more accurate marker localization.

Because the donor lifetime decreases in the presence of FRET, where the acceptor is the quenching molecule, FLIM offers a solution for quantitative analysis of molecular interactions and requires as control only measuring the fluorescence lifetime of a donor-only labelled sample.

New materials of interest can be new fluorescent labels or quantum dots, which are used in biological imaging as well as in materials sciences. Applications in materials science are mainly focused on the fundamental characterization of new materials[37,38] as used e.g., in photovoltaics[39,40], OLEDs[41], light harvesting materials[42,43] and functionalized surfaces[44,45]. The minor carrier lifetime in semiconductor materials is an important parameter to control or improve the quality of the fabrication procedure.

Accordingly, fluorescence lifetime imaging microscopy enables addressing questions in very different fields of research, and up to now, several thousand papers dealing with fluorescence lifetime measurements have been published. Continuing advances in technology for microscopy and the developing appreciation that fluorescence lifetime is a sensitive means for quantitatively evaluating microenvironment will likely help make FLIM a critical research tool for cell biology by providing new ways for life scientists to detect, visualize, and investigate structure and function in biological systems. The increasing interest in lifetime techniques will trigger new fields of applications, new analysis schemes as well as improvements in the labels, and, in the future, a combination of lifetime measurements with spectral or dynamic information will open promising prospects.

3.4.1 FLIM method and analysis

Fluorescence lifetime microscopy gives information on the characteristics feature of fluorescence decay in each pixel of the image, in particular, using the time-correlated single photon counting technique[46] (TCSPC), one measures the time between sample excitation by a pulsed laser and the arrival of the emitted photon at the detector. TCSPC requires a defined “start” signal, provided by the electronics steering the laser pulse or a photodiode, and a defined “stop” signal, realized by detection with single-photon sensitive detectors. The measurement of this time delay is repeated many times to account for the statistical nature of fluorophore emission. The delay times are sorted into a histogram that plots the occurrence of emission over time after the excitation pulse (**Fig. 3.8**).

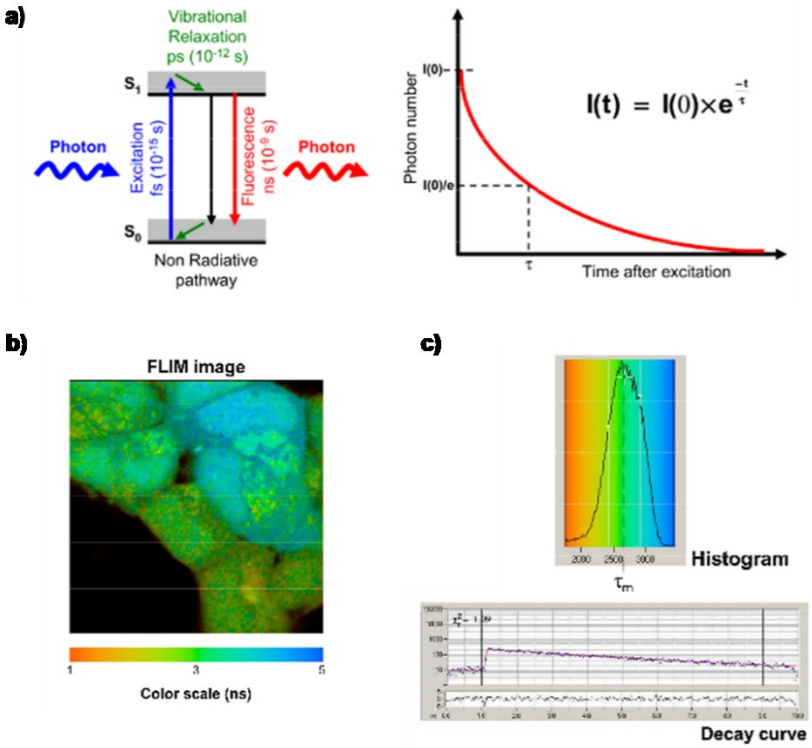

Figure 3.8: a) Exponential decay of fluorescence intensity during a fluorescence process, b) FLIM image reported in lifetime scale, c) time-correlated histogram of counts and decay curve.

In order to acquire a fluorescence lifetime image, the photons have to be attributed to the different pixels, which is done by storing the absolute arrival times of the photons additionally to the relative arrival time in respect to the laser pulse. Line and frame marker signals from the scanner of the confocal microscope are additionally recorded in order to sort the time stream of photons into the different pixels. From a practical point of view, the integration of TCSPC requires a suitable hardware parts[47]: pulsed light sources; appropriate microscopic optics (currently, confocal microscopes from all major microscope manufacturers can be upgraded); single photon detection modules with appropriate sensitivity and time resolution (detectors for FLIM imaging can be photomultiplier tubes, e.g. the PMA series, after pulsing-free hybrid detectors, e.g. PMA Hybrid 40 or avalanche photodiodes); suited timing electronics for data registration; data acquisition and analysis software to produce lifetime histograms, fit to different models, etc. (e.g., the SymPhoTime 64 software).

3.4.2 Phasor approach to FLIM measurements

In FLIM experiments multiple lifetime components arise from different molecular species or different conformations of the same molecule[48,49] and in different pixels of the image. The analysis of FLIM data collected in the time domain then proceeds by fitting multiple decays at each pixel using exponential components and identifying decay times and amplitudes with molecular species and their relative abundances. A problem with this approach is that many of fluorescence

molecules used in microscopy display a complex decay behaviour[50] which may also be environment dependent.

For this reason we decide to use the phasor approach an analysis method developed in 2007[51] which provides a fast, easy and fit free method to evaluate fluorescence lifetimes in each pixel of the image.

The phasor approach has the potential of simplifying the analysis of FLIM images, avoiding technical issues in multiple exponential analysis and provides a graphical global view of the processes affecting the fluorescence decay occurring at each pixel[52,53,54]. The phasor method transforms the histogram of the time delays at each pixel in a phasor. There is a direct relationship between a phasor location and lifetime.

When fluorescence lifetime data are acquired in the time domain, the components *g* (x-coordinate) and *s* (y-coordinate) of the phasor plot are given by the following expressions[55]:

$$g_{i,j}(\omega) = \frac{\int_0^\infty I_{i,j}(t)\cos(\omega t)dt}{\int_0^\infty I_{i,j}(t)dt} \tag{3.9}$$

$$s_{i,j}(\omega) = \frac{\int_0^\infty I_{i,j}(t)\sin(\omega t)dt}{\int_0^\infty I_{i,j}(t)dt} \tag{3.10}$$

where the indices *i* and *j* identify a pixel of the image and ω the frequency ($\omega = 2\pi f$), where *f* is the laser repetition rate (e.g. 80 MHz).

In the phasor plot if the decay is a single exponential $I(t)=Ae^{-t/\tau}$, the coordinates are given by:

$$g(\omega) = \frac{1}{1+(\omega\tau)^2} \tag{3.11}$$

$$s(\omega) = \frac{\omega\tau}{1+(\omega\tau)^2} \tag{3.12}$$

where τ is the lifetime of the decay and ω is the laser frequency.

Every possible lifetime can be mapped into a universal representation of the decay, a two-dimensional histogram called phasor plot, showed in **figure 3.9**.

If the decay is a single exponential, all single exponential components are represented by the "universal circle," defined as a semicircle of center (1/2,0) and radius 1/2 in the phasor plot. Along this semicircle a phasor corresponding to a very short lifetime (small phase angle) is close to the point (1,0), where as a phasor corresponding to a very long lifetime will be close to the (0,0) point ($\tau = 0$ in the point (1, 0) and $\tau = \infty$ in the point (0, 0). If the pixels are located inside the universal circle of the phasor plot, their decay is multiexponential.

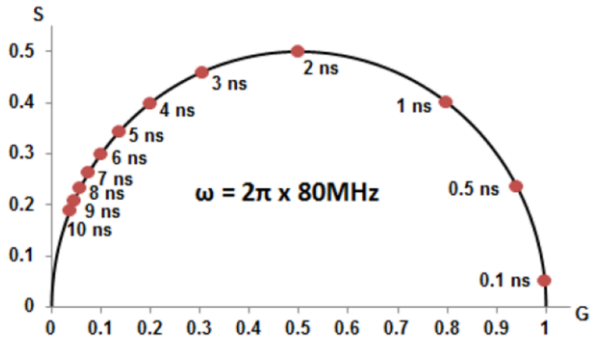

Figure 3.9: Schematic representation of the phasor plot.

Each pixel of the image gives a point in the phasor plot in which we can easily recognize the presence of different molecular species by their position in the plot or the occurrence of fluorescence resonance energy transfer. The analysis of the fluorescence lifetime imaging microscopy data in the phasor space is done observing clustering of pixel values in specific regions of the phasor plot rather than by fitting the fluorescence decay using exponentials, providing a global view of FLIM images. The analysis is instantaneous since is not based on calculations or nonlinear fitting. The phasor approach has the potential to simplify the way data are analyzed in FLIM, paving the way for the analysis of large data sets and, in general, making the interpretation of FLIM data accessible to the non-expert in spectroscopy and data analysis.

Bibliography

1. Lakowicz, J. R. *Principles of Fluorescence Spectroscopy*. (Springer US, 2006).
2. Lloyd, W. R., Wilson, R. H., Chang, C.-W., Gillispie, G. D. & Mycek, M.-A. Instrumentation to rapidly acquire fluorescence wavelength-time matrices of biological tissues. *Biomed. Opt. Express* **1,** 574–586 (2010).
3. Chen, L.-C., Lloyd, W. R., Chang, C.-W., Sud, D. & Mycek, M.-A. Chapter 20 - Fluorescence Lifetime Imaging Microscopy for Quantitative Biological Imaging. in *Digital Microscopy* (eds. Sluder, G. & Wolf, D. E. B. T.-M. in C. B.) **114,** 457–488 (Academic Press, 2013).
4. Chang, C., Sud, D. & Mycek, M. B. T.-M. in C. B. Fluorescence Lifetime Imaging Microscopy. in *Digital Microscopy, 3rd Edition* **81,** 495–524 (Academic Press, 2007).
5. Peyker, A., Rocks, O. & Bastiaens, P. I. H. Imaging Activation of Two Ras Isoforms Simultaneously in a Single Cell. *ChemBioChem* **6,** 78–85 (2005).
6. Peter, M. *et al.* Multiphoton-FLIM Quantification of the EGFP-mRFP1 FRET Pair for Localization of Membrane Receptor-Kinase Interactions. *Biophys. J.* **88,** 1224–1237 (2005).
7. Miyawaki, A. *et al.* Fluorescent indicators for Ca(2+) based on green fluorescent proteins and calmodulin. *Nature* **388,** 882 (1997).
8. Mank, M. *et al.* A FRET-Based Calcium Biosensor with Fast Signal Kinetics and High Fluorescence Change. *Biophys. J.* **90,** 1790–1796 (2006).
9. Celli, A. *et al.* The Epidermal Ca(2+) Gradient: Measurement Using the Phasor Representation of Fluorescent Lifetime Imaging. *Biophys. J.* **98,** 911–921 (2010).
10. Hille, C. *et al. Time-domain fluorescence lifetime imaging for intracellular pH sensing in living tissues*. *Analytical and bioanalytical chemistry* **391,** (2008).
11. Sanders, R., Draaijer, A., Gerritsen, H. C., Houpt, P. M. & Levine, Y. K. Quantitative pH Imaging in Cells Using Confocal Fluorescence Lifetime Imaging Microscopy. *Anal. Biochem.* **227,** 302–308 (1995).
12. Lin, H.-J., Herman, P. & Lakowicz, J. R. Fluorescence lifetime-resolved pH imaging of living cells. *Cytom. Part A* **52A,** 77–89 (2003).
13. Gerritsen, H. C., Sanders, R., Draaijer, A., Ince, C. & Levine, Y. K. Fluorescence lifetime imaging of oxygen in living cells. *J. Fluoresc.* **7,** 11–15 (1997).
14. Sud, D. *et al.* Optical imaging in microfluidic bioreactors enables oxygen monitoring for continuous cell culture. **11,** 50503–50504 (2006).
15. Sud, D. & Mycek, M.-A. Calibration and validation of an optical sensor for intracellular oxygen measurements. **14,** 20503–20506 (2009).
16. Lakowicz, J. R., Szmacinski, H., Nowaczyk, K. & Johnson, M. L. Fluorescence lifetime imaging of free and protein-bound NADH. *Proc. Natl. Acad. Sci. U. S. A.* **89,** 1271–1275 (1992).
17. Ketteler, A. von, Siegberg, D., Herten, D. P., Horn, C. & Petrich, W. Fluorescence lifetime-based glucose sensor using NADH. in **8229,** 82290P–8229–8 (2012).
18. Lahn, M., Dosche, C. & Hille, C. Two-photon microscopy and fluorescence lifetime imaging reveal stimulus-induced intracellular Na+ and Cl− changes in cockroach salivary

acinar cells. *Am. J. Physiol. - Cell Physiol.* **300,** C1323 LP-C1336 (2011).

19. Ruedas-Rama, M. J., Orte, A., Hall, E. A. H., Alvarez-Pez, J. M. & Talavera, E. M. A chloride ion nanosensor for time-resolved fluorimetry and fluorescence lifetime imaging. *Analyst* **137,** 1500–1508 (2012).

20. Piestert, O. *et al.* A Single-Molecule Sensitive DNA Hairpin System Based on Intramolecular Electron Transfer. *Nano Lett.* **3,** 979–982 (2003).

21. Marmé, N., Knemeyer, J.-P., Sauer, M. & Wolfrum, J. Inter- and Intramolecular Fluorescence Quenching of Organic Dyes by Tryptophan. *Bioconjug. Chem.* **14,** 1133–1139 (2003).

22. Semwogerere, D. & Weeks, Eric, R. Confocal Microscopy. in *Encyclopedia of Biomaterials and Biomedical Engineering, Biomaterials, Biomedical Engineering. Informa Healthcare* (2005).

23. Introductory Confocal Concepts. Available at: http://www.microscopyu.com/articles/confocal/confocalintrobasics.html.

24. Brown, C. M. *et al.* Raster image correlation spectroscopy (RICS) for measuring fast protein dynamics and concentrations with a commercial laser scanning confocal microscope. *J. Microsc.* **229,** 78–91 (2008).

25. Digman, M. A. *et al.* Measuring Fast Dynamics in Solutions and Cells with a Laser Scanning Microscope. *Biophys. J.* **89,** 1317–1327 (2005).

26. Rossow, M. J., Sasaki, J. M., Digman, M. A. & Gratton, E. Raster image correlation spectroscopy in live cells. *Nat. Protoc.* **5,** 1761–1774 (2010).

27. Wiseman, P. W., Squier, J. A., Ellisman, M. H. & Wilson, K. R. Two-photon image correlation spectroscopy and image cross-correlation spectroscopy. *J. Microsc.* **200,** 14–25 (2000).

28. Pawley, J. B. *Handbook of Biological Confocal Microscopy*. (Springer, New York, USA, 2006).

29. Webb, R. H. Confocal optical microscopy. *Reports Prog. Phys.* **59,** 427 (1996).

30. Digman, M. A. *et al.* Fluctuation Correlation Spectroscopy with a Laser-Scanning Microscope: Exploiting the Hidden Time Structure. *Biophys. J.* **88,** L33–L36 (2005).

31. Petersen, N. O., Höddelius, P. L., Wiseman, P. W., Seger, O. & Magnusson, K. E. Quantitation of membrane receptor distributions by image correlation spectroscopy: concept and application. *Biophys. J.* **65,** 1135–1146 (1993).

32. Chen, Y. Analysis and applications of fluorecence fluctuation spectroscopy; PhD Thesis. (University of Illinois, 1999).

33. Digman, M. A. & Gratton, E. Analysis of diffusion and binding in cells using the RICS approach. *Microsc. Res. Tech.* **72,** 323–332 (2009).

34. Krichevsky, O. Fluorescence correlation spectroscopy: the technique and its applications. *Reports Prog. Phys.* **65,** 251–297 (2002).

35. Digman, M. A., Brown, C. M., Horwitz, A. R., Mantulin, W. W. & Gratton, E. Paxillin Dynamics Measured during Adhesion Assembly and Disassembly by Correlation Spectroscopy. *Biophys. J.* **94,** 2819–2831 (2016).

36. Soffe, R. *et al.* Analysing calcium signalling of cells under high shear flows using discontinuous dielectrophoresis. *Sci. Rep.* **5,** 11973 (2015).

37. Čeklovský, A., Czímerová, A., Lang, K. & Bujdak, J. *Layered silicate films with photochemically active porphyrin cations*. *Pure and Applied Chemistry - PURE APPL CHEM* **81,** (2009).

38. Folmar, M. *et al.* Metal enhanced fluorescence of Me-ADOTA·Cl dye by silver triangular nanoprisms on a gold film. *Chem. Phys. Lett.* **531,** 126–131 (2012).

39. Ahrenkiel, R. K., Call, N., Johnston, S. W. & Metzger, W. K. Comparison of techniques for measuring carrier lifetime in thin-film and multicrystalline photovoltaic materials. *Sol. Energy Mater. Sol. Cells* **94,** 2197–2204 (2010).

40. Keyes, B. M., Dippo, P., Metzger, W. K., AbuShama, J. & Noufi, R. Changes in the dominant recombination mechanisms of polycrystalline Cu(In,Ga)Se2 occurring during growth. *J. Appl. Phys.* **94,** 5584–5591 (2003).

41. Huang, J.-H., Chien, F.-C., Chen, P., Ho, K.-C. & Chu, C.-W. Monitoring the 3D Nanostructures of Bulk Heterojunction Polymer Solar Cells Using Confocal Lifetime Imaging. *Anal. Chem.* **82,** 1669–1673 (2010).

42. Ghiggino, K. P., Bell, T. D. M. & Hooley, E. N. Synthetic polymers for solar harvesting. *Faraday Discuss.* **155,** 79–88 (2012).

43. Giansante, C. *et al.* White-Light-Emitting Self-Assembled NanoFibers and Their Evidence by Microspectroscopy of Individual Objects. *J. Am. Chem. Soc.* **133,** 316–325 (2011).

44. Grate, J. W., Kelly, R. T., Suter, J. & Anheier, N. C. Silicon-on-glass pore network micromodels with oxygen-sensing fluorophore films for chemical imaging and defined spatial structure. *Lab Chip* **12,** 4796–4801 (2012).

45. López-Gejo, J., Haigh, D. & Orellana, G. Relationship between the Microscopic and Macroscopic World in Optical Oxygen Sensing: A Luminescence Lifetime Microscopy Study. *Langmuir* **26,** 2144–2150 (2010).

46. Becker, W. *et al.* Fluorescence lifetime imaging by time-correlated single-photon counting. *Microsc. Res. Tech.* **63,** 58–66 (2004).

47. Trautmann, S. *et al.* Fluorescence Lifetime Imaging (FLIM) in Confocal Microscopy Applications: An Overview. Available at: https://www.picoquant.com/images/uploads/page/files/7350/appnote_flim_overview.pdf.

48. Peter, M. & Ameer-Beg, S. M. Imaging molecular interactions by multiphoton FLIM. *Biol. Cell* **96,** 231–236 (2004).

49. Wouters, F. S., Verveer, P. J. & Bastiaens, P. I. H. Imaging biochemistry inside cells. *Trends Cell Biol.* **11,** 203–211 (2017).

50. Suhling, K. *et al.* Imaging the environment of green fluorescent protein. *Biophys. J.* **83,** 3589–3595 (2002).

51. Digman, M. A., Caiolfa, V. R., Zamai, M. & Gratton, E. The Phasor Approach to Fluorescence Lifetime Imaging Analysis. *Biophys. J.* **94,** L14–L16 (2008).

52. Jameson, D. M., Gratton, E. & Hall, R. D. The Measurement and Analysis of Heterogeneous Emissions by Multifrequency Phase and Modulation Fluorometry. *Appl. Spectrosc. Rev.* **20,** 55–106 (1984).

53. Clayton, A. H. A., Hanley, Q. S. & Verveer, P. J. Graphical representation and multicomponent analysis of single-frequency fluorescence lifetime imaging microscopy data. *J. Microsc.* **213,** 1–5 (2004).

54. Redford, G. I. & Clegg, R. M. Polar Plot Representation for Frequency-Domain Analysis of Fluorescence Lifetimes. *J. Fluoresc.* **15,** 805 (2005).

55. Stringari, C. *et al.* Phasor approach to fluorescence lifetime microscopy distinguishes different metabolic states of germ cells in a live tissue. *Proc. Natl. Acad. Sci.* **108,** 13582–13587 (2011).

III Experimental Part

4 Confined Aqueous Compartments by Raster Image Correlation Spectroscopy (CADRICS)

This chapter reports a general methodology to produce by inkjet printing miniaturized oil/surfactant confined aqueous compartments up to the hundreds picoliter scale with subsequent investigation of molecular interactions in a space- and time- dependent fashion by Raster Image Correlation Spectroscopy (RICS), a technique specifically suited for monitoring molecular dynamics events in the living cells. The methodology was named CADRICS – i.e. Confined Aqueous Droplet Raster Image Correlation Spectroscopy.

The assembly of scalable liquid compartments for binding assays in array formats constitutes a topic of fundamental importance in life sciences. This challenge can be addressed by mimicking the structure of cellular compartments with biological native conditions. Unlikely, their realization by printing techniques often requires high-boiling viscous additives such as glycerol in order to get stable micro-spots[1] but this affect the native conditions. As a possible alternative we proposed the dispersion of water-based droplets in immiscible oil phases. In this way, aqueous-phase droplets result completely stable against evaporation[2]. By ligand-binding experiments and displacement tests, we clearly demonstrate the high potentiality and capabilities of this miniaturized approach to mimic cellular-like small compartments directly obtaining the read-out of relevant dynamic and thermodynamic parameters such as molecular diffusion coefficients and molecular concentrations, to study intermolecular interaction in confined environments of tunable volume (up to hundreds of picoliters) and at very low concentrations (nanomolar) and to determine the behaviour of few molecular systems (in principle those contained in 10-100 femtoliter volume) monitoring complexes formation and stoichiometry.

In order to validate this methodology, we employed the Alexa 647 dye and the biotin/streptavidin model interaction system. However, the bioarrays could be employed to study complex systems containing different interacting species, including biological macromolecules.

CADRICS approach may constitute a breakthrough for the field of biochips and droplet arrays technological platforms, since for the first time few molecular events are detected on engineered artificial platforms avoiding interfacial effects by solid surfaces or evaporating drops.

4.1 Materials and Methods

4.1.1 Chemicals and solutions preparation

Water-in-oil droplet microarrays have been fabricated on coverslip glasses (Corning 24 x 50 mm, Cover Glass) made from borosilicate glass (0.13-0.16 thick) which are compatible with confocal microscopy set-ups.

All solutions were prepared in ultrapure Millipore water (Direct Q-UV filtration system, 18.2 MΩ•cm). pH was controlled by the pH meter, pH 700, Eutech Instruments. Stock solutions of Atto655-biotin, BTN*, (BioReagent, suitable for fluorescence, Sigma Aldrich) were prepared in anhydrous DMSO and diluted in phosphate buffer solution 100 mM (pH 7.4). Stock solutions of Alexa 647 (Alexa Fluor® 647 carboxylic acid, succinimidyl ester, ThermoFisher Scientific), and Streptavidin, STV, from Streptomyces avidinii (affinity purified, lyophilized from 10 mM potassium phosphate, Sigma Aldrich) were prepared in the same phosphate buffer solution 100 mM.

Streptavidin/Atto655-biotin incubation was carried out 30 minutes at room temperature in the phosphate buffer. Displacement assays of Atto655 biotin/ biotin were carried out by taking constant Atto655 biotin and Streptavidin concentration in the solution (i.e. 40 nM and 10 nM) and varying unlabelled biotin concentration (in the range from 40 nM to 320 nM).

4.1.2 Functionalization of glass surfaces

Glass coverslips were extensively rinsed in ethanol and water to remove organic contaminants. After that they were treated with a UV Ozone Cleaner – ProCleaner (Bioforce Nanosciences) for 30’ in order to increase the hydrophylicity of the surface. Subsequently, the coverslips were coated with 1H,1H,2H,2H-perfluorooctyltriethoxysilane (2% v/v in ethanol) by using a sandwich incubation method[3] for 1 hour at room temperature (**Fig. 4.1)**. Subsequently to coating with 1H,1H,2H,2H-perfluorooctyltriethoxysilane (Sigma Aldrich), the slides were washed with ethanol and put in oven at 110 °C for 1 hour. After that, the coverslips are stored dry at -20°C until use. Contact angles are measured with optical apparatus OCA 20, Data Physics Instruments by using a 10 μL droplet. Water contact angle is 47° ± 2, whereas mineral oil contact angle is 28° ± 2. Each value is average of three measurements. The slight hydrophobicity of the surface allows for preventing excessive aqueous droplets spreading on glass surface.

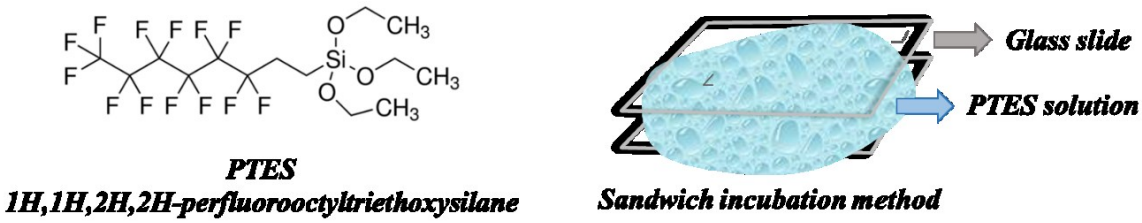

PTES
1H,1H,2H,2H-perfluorooctyltriethoxysilane

Sandwich incubation method

Figure 4.1: Glass surfaces functionalization with PTES solution 2% v/v in ethanol.

4.1.3 Molecular inkjet dispensing

Picoliter droplets were dispensed on glass substrates by using the Dimatix Materials Printer DMP-2800 Fuji Film in **figure 4.2**. This instrument was equipped with user fillable piezo-driven inkjet print cartridges, each with 16 nozzles 254 μm spaced and 21.5 μm in diameter. The droplets were emitted at a jetting frequency of 5 kHz with typical flow rates of 10 pL/10 μs (i.e. 1 μL/s) (considering the times necessary for the formation of a single droplet).

Figure 4.2: Dimatix Materials Printer DMP-2800 and Dimatix Cartridge DMC-11610, Fuji Film.

Mineral oil droplets (light oil (neat) suitable for mouse embryo cell culture Sigma Aldrich, M8410) were dispensed by using double pulse waveform signal at temperatures of 33 °C at voltages between 28 V and 30 V. An ensemble of 1000 droplets of oil (drop-to-drop pitch of 5 μm) formed a single droplet of 10 nL by coalescence. On the top of these droplets, aqueous droplets were dispensed by using single pulse waveforms at room temperature and at voltages between 18 V and 20 V. 100 droplets of aqueous ink (drop-to-drop pitch of 5 μm) were printed in order to form a single liquid droplet of 1 nL. The liquid droplet was completely engulfed inside the mineral oil, lying at the interface with the glass surface. Droplet roundness was evaluated by measuring scale invariance, i.e. the ratio of the radius of the largest circle contained by droplet to that of the smallest circle containing the same droplet[4]. This parameter is a measure of the roundness, comprised between 0 to 1.

Figure 4.3 reports the novel bioarray platform defined as Confined Aqueous Droplets investigated by RICS (hereafter CADRICS). Accordingly, low volume aqueous droplets containing protein

targets are firstly developed by Inkjet Printing. We fabricated microarrays in the form of a 3x2 format drop-to-drop spacing of 1 mm. Nano-liter scale mineral oil droplet arrays are assembled on glass surfaces through picoliter droplets coalescence. Then 1 nL aqueous droplets containing target molecules are injected into the mineral oil droplets. In other experiments, we decreased the number of aqueous coalesced droplets up to 10, in order to obtain liquid aqueous droplets of 100 pL.

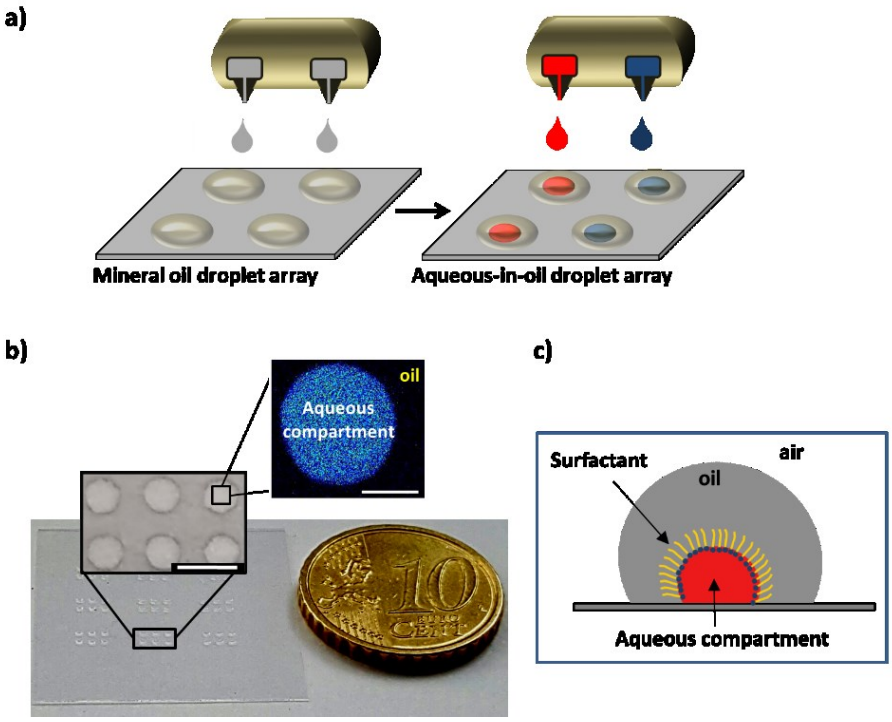

Figure 4.3: Inkjet printing confined aqueous compartments. (a) Inkjet printing is used for direct deposition of nanoliter scale oil droplets and subsequent encapsulation of picoliter scale aqueous droplets to form addressable independent aqueous compartments containing molecular targets (red and blue droplets on glass surfaces. The water-oil interface is stabilized by amphyphilic molecules which are compatible with biomolecules. (b) Optical image with inset (scale bar 1 mm) of a typical droplet array. The inset on the top-right shows the confocal fluorescence microscopy image (scale bar 100 µm) where fluorescence signal is obtained under appropriate excitation conditions. No fluorescence signal is observed in the oil phase around the aqueous droplet. (c) Representation of aqueous confined compartment with water/oil interface stabilization by surfactant molecules.

Fluorescence signal is used to visualise the aqueous compartment encapsulated within the oil droplet (**Fig. 4.3b**). As it can be seen, the droplet in fluorescence image is well-defined in shape and no leakage (i.e. molecular diffusion from aqueous compartment into oil) is observed for several hours. In particular, water-soluble amphiphilic molecules are used to stabilize the water/oil interface (**Fig. 4.3c**) avoiding both water in oil leaking effects[2] and the formation of colloidal aggregates which can significantly affect the assay specificity[5]. In this regard, we took advantage of Tween-20 (Polyoxyethylene (20) sorbitan monolaurate, Sigma Aldrich), a very mild nonionic

surfactant, known for its excellent compatibility with proteins and biomolecules in aqueous phase. Tween-20 possesses a high HLB (i.e. Hydrophile-Lipophile Balance) value equal to 16.7, being well soluble in aqueous phase and lying at the interface between aqueous and oil phases[6].

4.1.4 RICS setup and analysis

Images were acquired in one channel with an Olympus FluoView1200 confocal laser scanning microscope (Olympus, Japan**, Fig.4.4**) using 40X 1.2 NA objective. We used 635 nm laser to excite Atto 655 and Alexa 647 dyes. The bandwidth of the emission filter used for the red emission channel is 655-755 nm. Data were collected in the photon-counting mode. The scan area was 256x256 pixels and pixel size was set at 0.05 μm. 70 frames were collected for each image stack. The excitation volume was calibrated using a solution of Alexa 647 in phosphate buffer at pH 7.4. The diffusion coefficient of the dye was set to 300 $\mu m^2/s$ to determine the waist (ω_0) of the laser beam which resulted ω_0 = 0.35 μm. Scan speed of 4 μs/pixel, (line time was 2.120 ms and frame time was 0.564 s) was used for Atto 655 Biotin molecules and Alexa 647 dye, and 12.5μs/pixel, (line time was 4.325 ms and frame time was 1.15 s) for the complex between BTN* and STV.

Figure 4.4: Olympus FluoView1200 confocal laser scanning microscope (Olympus, Japan).

Droplets confocal images were exported with FV10-ASW 4.1 Viewer. Analysis was performed using the RICS algorithm of SimFCS 3.0 program. RICS autocorrelation function can be fitted using the diffusion model to calculate the characteristic parameters of the process: G(0) and D. Molecular diffusion coefficients and G(0) values were obtained as average of 10 measurements on different droplets. By means of the images processing and analysis program Image J we obtained the parameters related to the size and shape of the 1 nL droplets encapsulated with inkjet printing

into mineral oil droplets. From 10 fluorescence images of aqueous droplets in oil, we obtained average values of diameter and perimeter of 220 µm ± 30 µm and 690 µm ± 70 µm, respectively. Furthermore, from the ratio between the inscribed circle and the circumcircle to the drop, we could evaluate the circularity of the drops, which is 0.88 ± 0.01.

The read out in CADRICS is shown in **figure 4.5**. Aqueous droplets are imaged using a standard fluorescence confocal microscope (**Fig. 4.5a**). Collected images stacks are analysed using RICS and reveal the free diffusion of fluorescent molecules uniformly distributed in the droplets. After removing stationary objects by background subtraction, image autocorrelation is calculated on each fluorescence collected image. The image correlations of all the stacks are averaged and the result is fit with an equation which takes into account the diffusion coefficient (D) and particle concentration in the form of the amplitude G(0) of the autocorrelation function that is proportional to the inverse of the average number of fluorescent particles in the measurement volume[7,8]. By nano- to hundred pico-liters aqueous droplets at nanomolar molecular concentration ranges (i.e. 10^7-10^5 molecules), CADRICS allows gaining information on molecular events occurring in the micro-millisecond time scale (**Fig. 4.5b** and **Fig. 4.5c**).

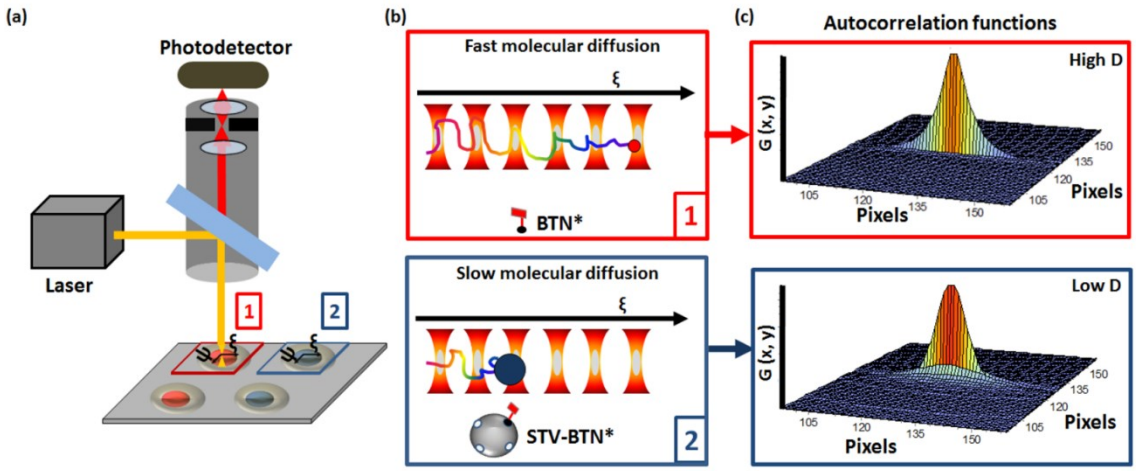

Figure 4.5: Schematic representation of the detection method for protein binding assays in small volume aqueous compartments. (a) Raster scanned image stacks of the droplets are acquired. The observation volume is moved across the droplet and intensity is measured in each pixel, a fast diffusing molecule (e.g. free BTN*) is observed across a larger number of pixels if compared to a slower one (i.e. STV-BTN* complex). (b) Schematic representation of basic idea of RICS technique: during a raster scan a fluorescent particle that moves faster (BTN*) will be observed across more pixels compared to a slower particle (i.e. STV/BTN*/complex). Spatio-temporal correlation of fluorescence intensity fluctuations is calculated from the image and occurs in a scale that depends on the rate of diffusion. (c) top: simulated function for molecules with high diffusion coefficient (high D); down: simulated function for molecules with low diffusion coefficient (low D). RICS reveals the mobility of molecules and thus molecular events within sub-regions of the image in the micro-millisecond timescale.

4.2 Water-in-oil Droplet Array Assembly

It is well known that assembling droplets arrays by inkjet printing is possible only under specific regimes of fluid properties[9]. If from one hand, assembly of mineral oil droplets is easily accomplished, on the other hand, inkjet printing picoliter-scale aqueous droplets constitutes a challenge (**Fig. 4.6-4.8**). Indeed, printing aqueous droplets gives rise to small satellites around the main droplet due to multiple breakups during ejection[10]. Proper tuning of the droplet speed and of the waveform are needed to obtain droplets of optimal shape without satellites embedded in the oil phase.

The experimental conditions for inkjet printing operation can be better visualized in **figure 4.6** in which the inverse of Ohnesorge number (Z = 1/Oh) is plotted against the Reynold number according to Derby[9]. Ohnesorge (Oh) and Reynold (Re) numbers are given by:

$$Oh = \frac{\mu}{\sqrt{\rho\sigma L}} \quad Re = \frac{\rho v L}{\mu}$$

Where ρ is the liquid density (g/cm^3), σ is the surface tension (dyne/cm), L is the characteristic length scale (i.e drop diameter), v is the velocity of the fluid (m/s) and μ is the dynamic viscosity of the fluid (cP).

Whereas Oh relates the viscous forces to surface tension forces, Re relates the inertial forces to the viscous forces.

The red dot in the **figure 4.6** defines the experimental conditions of the liquid ink here used (100 mM potassium phosphate, 0.05% tween 20). The low viscosity of the aqueous ink determines satellites which would render the printing process not reproducible. On the other hand, the grey dot corresponds to the experimental condition of the mineral oil, which has high viscosity and low density, respectively 30.0 cP and 0.82 g/cm^3.

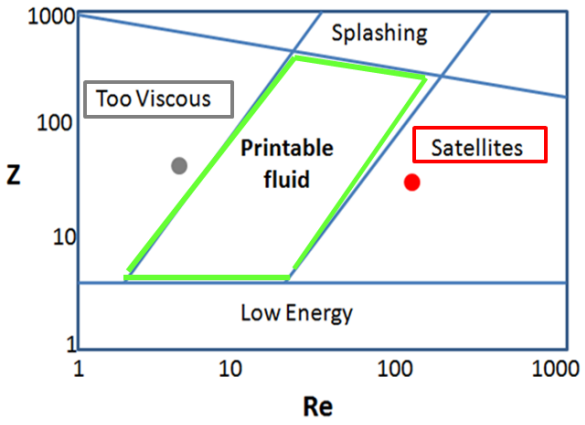

Figure 4.6: Printing regimes in inkjet printing. The coordinate system defined by the Reynolds and Z (i.e. the inverse of Ohnesorge number) illustrate the regime of fluid properties in which inkjet

printing is possible. Red and grey dot represent experimental points for, respectively, aqueous ink and mineral oil.

Inkjet printing dispensing of mineral oil was easily accomplished by standard double pulse waveforms (**Fig. 4.7**), increasing ink temperature at 33 °C in order to reduce dynamic viscosity (30 cps at 25 °C) obtaining droplets with long tails (> 200 µm) having velocities in the range 5 to 15 m/s (**Fig. 4.8**). The assembly of mineral oil droplets arrays on glass surfaces is easily accomplished by employing conventional piezoelectric waveforms (**Fig. 4.7**). In the initial stage piezo is in a neutral or relaxed position in which chamber is at its maximum volume. During the rise time (t_R) voltage is increased, causing a deflection in the piezo which pulls the fluid to the nozzle exit in order to form the droplet. The time at which the piezo is stable in a deflected state is called dwell time t_D. During fall time (t_F), the piezo voltage is decreased in order to pinch-off droplet at the nozzle exit. Remarkably, the relative relaxation of the piezo in during t_F permits to pull the liquid thread back in the nozzle.

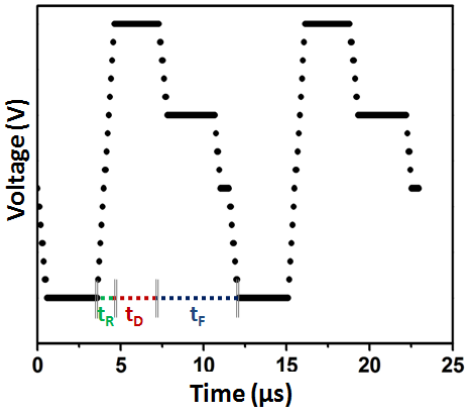

Fig. 4.7: Conventional double pulse waveform.

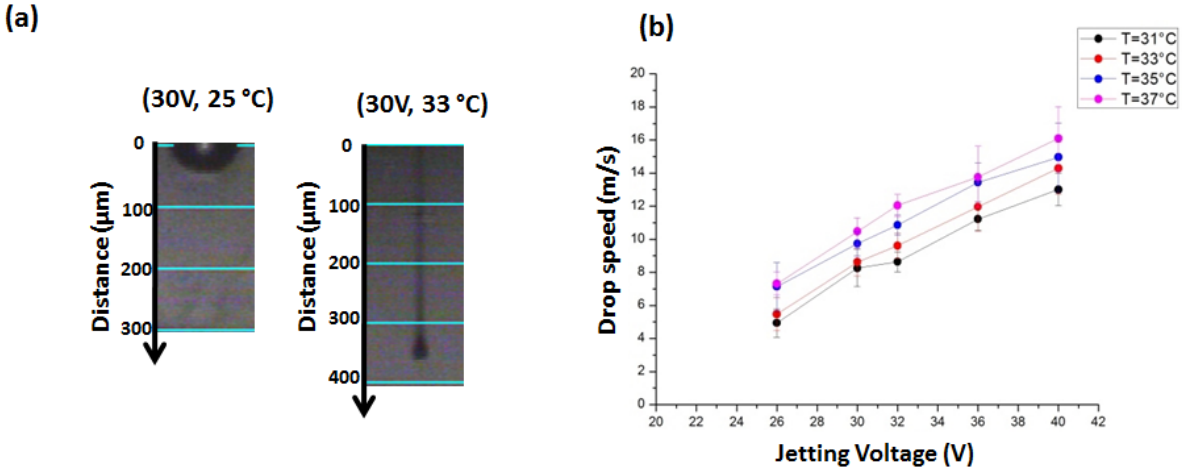

Fig. 4.8: Mineral oil droplet dispensing. (a). Stroboscopic images of 10 pL (nominal volume) mineral oil droplet pinching-off at nozzle at 25 °C (left) and at 33 °C (right). (b) Droplet speed (m/s) versus Jetting Voltage (V) for mineral oil droplet dispensing by double pulse waveforms at increasing temperature (31 °C – 37 °C).

Aqueous ink dispensing required a more careful investigation. In order to allow the printing process of such low viscosity ink, we optimized the waveform signal in order to avoid satellites formation. The liquid thread ejected from the nozzle is able to contract into a single drop without breaking up if the length of liquid thread at pinch-off, l_b, does not exceed a limiting value l_b* as from the following equation[11,12]:

$$\frac{l_b}{R_{noz}} < \zeta \frac{1}{\alpha^*_{max}} + 2 = \frac{l^*_b}{R_{noz}}$$

Where R_{noz} is the radius of the nozzle; $\zeta = (C_2\text{-}C_1)\cdot a$ is a measure of the times difference for the formation of the droplets at the nozzle exit C_1 and at complete pinch-off C_2, being a constant value. ζ is usually comprised between 0.9 and 1.1; $\alpha_{max}{}^*$ is given by the following expression:

$$\alpha^*_{max} = \sqrt{\frac{1}{2}x^2(1-x^2) + \frac{9}{4}x^4} - \frac{3}{2}Oh \cdot x^2$$

where

$$x^2 = \frac{1}{2 + \sqrt{18} \cdot Oh}$$

From this model, it turns out that for our aqueous ink, by considering that tween-20 decreases surface tension up to 35 mN/m, we obtain that Oh is almost 0.036 and α^*_{max} is equal to 0.756 which determine a $\frac{l^*_b}{R_{noz}}$ ratio of about 3.5. This means that in order to avoid satellite formation, it is necessary to have a liquid length while pinching off at nozzle of not more than 60 µm, since radius of the nozzle is about 21 µm.

Double pulse waveform used for aqueous ink dispensing produced long liquid thread (> 60 µm), so determining, as expected, a high number of satellites droplets (**Fig. 4.9-4.10**).

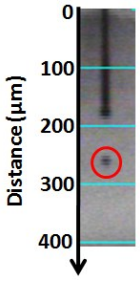

Fig. 4.9: Stroboscopic image of 10 pL (nominal volume) Alexa 647 droplet (40 nM, 0.05% Tween-20) pinching-off at nozzle during emission (16 V) by double pulse waveform. Satellite droplet is marked in the red circle.

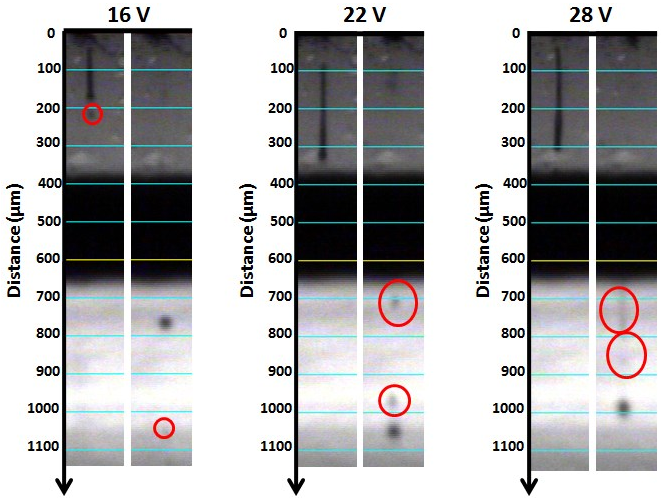

Fig. 4.10: Stroboscopic images of Atto-655 biotin (BTN*) (40 nM, 0.05 % tween 20) droplet dispensing by double pulse waveforms at various voltages (16 V – 22 V – 28 V). At each voltage, stroboscopic picture is taken while droplet is pinched-off (left figure) and when it reached 1000 µm to better show multiple breakups. Satellites droplets are encircled.

In order to avoid satellites formation during aqueous ink dispensing, we needed to tune waveform signal for reducing liquid length while pinching off at nozzle at values minor than 60 µm. To achieve that, we adapted a single pulse waveform signal (**Fig. 4.11**) instead of the conventional double pulse waveform (**Fig. 4.7**) in such a way to:

1. Increase the rise time (t_R) (which passed from 1 µs of double pulse waveform to 2.93 µs of single pulse waveform) in order to favour droplet formation at the nozzle.
2. Increase the fall time (t_F), i.e. the time at which the piezo voltage is decreased in order to pinch-off droplet at the nozzle exit. As to do so, we showed the possibility to decrease the onset of multiple breakup phenomena in the liquid thread minimizing the occurrence of satellite droplets[13]. We fixed fall time (t_F) to 16.9 µs – to be compared with 4.92 µs of double pulse waveform.

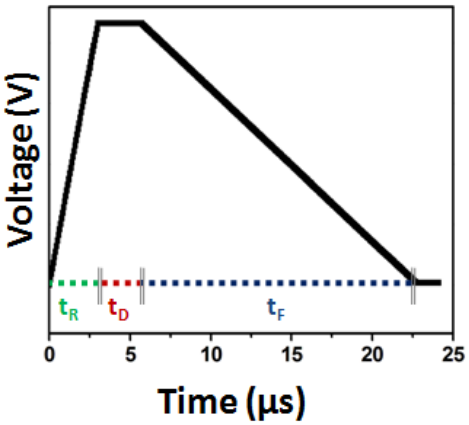

Fig. 4.11: Single pulse waveform specifically suited for aqueous inkjet printing.

We then investigated the liquid thread length while pinching-off at nozzle as a function of jetting voltages by using single pulse waveform signal pulse (**Fig. 4.12**). As clearly shown by stroboscopic figures (**Fig. 4.12a**), low-to-intermediate jetting voltages (16 V - 22 V) allow for short liquid threads (minor than threshold of 60 µm) that rapidly coalesce into spherical droplets, whereas high voltages (28 V) determine liquid threads longer than threshold which are prone to breakups and satellite formation. For this reason, we identified low voltages as the optimal condition for aqueous ink dispensing at velocities (around 6 m/s – see **Fig. 4.12b**) sufficient for encapsulation into mineral oil droplets. Remarkably, droplet velocities are quite well distributed among different nozzles of the same print head (**Fig. 4.12c**).

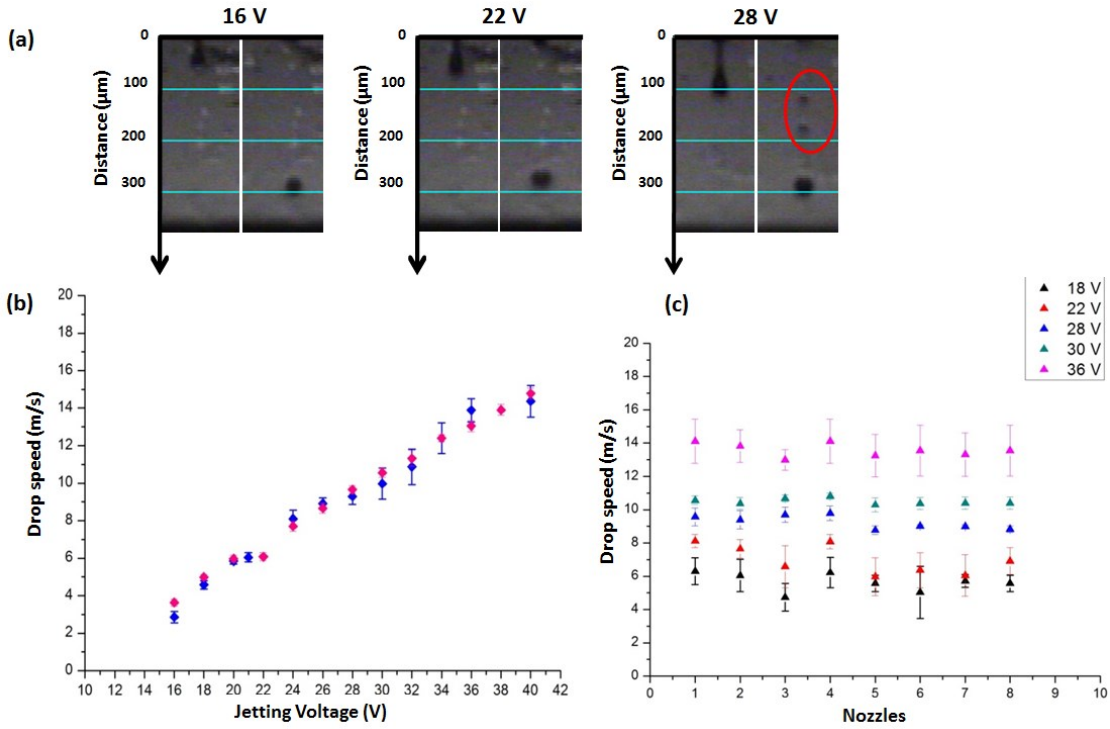

Fig. 4.12: Atto-655 biotin droplet dispensing by single pulse waveforms. (a) Stroboscopic images of 10 pL (nominal volume) BTN* (40 nM, 0.05 % tween 20) droplet pinching-off at nozzle at 16 V, 22 V and 28 V (left picture for each voltage), or when it reached almost 300 µm in the trajectory from nozzle. Satellites droplets are encircled. (b) Droplet speed (m/s) versus Jetting Voltage (V) for BTN* (40 nM) droplet in absence of STV (blu dots) or in presence of Streptavidin 10 nM (red dots). (c) Droplet velocity as a function of jetting nozzle for BTN* (40 nM) solution dispensing.

4.3 Molecular Diffusion Investigation by CADRICS

4.3.1 Molecular diffusion of Alexa 647 in nL environment

We initially optimized the inkjet dispensing by printing aqueous droplets containing the model fluorophore Alexa 647 (30 nM in 50 mM phosphate buffer pH 7.4) in order to optimize the following properties: i) shape, ii) stability against leakage, iii) solute concentration and iv)

occurrence of free diffusion. In **figure 4.13a** the shape of the single pulse waveform is reported together with the stroboscopic image of a 10 pL (nominal volume) Alexa 647 droplet pinching-off from the nozzle (30 nM, phosphate buffer with 0.05% of the non-ionic surfactant tween-20). The measured droplet speed is reported in **figure 4.13b** as a function of the jetting voltage for a single pulse waveform in the presence and in the absence of tween-20. For jetting voltages of about 20 V the droplet is stable and does not give satellites. In contrast, the conventional double pulse waveform used for viscous fluids gives rise to satellite droplets on such aqueous inks. This is in agreement with previous findings in which to obtain stable drops by double pulse waveform we needed to spike protein inks with high viscous additives like glycerol[14]. Remarkably, by using this waveform at low jetting voltages (14-20 V), we obtained almost spherical droplets with a very short tail (**Fig. 4.13a**). Remarkably, for jetting voltages of 14-20 V, the water droplet speed was in the 4-6 m/s range (**Fig. 4.13b**) that allows for the reproducible and successful insertion in the oil droplet (this occurs at velocities higher than 1-2 m/s) [15]. The water/oil interface was stabilized by spiking Alexa 647 aqueous droplets with the non-ionic surfactant tween-20 (0.05 % v/v). Representative fluorescence images of droplets obtained in presence and in absence of tween-20 are reported in **Fig. 4.13c**.

Accordingly, in the absence of tween-20 the diameter of the droplet is smaller than that of the one containing the surfactant and the leakage of the fluorophore into oil occurs in few minutes. In order to realize an array of aqueous droplets in oil, about one hundred 10 pL droplets (about 1 nL, 30 nM Alexa 647, 50 mM phosphate buffer, pH 7.4, 0.05 % tween-20) were injected into a mineral oil droplet of 10 nL (previously formed by one thousand 10 pL droplets). Importantly, the production of an array is pretty fast. About 20 water-in-oil drops can be printed in few minutes. Also, in the selected conditions, evaporation did not occur since the nozzle-to-oil trajectory takes hundreds of microseconds, that is significantly shorter than the picoliter droplet evaporation time (hundreds of milliseconds)[16]. **Fig. 4.13d** reports the investigation of the Alexa 647 diffusion by RICS into an individual confined droplet. Briefly the analysis of the spatial correlation function using a free diffusion model gives the molecular diffusion coefficient (D) and the amplitude G(0) that is proportional to the inverse of the average number of fluorescent particles in the measurement volume. Importantly RICS allows acquiring measurements in a uniform region of the droplet volume. The obtained D = 270 $\mu m^2/s$ and G(0) = 0.014 ± 0.003 for Alexa 647 dye are perfectly consistent with analogous measurements on larger volume droplets (50 µL - 100 nL droplets volumes, **Fig. 4.14**). This demonstrates that the printing process does affect neither the aqueous compartment properties nor the fluorescent dye concentration.

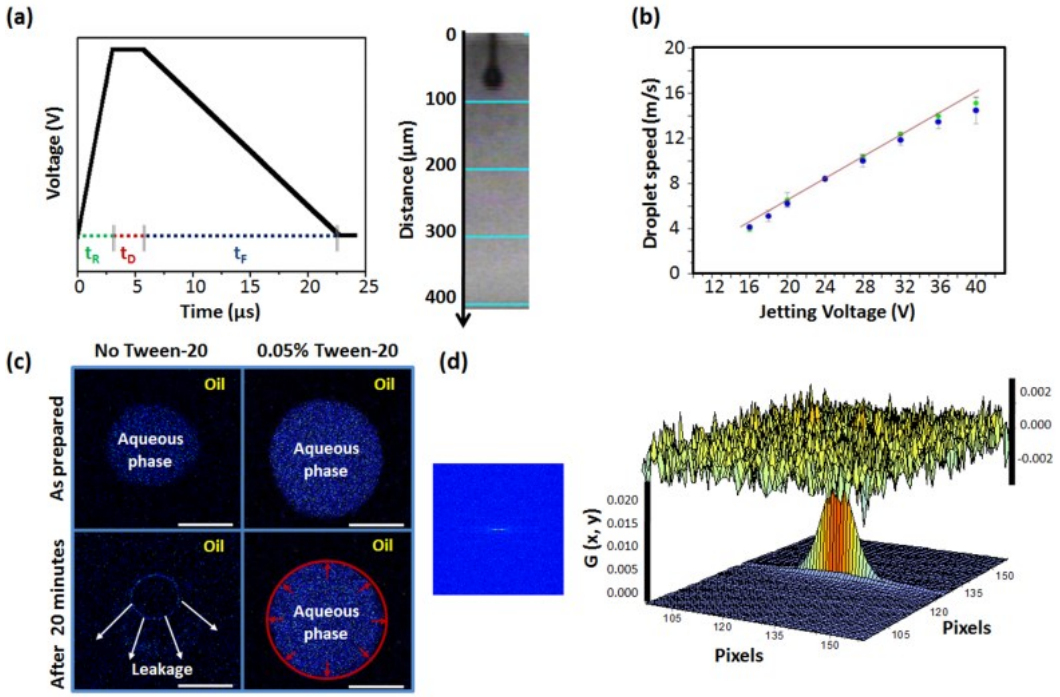

Figure 4.13: Assembly of confined aqueous compartments and subsequent RICS. (a) Piezoelectric single pulse driving waveform for aqueous picoliter droplet ejection. The time intervals t_R, t_D and t_F represent the times of rise, dwell and fall, respectively. Insets show representative stroboscopic image of 10 pL (nominal volume) Alexa 647 droplet (30 nM, 0.05% tween-20) pinching-off at the nozzle. (b) Droplet speed (Alexa 647 30 nM) as a function of jetting voltage for a single pulse waveform in absence (blue dots) or in presence (green dots) of (b) Representative images of Alexa 647 droplets injected in oil in absence or in presence of tween-20 0.05%. The fluorophore leakage in oil phase is observed when tween-20 is not present. Scale bar is 100 µm. (d) Spatial correlation function obtained from measurements on stable droplets of Alexa 647-in-oil arrays for a droplet of 1 nL. RICS shape clearly indicates the fast free diffusion of a small molecule and the fit gives D = 270 $\mu m^2/s$ and G (0) = 0.014 ± 0.003.

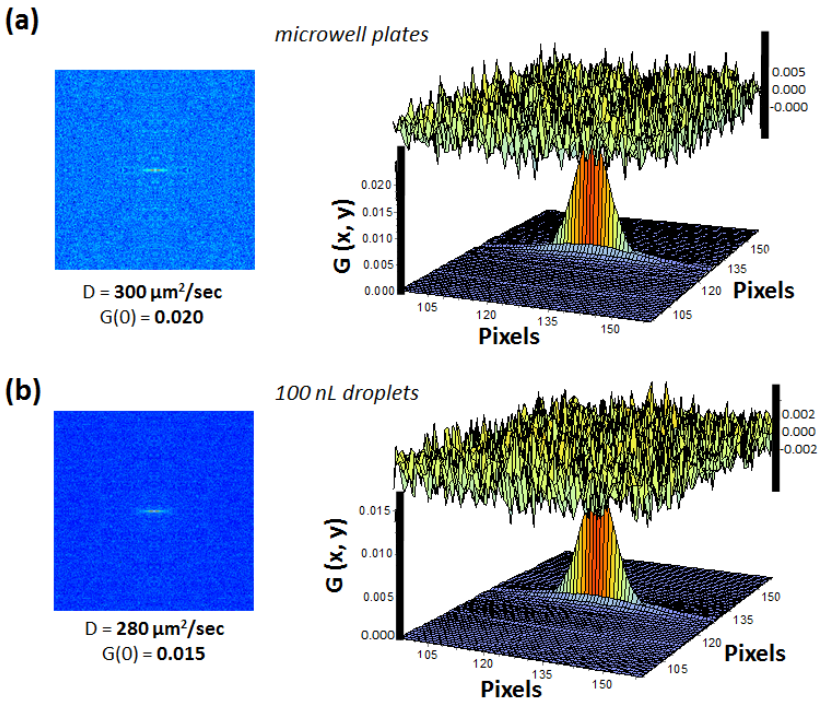

Figure 4.14: RICS on Alexa 647 solution on 50 µL volume in microwell plates and on 100 nL droplets manually deposed. Spatial autocorrelation functions and relative fits with residuals of of Alexa 647 (20 nM) in microwell plates (a) and on 100 nL droplets (b).

4.3.2 Molecular binding assays in confined compartments

Having demonstrated the possibility to fabricate confined aqueous compartments in which one can investigate molecular diffusion of a model fluorophore (Alexa 647), we show CADRICS capability to produce arrays of BTN* and STV solution as well as arrays of their mixtures at nM concentrations, i.e. suitable concentrations for monitoring few molecular binding events in small volume confined compartments. The choice of this system, consisting of labelled biotin (BTN*) and unlabelled streptavidin (STV), allows one for clearly distinguishing the formation of the complex STV-BTN* from free BTN*. In fact, once BTN* (MW = 1.2 kD) is bound to STV (MW = 60 kD) its diffusion coefficient is expected to be significantly reduced (**Fig. 4.15**).

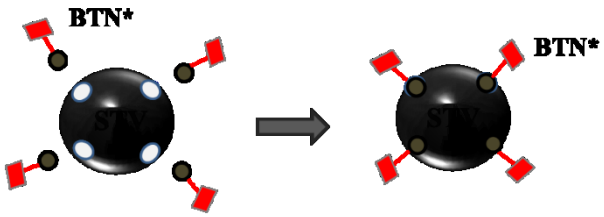

Figure 4.15: Atto655-biotin (BTN*) and Streptavidin (STV) interaction. Streptavidin has four binding sites for biotin (Kd approx. 10^{-15} M).

In particular, we encapsulated aqueous droplets (50 mM phosphate buffer, pH 7.4, 0.05% Tween-20) containing 20 nM BTN* or the mixture 20 nM BTN* - 200 nM STV into mineral oil droplets.

In addition to the stabilization of the water-oil interface, tween-20 also permitted to avoid colloidal aggregates formation in solution[17]. In order to get statistically significant data, the molecular binding events investigation has been carried out on tens of 1 nL droplets. Then, the suitability of CADRICS was tested on a range of different volumes (from 50 uL to 100 pL). Typical results are shown in **Fig. 4.16**. RICS functions of BTN* (**Fig. 4.16a**) and STV-BTN* (**Fig. 4.16b**) systems in 1 nL droplets are shown revealing that also in this case the molecules are freely diffusing within the droplet. It is immediately evident that the spatial correlation function for STV-BTN* droplets stands for slower diffusion. Measurements on STV-BTN* complex reported in figure are obtained with an excess of STV (200 nM) with respect to the ligand, i.e. a condition where all BTN* molecules are expected to be bound to STV. Several measurements were performed on multiple droplets and diffusion coefficients obtained from multiple 1 nL droplets are reported in **Fig. 4.16c**. Results indicate that the diffusion coefficients measured in BTN* and STV-BTN* droplets are clearly distinguishable within the experimental error (larger distribution of D for faster molecules is due to the instrumental sensitivity). The measured value of D for STV-BTN* droplets (about 60 $\mu m^2/s$) can be explained by the formation of the complex. In **figure 4.16d**, the diffusion coefficients measured for analogous solution in droplets of a range of volumes are reported (50 µL - 100 pL). The D values are comparable for all the investigated volume ranges, this clearly demonstrates the occurrence of free molecular diffusion up to picoliter volume scale – i.e. confinement in inkjetted droplets (1 – 0.1 nL) does not modify the molecular diffusion coefficient and protein binding in comparison to macroscopic volumes (50 µL – 100 nL). Droplet volumes are orders of magnitude above those of a single cell (picoliter scale) or a sub-cellular organelles (sub--picoliter scale) in which anomalous diffusion typically takes place[18] – mainly due to molecular crowding effects which generate heterogeneous intermolecular environements[19].

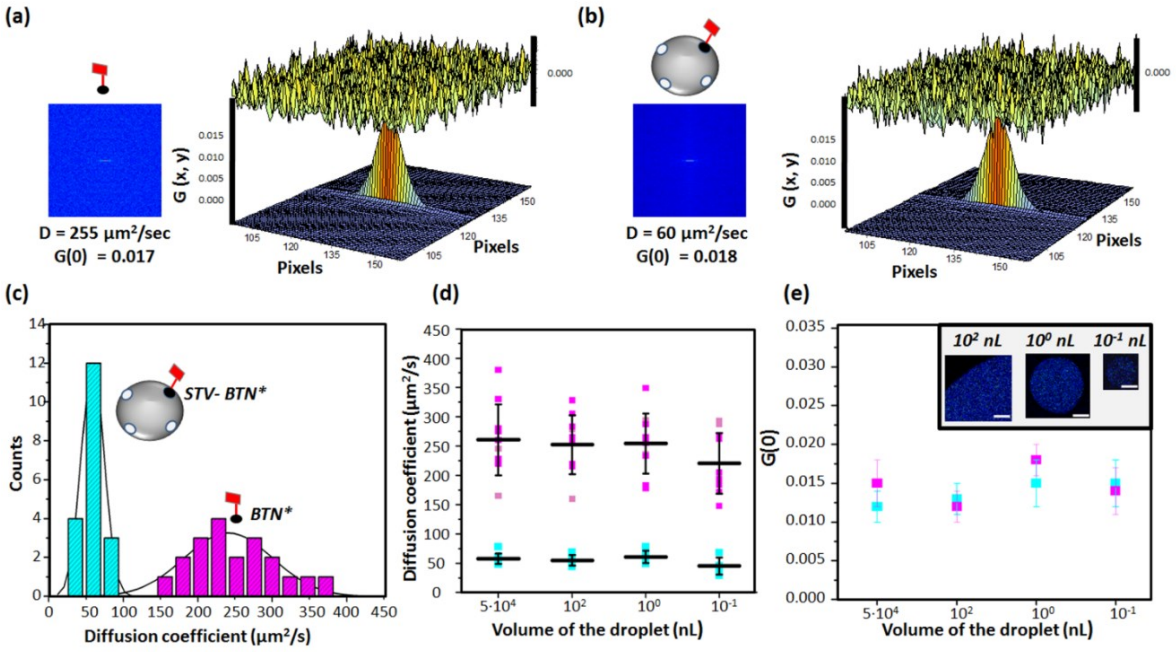

Figure 4.16: CADRICS for binding assays in confined aqueous compartments. Spatial autocorrelation functions and relative fits with residuals obtained for: (a) BTN* (20 nM); (b) STV-BTN* in 1 nL aqueous droplet. (c) Distribution of the diffusion coefficient obtained by RICS analysis of measurements on multiple 1 nL droplets in printed arrays for BTN* (pink) and STV-BTN* (cyan) systems. (d) Diffusion coefficient obtained by RICS analysis of measurements on multiple droplets at different volumes for BTN* (pink) and STV-BTN* (cyan). (e) G(0) values for droplets containing BTN* (magenta) and STV-BTN* (cyan). The inset reports representative 256x256 confocal microscopy images of BTN* containing droplets having different volumes. Scale bar is 50 µm.

Importantly, aqueous solutions can be efficiently printed, without affecting the value of solute concentration as shown by the G(0) values reported in **figure 4.16e**.

In **figures 4.17** and **4.18** are reported RICS analysis results for measurements on larger volume droplets 50 µL ad 100 nL, respectively.

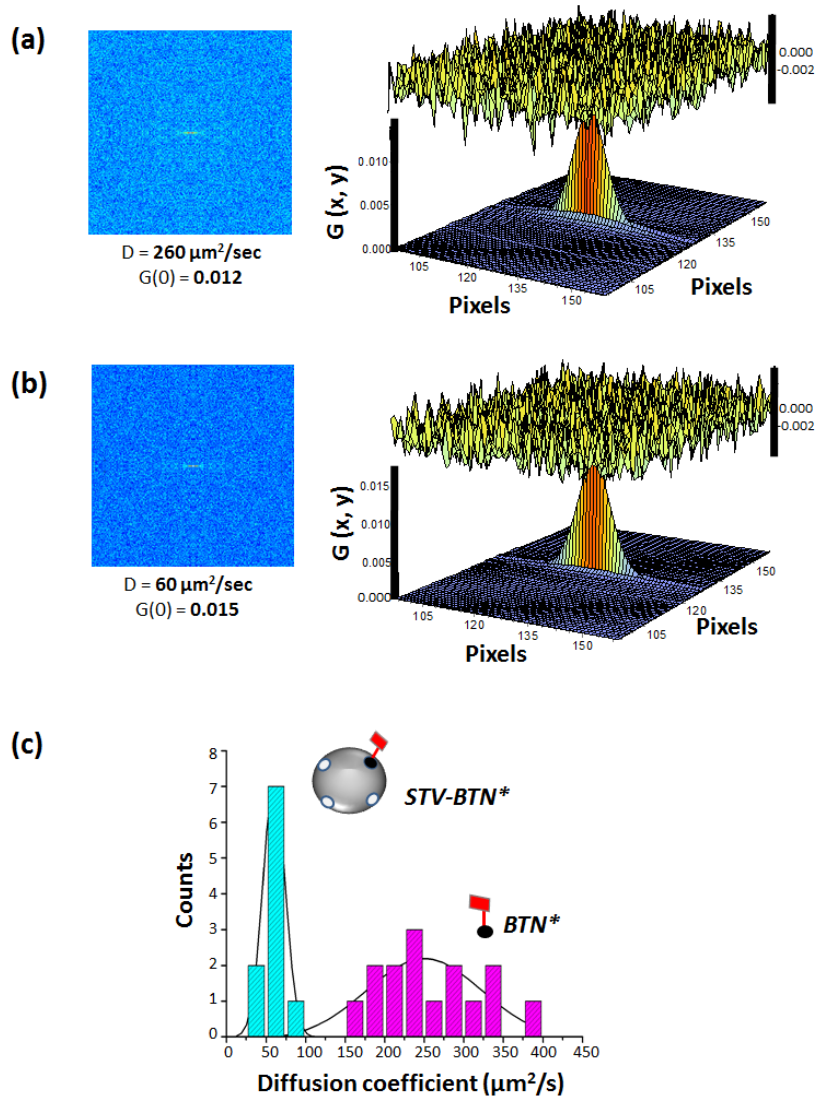

Figure 4.17: BTN* binding to STV obtained from measurements on 50 µL volume samples in microwell plates. Typical spatial autocorrelation functions and relative fits with residuals of Atto655-biotin (BTN*) (20 nM) (a) and of the Streptavidin-Atto655-biotin (STV-BTN*) complex (b) obtained from microwell plates. In (c), histograms showing diffusion coefficient distribution for BTN* (light blue bars) and STV-BTN* complex (pink bars) obtained from measurements in microwell plates. Black lines representing Gaussian distributions centered at D mean values are reported as an eye guidelines.

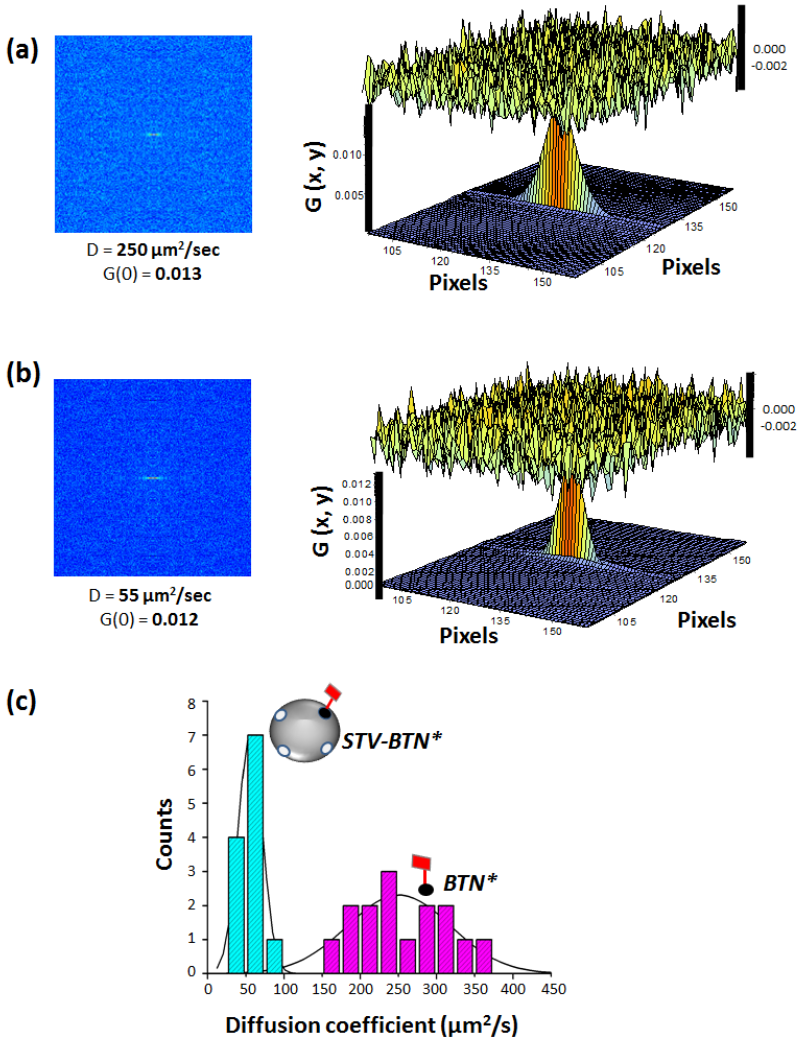

Figure 4.18: BTN* binding to STV in 100 nL droplets. Spatial autocorrelation functions and relative fits with residuals of BTN* (20 nM) (a) and of the STV-BTN* complex (b) obtained from 100 nL aqueous droplets. In (c), histograms showing diffusion coefficients distribution for BTN* (light blue bars) and STV-BTN* complex (pink bars) obtained from measurements in 100 nL aqueous droplets. Black lines representing Gaussian distributions centered at D mean values are reported as an eye guidelines.

Data reported in **figure 4.16** together with results in **Table 4.1** point out that the molecular concentration is not modified by printing. Note that the G(0) values for STV-BTN* and BTN* droplets are equivalent on all the volume range, that is consistent with the presence only of bound BTN* as expected in large excess of STV.

Volume (nL)	D (BTN*) (µm²/s)	G(0)	D (STV-BTN*) (µm²/s)	G(0)
$5 \cdot 10^4$	260.7 ± 60.6	0.015 ± 0.003	57.9 ± 8.9	0.012 ± 0.002
10^2	252.4 ± 50.1	0.012 ± 0.002	54.8 ±9 .1	0.013 ± 0.002
10^0	254.4 ± 51.1	0.018 ± 0.002	60.7 ± 10.5	0.015 ± 0.003

10^{-1}	220.4 ± 51.8	0.014 ± 0.003	45.2 ± 14.6	0.015 ± 0.003

Table 4.1: Comparison of average diffusion coefficients (D) and G_0 values obtained from ten measurements on samples of different volumes ($5 \cdot 10^4 – 10^0$ nL).

Typically, concentration range employed in RICS are comprised between 10-100 nM in order to obtain reliable image correlation functions, as reported by Brown et al.[8]. The possibility to employ nanomolar-scale concentrations for binding assays in liquid phase droplets is a clear advantage of our CADRICS method in comparison with established approaches, since binding assays are conducted at pico-to nano-liter scale, with molecular consumptions as low as 1-10 attomoles scale per single droplet permitting to extract molecular diffusion parameters and binding dynamics information comparable to macrovolumes (microliter scale).

Notably, whereas 1 nL droplets were totally stable against leakage for several hours, aqueous droplet stability was affected at 100 pL volume range, likely due to the high surface/volume ratio[20]. Many previous reports state that the mechanical stresses occurring during the printing process can affect the protein structure and hence its activity due to the compression and shear stresses by the droplet ejection[21,14]. Remarkably, we here found that inkjet printing processes in aqueous based inks does not affect the STV binding activity towards BTN* without employing any additives (i.e. glycerol or PEG). Moreover, the fact that solution concentrations are not affected by the printing process indicates that inkjet printing of STV aqueous solutions does not lead to significant protein adsorption on print-head surfaces, as it would be expected in the case of dilute protein inks[22] due to the coupling of adsorption kinetics with convection-diffusion phenomena in the microchannels[23]. This fact is likely due to the fact that tween-20 is able to prevent colloidal aggregation of biomolecules[17,5], thus avoiding protein adsorption on surfaces[24]. Thus, given the mild printing conditions of our nanomolar concentrated aqueous based ink spiked with 0.05 % tween-20, the excellent stability in mineral oil against leakage, and the optimal correspondence of D and G(0) values between macroscopic and microscopic volumes, we selected 1 nL droplet volume as the optimal condition for further application of our CADRICS methodology in investigating protein-ligand interactions.

4.3.3 Biochemical assays in confined compartments

To demonstrate that CADRICS is useful for programming confined droplet arrays suitable for biochemical assays, displacement tests assessing biomolecular interactions on droplets containing mixtures of BTN*, BTN and STV at nanomolar concentrations were carried out. Accordingly, we varied the [BTN]/[BTN*] ratio in order to test the competition between BTN and BTN* towards binding to STV in 1 nL confined droplets. We firstly investigated BTN* interaction with STV in a

stoichiometric ratio of 4:1 (40 nM BTN*, 10 nM STV) and then, we added BTN at the concentration range of 40-320 nM to compete with BTN* binding to STV.

In **figure 4.19** RICS results for BTN*-STV system in the stoichiometric ratio 4:1.

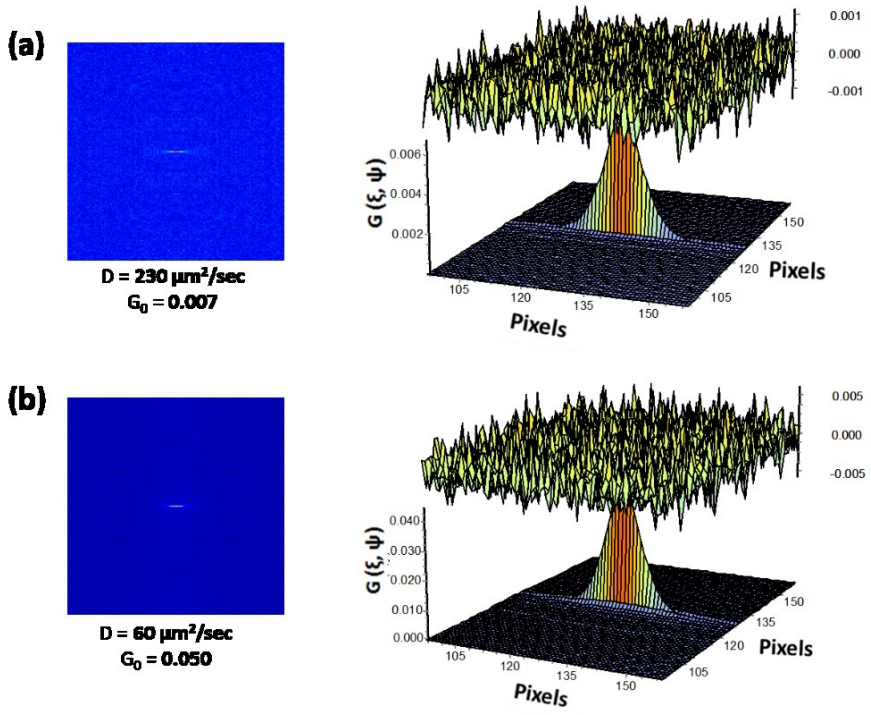

Figure 4.19: Spatial autocorrelation functions and relative fits with residuals of BTN* (40 nM) **(a)** and of the STV-BTN* complex in presence of the stoichiometric amount of STV (10 nM) **(b)** obtained from measurements 1 nL droplets.

In **figure 4.20a** we report representative 256x256 fluorescence confocal microscopy images of the droplets as function of the [BTN]/[BTN*] ratio. As it can be seen the measured fluorescence intensity increases with the [BTN]/[BTN*] ratio. Atto 655 fluorescence quantum yield decreases as BTN* binds STV, this effect being explained by Buschmann et al.[24] as due to the interaction of Atto 655 with tryptophan residues in the STV binding site. The average measured fluorescence intensity is reported in **figure 4.20b** as a function of the [BTN]/[BTN*] ratio. Fluorescence intensity reaches a plateau values at concentrations in which BTN is in large excess with respect to BTN* so that, assuming that BTN and BTN* have the same affinity towards STV[25], at high [BTN] essentially all BTN* are freely diffusing in the confined droplet. In **figure 4.20c**, the D values calculated from one component RICS analysis is reported for droplets at increasing BTN concentration. The observed increase of average D value qualitatively demonstrates the presence of free BTN* molecules in droplet due to the BTN competitive binding to STV. Since STV has four binding sites for BTN* or BTN, quantitative investigation in this system is quite challenging given that the binding interaction of BTN* to STV in presence of BTN, is expected to form STV-BTN_4, STV-BTN_1(BTN_3*), STV-BTN_2(BTN_2*), STV-BTN_3(BTN_1*) and STV-(BTN_4*) species, all having approximately the same D but different brightness due to the different number of BTN*

molecules bound to STV. Also, one has to consider that BTN* fluorescence is partially quenched when bound to STV[26]. However, it is still possible to carry out a semi-quantitative evaluation of BTN vs. BTN* competition towards binding to STV.

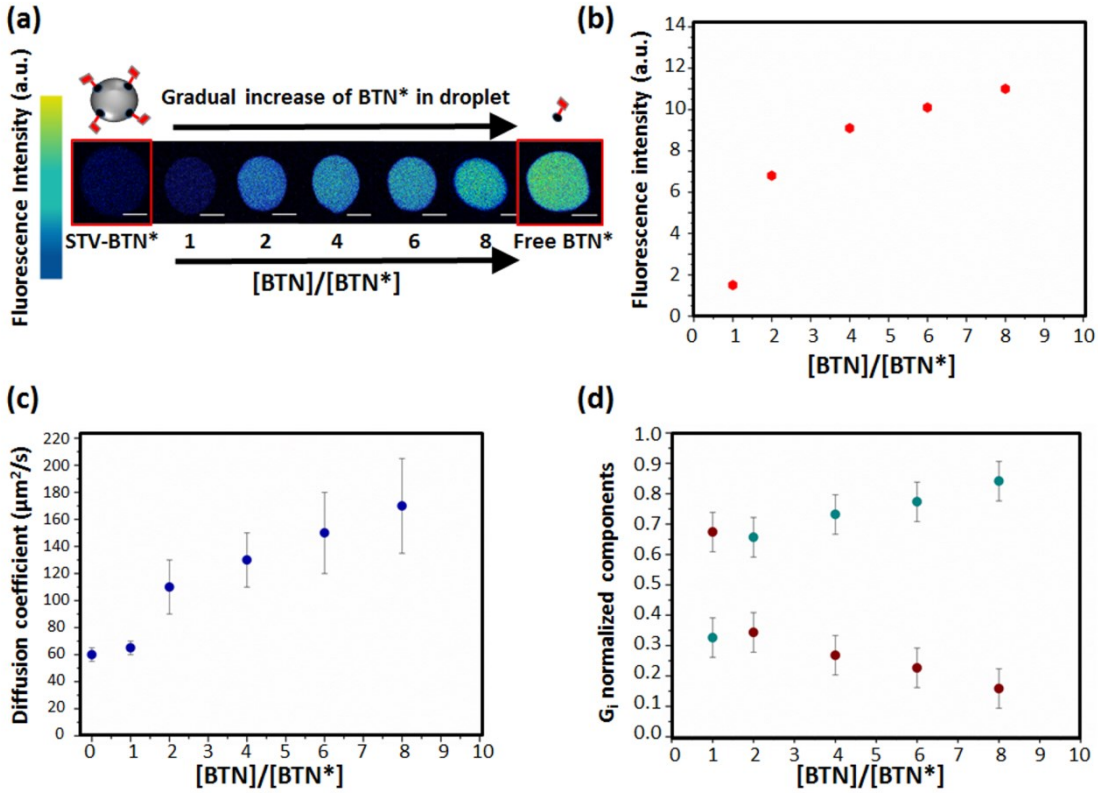

Figure 4.20: Competitive inhibition in 1 nL confined aqueous compartments. (a) 256x256 representative fluorescence confocal images of 1 nL droplets. All aqueous droplets contain 40 nM BTN* - 10 nM STV. [BTN]/[BTN*] ratio is progressively increased in the droplet corresponding to [BTN] values of 40 nM, 80 nM, 160 nM, 240 nM and 320 nM. The droplet on the right contains free BTN* as reference. Scale bar is equal to 100 µm. (b) Average fluorescence intensity measured in the droplets. (c) Diffusion coefficient obtained from one component RICS analysis as a function of molar fraction between BTN and BTN*. (d) Normalised amplitude $G_1(0)/G(0)$ (red dots) and $G_2(0)/G(0)$ (blue dots).

In fact, from RICS it is also possible to carry out multicomponent analysis as described by Ilaste et al.[27] who derived an analytical expression for autocorrelation function in case of two diffusing species with different diffusion coefficients. From their expression, it is possible to obtain:

$$G(0) = \frac{\gamma}{(\bar{n}_1 + \bar{n}_2)^2} \cdot (\bar{n}_1 + \bar{n}_2)$$

In which $\bar{n}_1$ and $\bar{n}_2$ are the concentrations of the species having molecular diffusion D_1 and D_2. By defining $G(0) = \frac{\gamma}{\bar{n}_1 + \bar{n}_2}$ and the molar fraction $\chi_i = \frac{\bar{n}_i}{\bar{n}_1 + \bar{n}_2}$, it is possible to obtain:

$$G(0) = G(0)\frac{\bar{n}_1}{\bar{n}_1 + \bar{n}_2} + G(0)\frac{\bar{n}_2}{\bar{n}_1 + \bar{n}_2}$$

Which finally gives:

$$G(0) = G(0) \cdot \chi_1 + G(0) \cdot \chi_2$$

This can be rewritten as:

$$G(0) = G(0)_1 + G(0)_2$$

In which we define $G_1 = G(0) \cdot \chi_1$ as the $G(0)$ value for the slow diffusing species and $G_2 = G(0) \cdot \chi_2$ as the $G(0)$ value for the rapid diffusing species.

So, it was possible to fit RICS autocorrelation function using two components, the slow component relative to bound BTN* species - see above - (fixed at D = 50 $\mu m^2/s$) and the fast component due to freely diffusing BTN* (fixed at D = 200 $\mu m^2/s$) in order to qualitatively evaluate the relative amounts of bound and free BTN* in the aqueous droplets. In **figure 4.20d** we report the normalised amplitude of the autocorrelation function $G_2(0)/G(0)$ and $G_1(0)/G(0)$ [27], being $G(0) = G_1(0) + G_2(0)$. Note that $G_1(0)$ represents the amplitude of slow diffusion component and $G_2(0)$ is the amplitude of fast diffusion component. As expected, the ratio $G_1(0)/G(0)$ decreases with the molar fraction between BTN and BTN*, given the competition of BTN towards BTN* on binding with STV.

Similar results were observed in macroscopic volumes (**Fig. 4.21 and 4.22**).

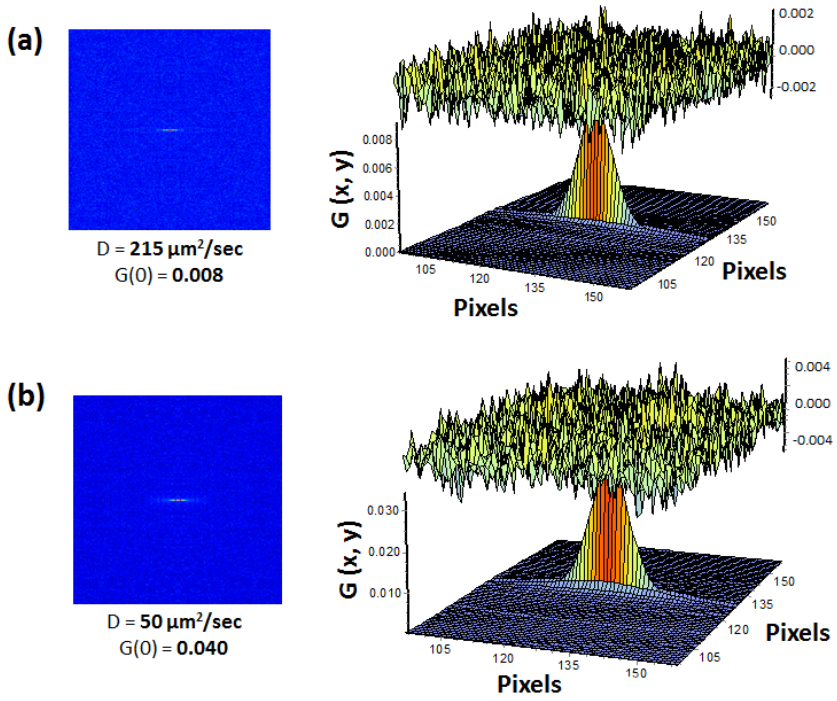

Figure 4.21: Spatial autocorrelation functions and relative fits with residuals of of BTN* (40 nM) (a) and of the STV-BTN* complex in presence of the stoichiometric amount of STV (10 nM) (b) obtained from measurements on 100 nL droplets.

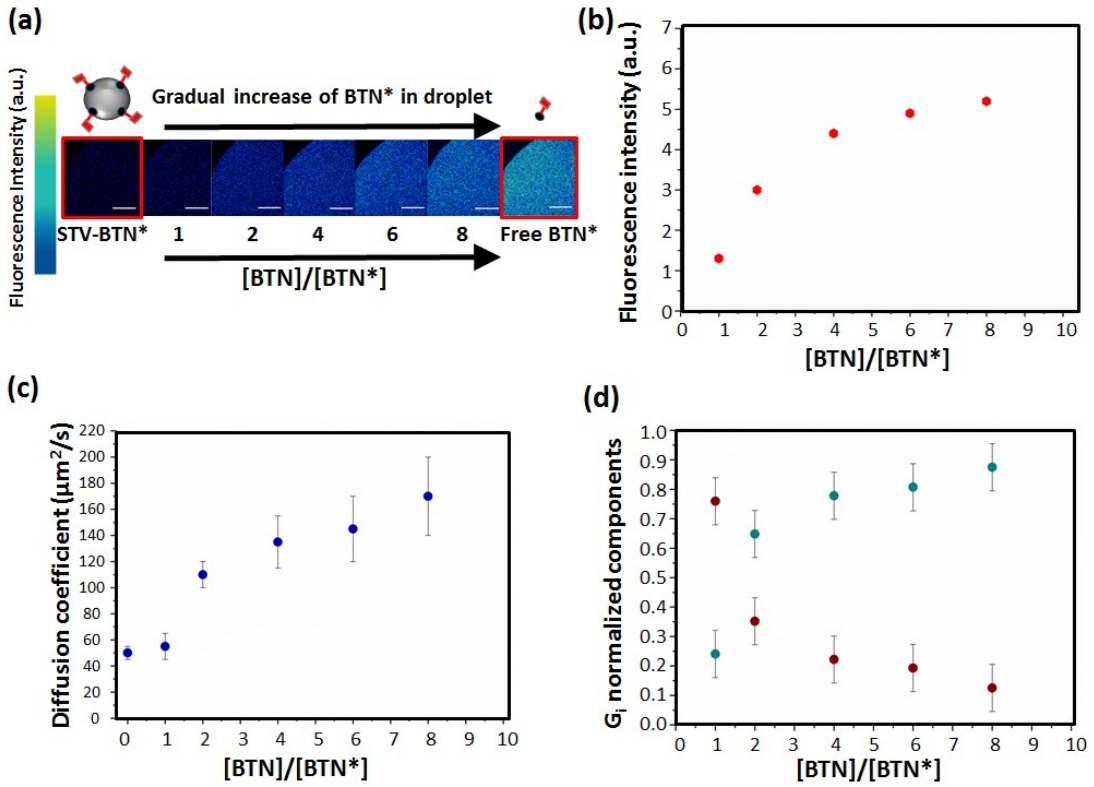

Figure 4.22: Competitive inhibition reactions in 100 nL droplets. (a) 256x256 representative fluorescence confocal images of 100 nL drops injected in oil matrices. All aqueous droplets contain 40 nM BTN* -10 nM STV. [BTN]/[BTN*] ratio is progressively increased in the droplet - corresponding to [BTN] values of 40 nM, 80 nM, 160 nM, 240 nM and 320 nM. Drop on the right contains free BTN* as reference. Scale bar is equal to 100 µm. (b) Average fluorescence intensity measured in the droplets. (c) Diffusion coefficients obtained from one component RICS analysis as a function of molar fraction between BTN and BTN*. (d) Normalised amplitude $G_1(0)/G(0)$ (red dots) and $G_2(0)/G(0)$ (blue dots).

CADRICS combines, for the first time, confined aqueous droplet dispensing by inkjet printing (in absence of viscous or humectants additives) with detection by RICS. Accordingly, in contrast to existing technological platforms, we demonstrate significant improvements in turns of mildness of fabrication (i.e. no need for external or pyroeletrohydrodynamic[28] or electrohydrodynamic[29] jets), sensitivity (up to few molecules), low consumption of reagents (nanoliter droplets with nanomolar concentrations of biomolecules) and precise mimicking of biological native condition in droplets. We achieve this result by coupling the aqueous inkjet printing of biomolecules in native biological conditions at unprecedented diluted concentrations (i.e. nanomolar concentration) to the few-molecule sensitivity of RICS. We here take advantage of inkjet printing to produce droplets having volumes from picoliter to nanoliter scale.

The results of this work have led to the publication of an article entitled "*Monitoring few molecular binding events in scalable confined aqueous compartments by raster image correlation spectroscopy (CADRICS)*" on Lab on a Chip journal (*Lab. Chip.* 24, 4666–4676 (2016)).

Bibliography

1. Arrabito, G., Galati, C., Castellano, S. & Pignataro, B. Luminometric sub-nanoliter droplet-to-droplet array (LUMDA) and its application to drug screening by phase I metabolism enzymes. *Lab Chip* **13,** 68–72 (2013).

2. Gruner, P. *et al.* Controlling molecular transport in minimal emulsions. *Nat Commun* **7,** (2016).

3. Benters, R., Niemeyer, C. M. & Wöhrle, D. Dendrimer-Activated Solid Supports for Nucleic Acid and Protein Microarrays. *ChemBioChem* **2,** 686–694 (2001).

4. Arrabito, G. & Pignataro, B. Inkjet printing methodologies for drug screening. *Anal. Chem.* **82,** 3104–3107 (2010).

5. Ryan, A. J., Gray, N. M., Lowe, P. N. & Chung, C. Effect of Detergent on 'Promiscuous' Inhibitors. *J. Med. Chem.* **46,** 3448–3451 (2003).

6. Baret, J.-C. Surfactants in droplet-based microfluidics. *Lab Chip* **12,** 422–433 (2012).

7. Rossow, M. J., Sasaki, J. M., Digman, M. A. & Gratton, E. Raster image correlation spectroscopy in live cells. *Nat. Protoc.* **5,** 1761–1774 (2010).

8. Brown, C. M. *et al.* Raster image correlation spectroscopy (RICS) for measuring fast protein dynamics and concentrations with a commercial laser scanning confocal microscope. *J. Microsc.* **229,** 78–91 (2008).

9. Derby, B. Inkjet Printing of Functional and Structural Materials: Fluid Property Requirements, Feature Stability, and Resolution. *Annu. Rev. Mater. Res.* **40,** 395–414 (2010).

10. H.Dong, Carr, W. W. & Morris, J. F. An experimental study of drop-on-demand drop formation. *Phys. Fluids* **18,** 72102 (2006).

11. Dong, H., Carr, W. W. & Morris, J. F. An experimental study of drop-on-demand drop formation. *Phys. Fluids* **18,** 72102 (2006).

12. Eggers, J. Nonlinear dynamics and breakup of free-surface flows. *Rev. Mod. Phys.* **69,** 865–930 (1997).

13. H.Y. Gan, X. Shan, T. Eriksson, B. K. L. and Y. C. L. Reduction of droplet volume by controlling actuating waveforms in inkjet printing for micro-pattern formation. *J. Micromechanics Microengineering* **19,** 55010 (2009).

14. Arrabito, G. *et al.* On the relationship between jetted inks and printed biopatterns: molecular-thin functional microarrays of glucose oxidase. *Langmuir Acs J. Surfaces Colloids* **25,** 6312–6318 (2009).

15. Sun, Y., Chen, X., Zhou, X., Zhu, J. & Yu, Y. Droplet-in-oil array for picoliter-scale analysis based on sequential inkjet printing. *Lab Chip* **15,** 2429–2436 (2015).

16. Talbot, E. L., Berson, A., Brown, P. S. & Bain, C. D. Evaporation of picoliter droplets on surfaces with a range of wettabilities and thermal conductivities. *Phys. Rev. E* **85,** 61604 (2012).

17. Feng, B. Y. & Shoichet, B. K. A detergent-based assay for the detection of promiscuous inhibitors. *Nat. Protoc.* **1,** 550–553 (2006).

18. F. Höfling & Franosch, T. Anomalous transport in the crowded world of biological cells. *Reports Prog. Phys.* **76,** 46602 (2013).

19. Hansen, M. M. K. *et al.* Macromolecular crowding creates heterogeneous environments of gene expression in picolitre droplets. *Nat Nano* **11,** 191–197 (2016).

20. Chen, Y.-Y., Chen, Z.-M. & Wang, H.-Y. Enhanced fluorescence detection using liquid-liquid extraction in a microfluidic droplet system. *Lab Chip* **12,** 4569–4575 (2012).

21. Nishioka, G. M., Markey, A. A. & Holloway, C. K. Protein Damage in Drop-on-Demand Printers. *J. Am. Chem. Soc.* **126,** 16320–16321 (2004).

22. Calvert, P. & Boland, T. Biopolymers and Cells. in *Inkjet Technology for Digital Fabrication* 275–305 (John Wiley & Sons, Ltd, 2012). doi:10.1002/9781118452943.ch12

23. Lionello, A., Josserand, J., Jensen, H. & Girault, H. H. Dynamic protein adsorption in microchannels by 'stop-flow' and continuous flow. *Lab Chip* **5,** 1096–1103 (2005).

24. Buschmann, V., Weston, K. D. & Sauer, M. Spectroscopic Study and Evaluation of Red-Absorbing Fluorescent Dyes. *Bioconjug. Chem.* **14,** 195–204 (2003).

25. H Keilacker, W Besch, K.P. Woltanski, J.M. Diaz-Alonso, K.D. Kohnert, M. Z. Mathematical Modelling of Competitive Labelled-Ligand Assay Systems. Theoretical Re-Evaluation of Optimum Assay Conditions and Precision Data for Some Experimentally Established Radioimmunoassay Systems. *Clinical Chemistry and Laboratory Medicine* **29,** 555 (1991).

26. J. Strömqvist, L. Nardo , O. Broekmans, J. Kohn, M. Lamperti, A. Santamato, M. Shalaby, G. Sharma, P. Di Trapani, M. Bondani, R. R. Binding of Biotin to Streptavidin: A combined fluorescence correlation spectroscopy and time-resolved fluorescence study. *Eur. Phys. J. Spec. Top.* **199,** 181–194 (2011).

27. Illaste, A., Laasmaa, M., Peterson, P. & Vendelin, M. Analysis of Molecular Movement Reveals Latticelike Obstructions to Diffusion in Heart Muscle Cells. *Biophys. J.* **102,** 739–748 (2012).

28. Grilli, S. *et al.* Active accumulation of very diluted biomolecules by nano-dispensing for easy detection below the femtomolar range. *Nat Commun* **5,** (2014).

29. Shigeta, K. *et al.* Functional Protein Microarrays by Electrohydrodynamic Jet Printing. *Anal. Chem.* **84,** 10012–10018 (2012).

5 Molecular Confinement in fL Aqueous Compartments

Biological compartmentalization is a fundamental principle of life that allows cells to metabolize, propagate, or communicate with their environment. Today much research is devoted to understanding this basic principle and to harness biomimetic compartments and catalytic cascades as tools for technological processes[1]. Molecular confinement is known to lead to acceleration of molecular dynamics by decreasing spatial dimensions of the confining space, along with surface effects due to interactions with the molecular container's walls[2]. Nature employs confinement in molecularly crowded, heterogeneous, specialized femtoliter (fL) compartments inside living cells for spontaneously achieving higher reaction efficiency and spatial-programming of complex, multi-step biochemical processes[3]. Man-made aqueous compartments can trigger the formation of heterogeneous environments with unique properties[4,5]. However, current compartment fabrication approaches impose constrains in terms of fluid composition and conductivity[6–9] and are not able to combine crowding and confinement which hamper general application on bespoke systems.

In this chapter we show a novel printing approach to produce stable fL-scale aqueous droplets inside mineral oil for studying molecular confinement. We tailor the fabrication of fL droplets by a "field-free" -i.e. in absence of electrolytes[7] - piezoelectric inkjet printing in which a novel actuating waveform is used to produce femtoliter scale aqueous droplets by picoliter sized nozzles.

The droplets form an almost-regular circular droplet network pattern at the border of mineral oil droplet, given their negligible frictional force in mineral oil phase. Molecules in such fL scale compartments form ring patterns at the surfactant/oil interface due to spontaneous adsorption phenomena at the interface which, finally, bring to molecular concentration at the border and depletion at bulk. Inside fL droplets solute-solvent and solvent driven solute-solute interactions are modified with respect to bulk case as demonstrated by variation of fluorescence life time of environmental-sensitive molecules. By fluorescence life-time imaging (FLIM) on single droplets, we show that molecular confinement leads to a decrease of fluorescence life-time of environment-sensitive molecular systems (such as Streptavidin-Biotin or FITC dye), but not to significant increase of local viscosity-sensitive molecules (CCVJ dye) or environment insensitive dyes (Alexa dyes). Confinement at ring pattern leads to molecular crowding, likely due to co-adsorption at the aqueous/oil interface of biomolecules and surfactants.

We exploit such confinement process by a model DNA beacon molecular machine, finding out that fluorescence signal switching-on is triggered at lower DNA target concentrations with respect to macrovolumes. Therefore, self-assembled annular-patterns constitute a totally novel tool for investigating molecular dynamics in confined and crowded environments.

5.1 Materials and Methods

5.1.1 Chemicals and solutions preparation

Water-in-oil droplet microarrays have been fabricated on coverslip glasses (Corning 24 × 50 mm, cover glass) made from borosilicate glass (0.13–0.16 thick) which are compatible with confocal microscopy set-ups.

All solutions were prepared in ultrapure Millipore water (Direct Q-UV filtration system, 18.2 MΩ cm). The pH was controlled by a pH meter (pH 700, Eutech Instruments).

With the exception of DNA molecular machines, a buffer containing 100 mM phosphate buffer aqueous solution (pH 7.4), 0.05% v/v Tween-20 (polyoxyethylene (20) sorbitanmonolaurate, Sigma Aldrich), and 0.03% w/v F108 poly(ethylene glycol)-block-poly(propylene glycol)-block-poly(ethylene glycol) was employed for all the experiments. In the case of DNA molecular machines solutions, NaCl at the final concentration of 50 mM was added at the previous buffer composition.

The following molecular systems solutions were employed at these final concentrations: Alexa 647 10 μM (Alexa Fluor® 647 carboxylic acid, succinimidyl ester, ThermoFisher Scientific), FITC 10 μM (Fluorescein Sodium, suitable for fluorescence, Sigma Aldrich), BSA-FITC 10 μM (Albumin-Fluorescein isothiocyanate conjugate bovine, Sigma Aldrich), BSA 1.2 μM (Sigma Aldrich, lyophilized powred, ≥96.0% agarose gel electrophoresis) and FITC 10 μM mixture, CCVJ 10 μM (9-(2-Carboxy-2-cyanovinyl)julolidine Sigma Aldrich suitable for fluorescence, ≥97.0% HPLC), BSA 10 μM and CCVJ 10 μM mixture, ANS 3 μM (8-anilinonaphthalene-1-sulfonic acid, Sigma Aldrich), BSA 10 μM and ANS 3 μM mixture. DNA molecular beacon solution was prepared from a 100 nM stock solution, and finally diluted to 10 nM in all the experiments.

DNA Target 15-mer (5'-DNPttttttttttttttttCGAATTAGGCTATAC-3') was prepared from a 10 μM stock solution and was employed at concentrations ranging from 1 nM to 1μM. DNA molecular beacon (t(Alexa555) gagcg GTA TAG CCT AAT TCG cgctc t (BHQ2) ctgtcactttctgag -3') and DNA target incubation was carried out for 30 minutes at room temperature.

Stock solutions of Atto655-biotin (Bio-Reagent, suitable for fluorescence, Sigma Aldrich) were prepared in anhydrous DMSO and diluted at 4 μM. Streptavidin (4 μM) (from Streptomyces avidinii affinity purified, lyophilized from 10 mM potassium phosphate, Sigma Aldrich) /Atto655-biotin (4 μM) incubation was carried outfor 30 minutes at room temperature.

5.1.2 Functionalization of glass surfaces

Glass coverslips were extensively rinsed in ethanol and water to remove organic contaminants. After that they were treated with a UV Ozone Cleaner – ProCleaner (BioforceNanosciences) for 30 minutes in order to increase the hydrophylicity of the surface. Subsequently, the coverslips were coated with 1H,1H,2H,2H-perfluorooctyltriethoxysilane (2% v/v in ethanol) by sandwich

incubation method for 1 hr at room temperature (see **figure 4.1**). Subsequently to coating with 1H,1H,2H,2H-perfluorooctyltriethoxysilane, the slides were washed with ethanol and put in oven at 110 °C for 1 hr. After that, the coverslips are stored dry at -20°C until use.

5.1.3 Molecular inkjet dispensing

Picoliter droplets were dispensed on glass substrates by using a Dimatix Materials Printer (DMP-2800, Fuji Film) reported in **figure 4.2**.

Mineral oil droplets were dispensed by using double pulse waveform at 5 kHz and 10 pL jetting cartridges at temperatures of 33°C and at voltages of 28 V. An ensemble of 1000 droplets of oil (drop-to-drop pitch of 5 μm) formed a single droplet of 10 nL by coalescence. We fabricated mineral oil microarrays in the form of a 4×2 format of 10 nL drops with a spacing of 1 mm. On the top of these droplets, fL-scale droplets were dispensed by using designed "spiked" waveform and 1 pL jetting cartridges at room temperature and at voltages between 13 V and 15 V.

5000 fL droplets of aqueous ink were printed on top of mineral oil droplets (a drop-to-drop pitch of 40 μm was set to avoid droplets coalescence). The fL-scale droplets were completely engulfed inside the mineral oil, lying at the border of the mineral oil droplets.

5.1.4 Confocal microscopy and FLIM analysis

Confocal images of fL droplets were acquired in one channel with an Olympus FluoView1200 confocal laser scanning microscope (Olympus) using 60x 1.35 NA objective. We used 515 nm laser to excite the Alexa 555 dye of DNA molecular beacon. The bandwidth of the emission filter used for the red emission channel is 550-650 nm. Data were collected in the photon-counting mode. The scan area was 512x512 pixels, the pixel size was set at 0.05 μm and the scan speed was 4 μs/pixel, (line time was 2.120 ms and frame time was 0.564 s).

Droplets confocal images were exported with FV10-ASW 4.1 Viewer. By means of the images processing and analysis program Image J (1.46r version) we obtained the parameters related to the size and shape of the fL droplets encapsulated with inkjet printing into mineral oil droplets. From an average of 120 fL aqueous droplets in oil, we obtained average values of diameter and perimeter of 3.5 μm ± 1.0 μm and 10 μm ± 2 μm, respectively. The thick of fL ring-pattern is less than 1 μm.

For FLIM analysis 256 × 256 pixels image stacks were sequentially acquired using a Leica TCS SP5 confocal scanning microscope with a 63x oil objective (Leica Microsystems, Germany, **Fig.5.1**). Measures were performed with a frequency of 200 kHz. 2-Photon excitation was set at 780 nm (Spectra-Physics Mai-Tai Ti:Sa ultra-fast laser) for ANS and ANS/BSA mixture, using a detection range of 400-650 nm, a laser power of 2% and a pinhole of 600 μm. For CCVJ and CCVJ/BSA system 2-Photon excitation was set at 830 nm and the emission range at 450-650 nm.

The white laser was used for FITC, Alexa 647, Atto655-BTN, DNA molecular beacon and was set at 488 nm, 647 nm, 655 nm, 515 nm, respectively.

Fluorescence decay was initially evaluated with SymPhotime Analysis software, subsequently FLIM images were exported and analyzed using the SimFCS 3.0 program (Laboratory for Fluorescence Dynamics, University of California, Irvine, CA) to calculate fluorescence lifetime with the phasor method[10].

Figure 5.1: Leica TCS SP5 confocal scanning microscope, Leica Microsystems, Germany.

5.2 Sub-nozzle Resolution Inkjet Printing

In inkjet printing operation, for a normal input pulse consisting in a pushing stage and then a pulling stage, the droplet size is usually similar or slightly larger than the nozzle size. This boundary condition is due to the fact that during the pushing stage, the meniscus formed at the exit and protruding from the nozzle. The size of the meniscus is dependent on the boundary conditions imposed by the orifice's walls. In order to reduce droplet size without reducing nozzle size, efforts have considered the application of double polarity square waves[11]. This approach shows drawbacks since it leads to the generation of unwanted satellites along with the main droplet. An alternative approach is to impose oscillating conditions onto the protruded meniscus as it is exits the nozzle.[12] This approach also shows issues due to the strict dependence on the imposed oscillation frequency and can be influenced by manufacturing defects within the nozzle orifice. A recent report demonstrate the possibility to scale droplet size down to submicrometer scale by sucking back the liquid from a sessile droplet initially suspended from a nozzle without applying external fields[13]. However, the generation of droplets depends upon the Rayleigh-Plateau instability and requires high Capillary number and thus suits better for high viscosity and low surface tension inks.

We here considered the singularity[14] that the Navier-Stokes equations (i.e. the equations that can be applied to describe the motion of viscous fluid substances) form as the height of the fluid neck goes to zero – i.e. close to pinch-off. In this situation, the solutions of the Navier-Stokes equation have a scaling form characterized by a set of universal exponents. The natural length and time units of singularity are given by:

$$l_v=\eta^2/\gamma\rho \quad \text{and} \quad t_v=\eta^3/\gamma^2\rho$$

in which η is the viscosity, ρ is the density and γ is the surface tension.
Length and time distances from singularity are measured by $z'=(z - z_0)/l_v$ and $t'=(t - t_0)/t_v$. In the pinch region, meaning that $|z'| \ll 1$ and $t' \ll 1$, h(z,t) and v(z,t) are expected to have the scaling form:

$$h(z,t) = l_v t'^{\alpha 1}\varphi(z'/t'^{\beta})$$
$$v(z,t) = (l_v/t_v)t'^{\alpha 2}\Psi(z'/t'^{\beta})$$

The correct exponents α1, α2 and β can be inferred from dimensional analysis by seeking for regularity properties of the functions h and v as one of the physical parameters η, γ or ρ goes to zero. From the mathematical analysis of Eggers[14], the width of the pinch region scales like $t'^{1/2}$, whereas the height of the liquid thread scales like t'. This means that, the droplet at the moment of pinch-off forms a long and thin neck as $t' \rightarrow 0$. The expression for the minimum height h_{min} and maximum velocity v_{max} are given by: $h_{min}=0.0304(\gamma/\eta)(t_0 - t)$ and $v_{max}= 3.07(\eta/\rho)^{1/2}(t_0 - t)^{-½}$.
Eggers demonstrated the usefulness of his model by predicting the minimum height h_{min} and maximum velocity v_{max} for pinching-off of glycerol.
In this work, we show the possibility to obtain, for the first time, a liquid thread with the lowest possible volume (at femtoliter scale) from a 10 μm microfluidics by striving to reach such singularity. This approach would permit to reach the lowest possible droplet volume, and would be applicable to different nozzle length scales, given that the behaviour is scale-free. Importantly, the *jetting time* has to be selected as minimum possible for the inkjet device (i.e. 0.5 microseconds in our case). Accordingly, such "spiked" wave is followed *by a longer phase* at zero voltage in order to facilitate sucking back into the nozzle. In this scenario, we had to firstly investigate the effect of jetting potential upon liquid thread length and stability. Whereas pinch-off time is not strictly dependent upon *jetting voltage*[15], the length of the liquid thread at pinch-off from the nozzle exit is known to increase as a function of jetting voltage. The liquid thread exiting from nozzle is able to contract into a single drop without breaking up if the length of liquid thread at pinch-off, l_b, does not exceed a limiting value l_b* as from the following equation[15]:

$$\frac{l_b}{R_{noz}} < \zeta\frac{1}{\alpha^*_{max}} + 2 = \frac{l_b^*}{R_{noz}}$$

where R_{noz} is the radius of the nozzle; $\zeta = (C_2\text{-}C_1)\cdot a$ is a measure of the times difference for the formation of the droplets at the nozzle exit C_1 and at complete pinch-off C_2, being a constant value. ζ is usually comprised between 0.9 and 1.1; α_{max}^* is given by the following expression:

$$\alpha_{max}^* = \sqrt{\frac{1}{2}x^2(1-x^2) + \frac{9}{4}x^4} - \frac{3}{2}Oh \cdot x^2$$

where

$$x^2 = \frac{1}{2 + \sqrt{18} \cdot Oh}$$

in which Oh is the Ohnesorge number which is given by:

$$Oh = \frac{\mu}{\sqrt{\rho\sigma L}}$$

Where

ρ is the liquid density (g/cm^3)

σ is the surface tension (dyne/cm)

L is the characteristic length scale (i.e drop diameter)

μ is the dynamic viscosity of the fluid (cP)

From this model, it turns out that for our aqueous ink, by considering that surface tension is decreased up to 30mN/m, we obtain that Oh is almost 0.083, being α_{max}^* is equal to 0.705 which determine a $\frac{l_b^*}{R_{noz}}$ ratio of about 3.4.

From the previously explained singularity condition for length $l_v=\eta^2/\gamma\rho$ and time ($t_v=\eta^3/\gamma^2\rho$), we find that values are respectively on the order of 30 nm and 0.025 µs. In our experimental conditions, we set total actuation time equal to 0.5 µs, which leads to a h_{min} in the order of around 1 micron. Importantly, model from Eggers[14] predicts that liquid thread forms a long and thin neck (width of the pinch region scales like $t'^{1/2}$, whereas the height of the liquid thread scales like t'). Since $t' << 1$, the $\frac{l_b^*}{R_{noz}}$ ratio is expected to be higher than previously calculated threshold values and hence, it leads to the formation of satellites.

We experimentally found out that jetting potential (investigated in the range from 15 V to 40 V), significantly affected droplet emission dynamics at the same drop jetting time phase (i.e. 0.5 µs) (**Fig. 5.2**). As previously predicted, ejected drop leads to the formation of satellites already at very low jetting voltages (i.e. 14-15 V). A rounded satellite droplet is formed at the front of the jetted liquid thread, having a droplet radius of few microns, in accord with Eggers' model[14]. Remarkably, the remaining part of the droplet is sucked back in the nozzle- thus not contributing to increasing droplet volume.

On the other side, by increasing jetting voltage to 20 – 25 V, in addition to the femtoliter scale droplet, the main droplet also pinches off from the nozzle, because liquid thread length increases by increasing jetting voltage, being respectively 30 µm at 20 V and 35 microns at 25 V. This thread finally retracts and forms another droplet with higher volume (around 6-7 times the droplet diameter) in addition to the first one.

At 30-35 V, the liquid thread which pinches off from nozzle still increases its length up to 60 µm and brings to the formation of two droplets. At the highest possible jetting voltage (i.e. 40 V), liquid thread reaches almost 65 µm length and gives rise three droplets. Accordingly, whereas pinch-off length and thus droplet formation is clearly dependent upon jetting voltage, pinch-off time is not dependent on pinch-off voltage as expected[15].

On the other side, by increasing jetting voltage (>18 V), the ejected liquid thread gives rise to the typical picoliter scale spherical droplet without liquid thread contraction back in the nozzle. Finally, by increasing jetting voltage to higher values (>30 V), liquid tongue increased in size also resulting in multiple droplet breakups and satellites formation (**Fig. 5.3**). This means that application of low voltage jetting is also beneficial for jetting frequency did not produce significant variations on droplet speed and shape.

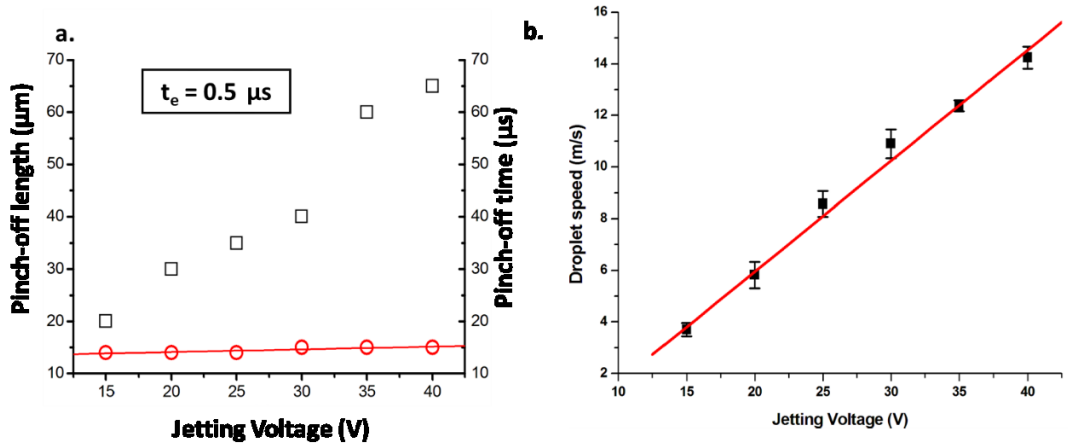

Figure 5.2: (a) Effect of Jetting Voltage on Pinch-off length and Pinch-off time, i.e. respectively, length at which droplet detaches from nozzle and time at detachment occurs. (b) Droplet speed as a function of Jetting Voltage by employing "spike" waveform at t_e = 0.5 µs.

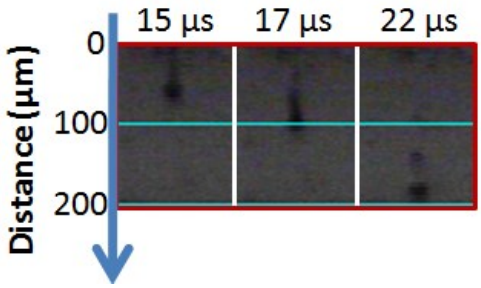

Figure 5.3. Stroboscopic images showing droplet jetting by "spike" waveform at 40 V of a solution containing 4µM of atto655-BTN (0.03% F-108, 0.05% Tween20).

5.3 Self-assembled Aqueous Confinement Platform

Differently from above reported artificial platforms, molecular evolution has chosen to adopt both strategies confinement and crowding by combining a high-volume fraction of macromolecules and static barriers to molecular movement in order to increase efficacy of biochemical reactions. There is then an urgent need to adopt a general strategy to fabricate crowded and confined bespoke environments to truly characterize the behaviour of artificial and biochemical reaction systems in evolutionary selected conditions. An ideal solution to the fabrication of compartment is constituted by printing. In fact, in comparison with microfluidic setups or emulsification methods, printing approaches are suitable for addressable production of droplets, automation and operation under digital control[16,17,18]. Among printing techniques, inkjet printing represents an ideal choice, given its simplicity, additive nature and adaptability to inks of different nature. We already showed that homogenous nanoliter scale environments can be easily assembled by inkjet printing, allowing for the investigation of few molecular binding interactions inside aqueous droplet arrays[19]. Droplets by inkjet printing are normally up to picoliter scale, being droplet size dependent on the nozzle size, which is typically not below 10 µm. Recent approaches show the possibility to reduce droplets volume down to the attoliter scale by <10 µm nozzle radius[20] or by electric field aided hydrodynamically dispensing[13], however these approaches respectively can cause nozzle clogging or require electrolyte media support in the solution.

Here, a novel actuating waveform that permits to assemble for the first time fL aqueous droplets from 10 µm size nozzles, by a "field-free" piezoelectric inkjet, is shown. Autonomous molecular assembly of molecular annulus at the interface with oil phase triggers a unique synergy of molecular confinement and crowding inspired by natural systems. We show potentiality of the approach by accelerating the hybridization-driven opening of a DNA molecular beacon in presence of target sequence.

We design a novel waveform signal (**Fig. 5.4a**) which is able to produce fL droplet dispensing by our three phases waveform. Whereas only the second phase corresponds to droplet jetting (i.e. t_e), the first and thirds parts permit to pull back liquid tongue in the nozzle orifice. We printed an aqueous ink containing 0.03% (v/v) of F-108 copolymer (poly(ethylene glycol)-block-poly(propylene glycol)-block-poly(ethylene glycol)) and 0.05% Tween 20 by the proposed "spike" waveform. Our selected ink is aqueous and thus, leads to satellites production. Intentionally, we chose a t_e (ejection time) value to be the minimum possible time interval selectable for our device (i.e 0.5 µs) in order to meet the singularity criterion demonstrated by Eggers's model which predicts reduction of droplet size by reducing droplet formation time[14] (**Fig. 5.4b**). At low jetting voltages (14 V- 16 V and droplet speeds of about 4 m/s), the liquid thread exiting from nozzle resulted in a front spherical sub-nozzle size droplet detaching from the main liquid thread (see **Fig. 5.4c**). At the same time, the remaining liquid thread remained in the nozzle since it was pulled

inside it by the second phase of the waveform (90 µs duration). At higher voltages, liquid thread was ejected together with droplet (see **Fig. 5.4d**). Details on the effects of jetting voltages have been reported in Chapter 5.

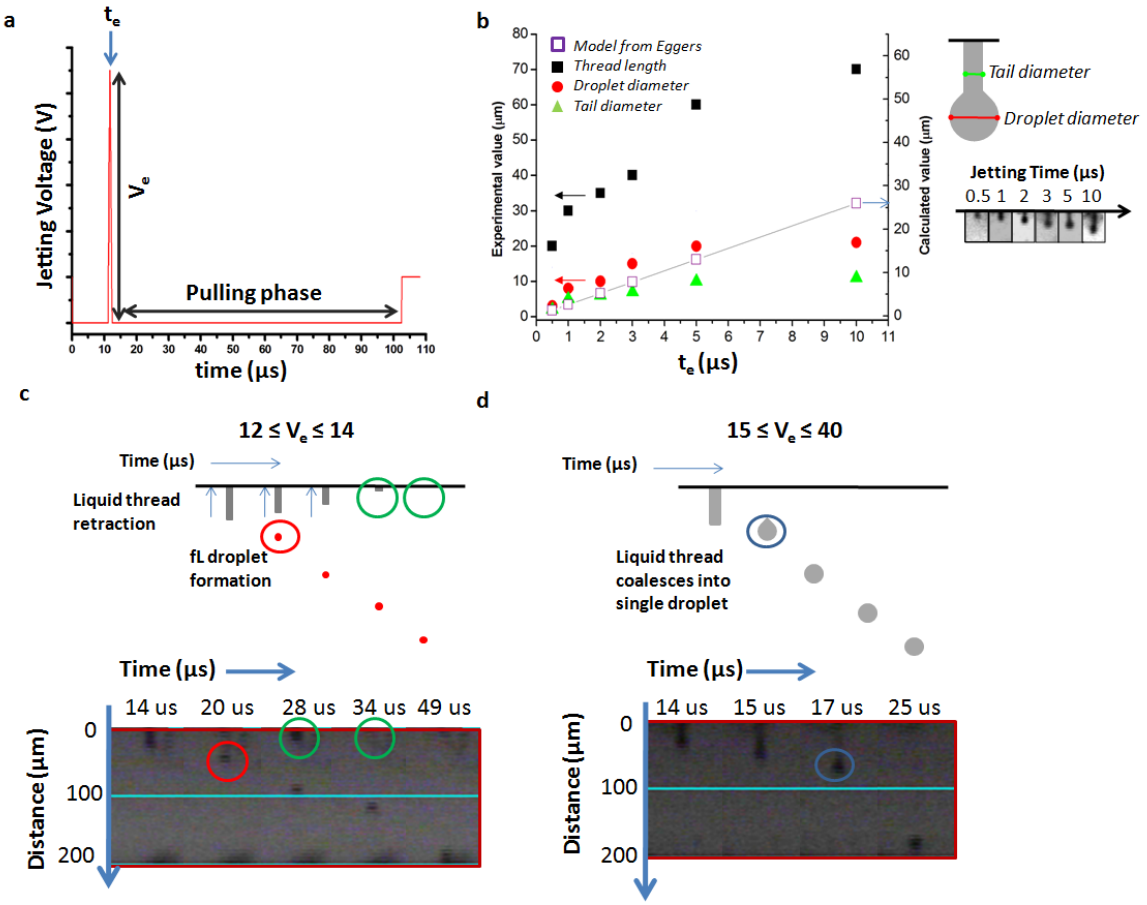

Figure 5.4: Aqueous femtoliter droplet dispensing by "spike"waveform. (a) Piezoelectric driving "spike" waveform for ejecting femtoliter scale droplets from picoliter scale nozzles. The ejection phase is equal to 0.5 µs. Pulling phase lasts 90 µs ($t_e$is time of droplet ejection, V_e is the jetting potential at droplet ejection). (b) Droplet jetting dynamics as a function of t_e (time of ejection). Stroboscopic images showing droplet jetting by "spike" waveform at 12 V. (c) and at 25 V (d) of a solution containing 4µM of Atto655-BTN (0.03% F-108, 0.05% Tween20). Femtoliter scale spherical droplet pinches-off at 20 µs (see red circle), whereas liquid tail remains attached at the nozzle exit and eventually is pulled back after 34 µs (see green circle), so permitting to reduce droplet volume below nozzle size. Blue circle denotes a droplet formed at 25 V in case liquid thread exiting nozzle coalesces into a single nozzle-sized droplet.

In comparison with picoliter-sized droplets, fL droplets experience a significantly lower frictional force (also defined as Stokes' drag) in mineral oil whilst moving in the mineral oil at speeds of about 4 m/s by ejecting them at the same speed of picoliter scale droplets. The expression of the Stokes' drag is the following:

$$F_d = 6\pi\eta r v$$

in which η is the dynamic viscosity, r is the radius of the spherical droplet and v is the flow velocity relative to the object.

At similar dynamic viscosity and flow velocity, frictional force for femtoliter droplets would be 6-7 times lower than that for picoliter droplets – hence their trajectory is longer until they reach the border of the oil droplet, forming an almost-regular droplet network pattern, arranged according to a circular geometry (see **Fig. 5.5a** and **5.5b**). Self-assembling of an adsorptive molecular layer - with thickness on the scale of hundreds of nanometers for 0.1-1 µM concentrated solutions - occurs in time scale of seconds at water/oil interface according to models - i.e. adsorption isotherms such as Frumkin and Szyszkowski isotherms[21] based on the Fick's transient diffusion law. Confinement at border is a concentration-dependent phenomenon, being more evident for 0.1-100 nM bulk concentration range, leading to molecular depletion of internal zone, whereas at micromolar concentration, concentration of inner zone is only reduced with respect to the droplet border.

Molecules and surfactant molecules compete in the process of absorption at the interface. However, we chose surfactant concentrations higher than molecules dissolved in the droplet, so that surfactant confine at the water/oil interface in order to leave molecules apart from the interface with oil phase[22], leading to molecular confinement at PEG-PPG-stabilized interfaces (**Fig. 5.5 c**).

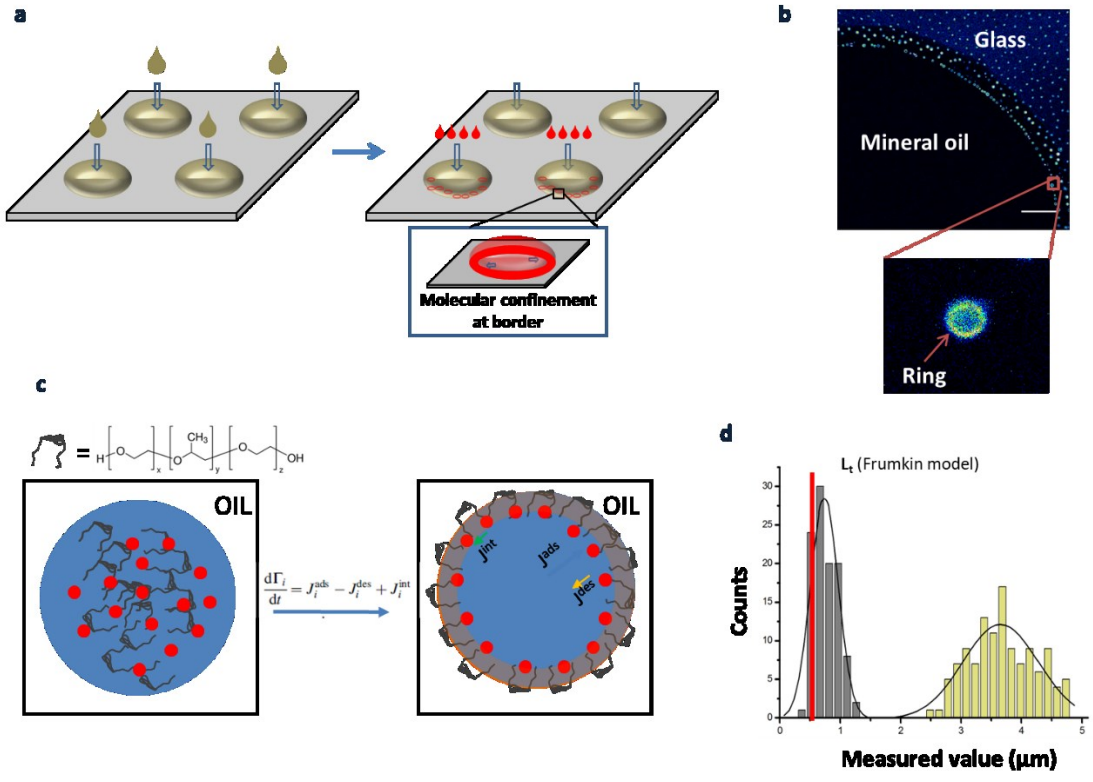

Figure 5.5: Self-assembled molecular annular confinement at water/oil interface. (a) Sequential preparation of fL aqueous compartments inside nL-scale mineral oil droplets. Molecules spontaneously self-assemble 500-nm thick ring at the water/oil interface. (b) Fluorescence images of Alexa 647 (10µM) fL droplets showing ring-assembly. (c) Scheme of the spontaneous molecular ring assembly of F108 and molecules (red circles), in which J_{ads} is the adsorptive flux, J_{des} is the desorptive flux and J_{int} is the internal source flux. J_{int} results from the reorganization of adsorbed molecules at the water/oil interface. (d) Droplets size and corresponding ring-thickness (average of

120 droplets). Average value of ring thickness is in agreement with values predicted by Frumkin-isotherm numerical models for adsportion at water/oil interface by excluding electrostatic effects.

5.4 Fluorescence Lifetime Imaging Analysis

5.4.1 Molecular confinement of molecular probes in fL droplets

Coupling of molecular crowding and confinement is investigated by fluorescence life time imaging microscopy (FLIM) on probe molecules. In general, fluorescence lifetime (τ) measures the exponential decay rate (via time) of a fluorophore from the its excited state to the radiative fluorescence emission[23]. τ, here obtained by phasors approach, is highly sensitive to the multiple aspects of local fluorophore environment within 10-0.1 nm length scale. Remarkably, molecules which are environmental insensitive (such as Alexa fluorophores – i.e. Alexa 647) do not display any significative difference in τ when ring-confined as can be seen in **Fig. 5.6a** (10 μM, τ_{bulk} = 1 ns, τ_{fL}= 1 ns)). On the other hand, environmental sensitive molecules such as FITC shows a decrease of τ between bulk and fL droplets (10 μM, τ_{bulk} = 4 ns, τ_{fL}= 2 ns) (**Fig. 5.6b**). This is likely due to self-quenching effects – i.e. non-radiative energy migration between FITC neighbouring molecules. The distance for FITC-FITC interaction that leads to self-quenching is reported to be on the order of 5 nm, according to mechanisms dye dimerization, energy transfer to non-fluorescent dimers and also collisional quenching interactions between dye monomers.[24] Viscosity in fL droplets is not significantly modified with respect to bulk (10 μM concentration, both 0.2 ns) (**Fig. 5.6c**) as probed by a model molecular rotor CCVJ, 9-(2-Carboxy-2-cyanovinyl)julolidine, whose fluorescence lifetime increases in presence of highly-viscous environments[25]. We finally sought to investigate molecular crowding effects by measuring τ on FITC as conjugate with Bovine Serum Albumin (BSA-FITC 10 μM) or as in mixture with the same protein (BSA 1.2 μM and FITC 10 μM). τ values in fL are almost equal between mixture and conjugate (τ_{fL} = 0.5 ns) and are both lower than corresponding bulk solution values (τ_{mix} = 4 ns and $\tau_{conjugate}$ = 2 ns); this demonstrates that molecular crowding effectively takes place (**Fig. 5.6d**).

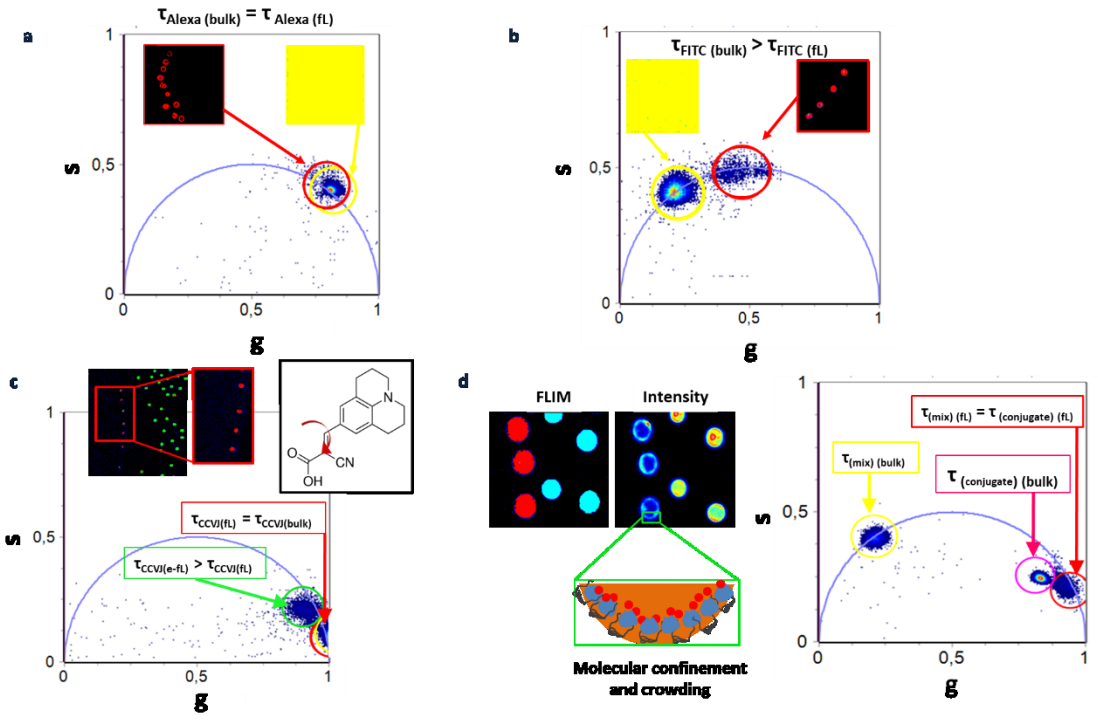

Figure 5.6: Coupling of molecular crowding and confinement in fL-droplets. (a) Environmental insensitive Alexa 647 (10 μM) shows τ(bulk) = τ(fL). (b) Environmental sensitive Fluorescein (FITC) show significative decrease in τ n fL-droplets with respect to bulk. (c) Molecular viscosimeter CCVJ does not show any increase of τ in fL-droplets, thus demonstrating lack of local viscous increase at confinement. (d) Mixture of BSA and FITC (BSA 1.2 μM and FITC 10 μM) and BSA-FITC conjugate (10 μM) result in an identical τ, demonstrating the simultaneous presence of confinement and crowding.

Protein conformation is affected by molecular crowding and confinement in fL droplets. We prove this by employing ANS (8-Anilinonaphthalene-1-sulfonic acid) probe, which is able to interact with hydrophobic domains of proteins[26], causing an increase of τ. We found a decrease in fluorescence lifetime (τ) of ANS in mixture with BSA from bulk to fL (τ_{bulk} = 11 ns vs τ_{fL} = 3.4 ns), likely because of the lower protein surface exposure to the dye due to a more compact protein structure, in accord with crowding theory[2].On the other hand, CCVJ probe shows an increase of τ in presence of BSA from τ_{bulk} = 0.6 ns to τ_{fL} (center) = 1.1 ns and τ_{fL} (edge) = 0.7 ns. This is due to the higher rigidity of the microenvironment which also inhibits the intramolecular rotation, leading to an increase in CCVJ quantum yield, and thus fluorescence lifetime[27] (**Fig. 5.7**). CCVJ and ANS in presence of BSA lead to a heterogeneous distribution of fluorescence lifetimes: τ_{fL} (edge) < τ_{fL} (center). This behaviour can be explained by a concentration gradient of BSA in the droplet, due to the unbalance of negative charges due to the anionic characters of the probes which impedes confinement at the border whilst maintaining crowding; remarkably, all confinements model proposed so far have always neglected electrostatic effects. These observations permit to conclude that confinement at border modifies spectroscopic properties of probes molecules (**Table 5.1**), albeit not affecting local viscosity since PEG-PPG is mainly at interface with oil phase, reduces

available volume due to the PEG-induced depletion force which increases molecular local concentration and likely modifies conformation of protein molecules, as known from confinement effects in droplets which tend to compact protein structures[28].

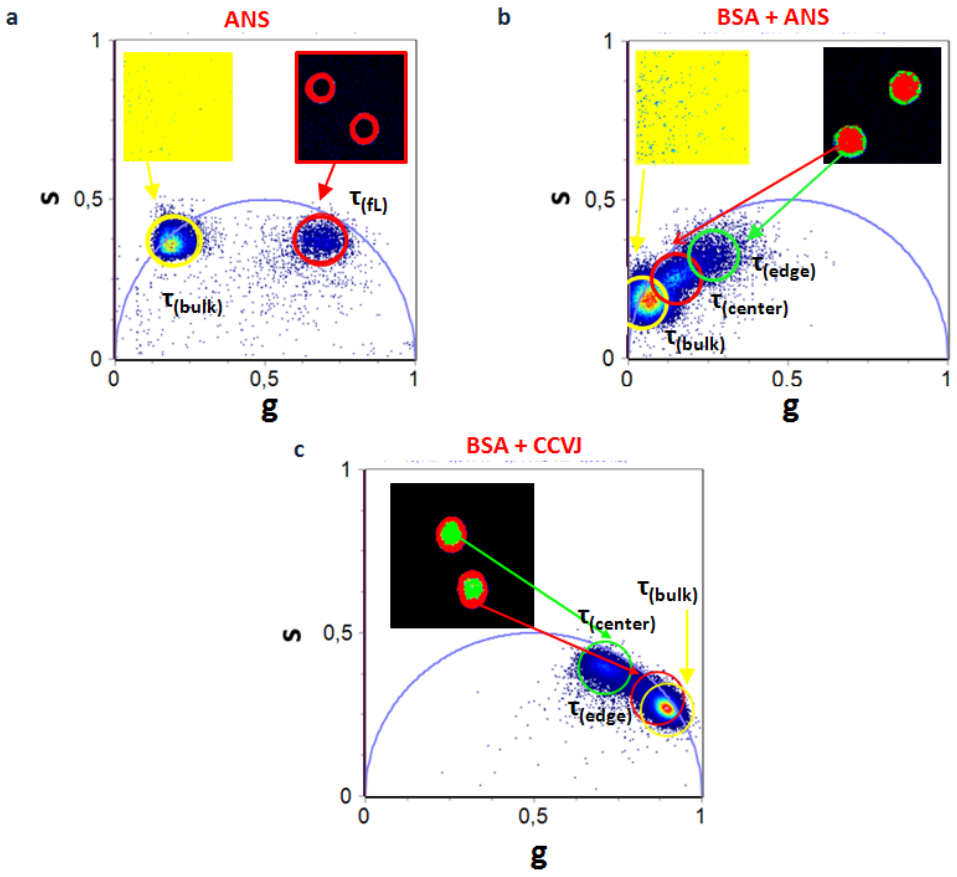

Figure 5.7: (a) Fluorescence lifetimes (τ) of fL droplets containing ANS (3 µM) in comparison with bulk values. (b) Fluorescence lifetimes (τ) of fL droplets containing BSA (10 µM) mixed with ANS (3 µM) in comparison with bulk values. (c) Fluorescence lifetimes (τ) of fL droplets containing BSA (10 µM) mixed with CCVJ (10 µM) in comparison with bulk values. For both (b) (BSA +ANS) and (c) (BSA + CCVJ) cases, droplets form heterogeneous distribution of τ (lower value at droplet edge, higher value at droplet center).

	τ (ns)	
	50 uL	fL droplets
Alexa647 10 µM	1	1
Atto655-BTN 4 µM	2.2	2.3
Atto655-BTN 4 µM + STV 4 µM	1.1	0.8
FITC 10 µM	4.0	2.0
BSA-FITC 10 µM	2.0	0.5
BSA 1.2 µM + FITC 10 µM	4.0	0.5
ANS 3 µM	4	1.2
BSA 10 µM + ANS 3 µM	11	7

CCVJ 10 µM	0.2	0.2
BSA 10 µM + CCVJ 10 µM	0.6	0.7
MB 10 nM	--	0.9
MB 10 nM + Target15-mer 100 nM	0.6	0.9

Table 5.1. Fluorescence lifetime measurements on probe solutions. All values are expressed in nanoseconds (ns) and are calculated according to phasor approach[10].

Molecular interactions are known to be facilitated in confined environments[3]. We observed that extremely high affinity intermolecular interactions such as Streptavidin-Biotin are totally unmodified by confinement, also if τ of the resulting complex, but not of the labelled ligand, is reduced in comparison with bulk solution (**Fig. 5.8**); this being likely explained again by possible effects on the STV structure[28].

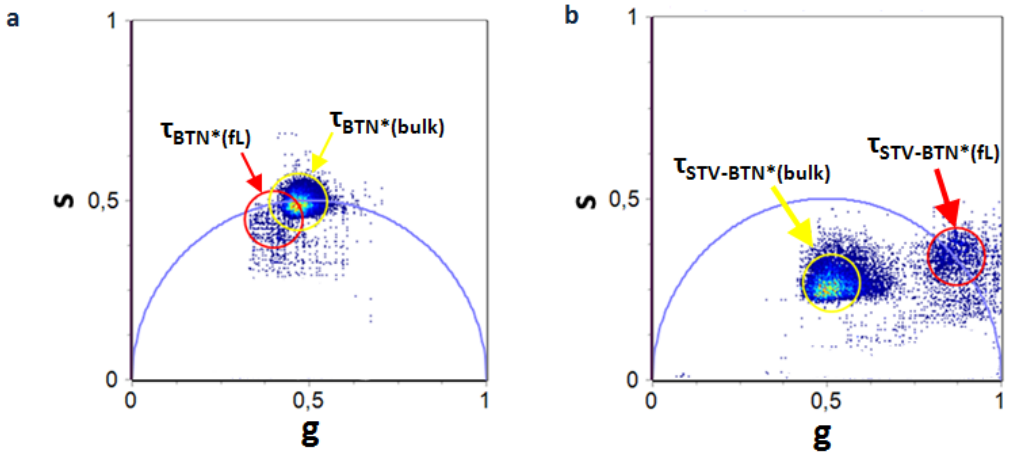

Figure 5.8: Fluorescence lifetimes (**τ**) of fL droplets and corresponding bulk volumes containing (**a**) Atto655-Biotin (BTN*) 4 µM, (**b**) Atto655-BTN (BTN*) 4 µM and Streptavidin (STV) 4 µM.

5.4.2 Molecular machines in confined and crowded environments

We tested synergic effects of confinement and crowding in fL compartments on a DNA molecular beacon (**Fig. 5.9a**) whose fluorescence is triggered by the presence of an input target sequence by a strand displacement mechanism. In absence of target, DNA machine is in OFF state – i.e. it is not fluorescing, since dye (Alexa 555) and quencher (BHQ2) are in close proximity producing FRET.

In presence of target (Target 15-mer), single strand displacement on DNA beacon causes conformational rearrangement which restores fluorescence. Very surprisingly, in comparison to bulk volumes, DNA beacon in OFF state (i.e. in absence of target) showed fluorescence signal and measurable τ (**Fig. 5.9b**). In ON state, DNA beacon showed increase of τ in comparison to bulk (0.9 ns vs 0.6 ns) and an almost10-fold increase of fluorescence signal (**Fig. 5.9b** and **Fig. 5.9c**). From these results, a different Fret Efficiency <E> is calculated between bulk (1) and fL droplets (0.78), (see **Fig. 5.9c**), which can be ascribed to a more elongated DNA conformation in fL.

Finally, signal was switched-on at one order of magnitude lower input target concentration in fL vs. bulk (**Fig. 5.9d** and **Fig. 5.10**).

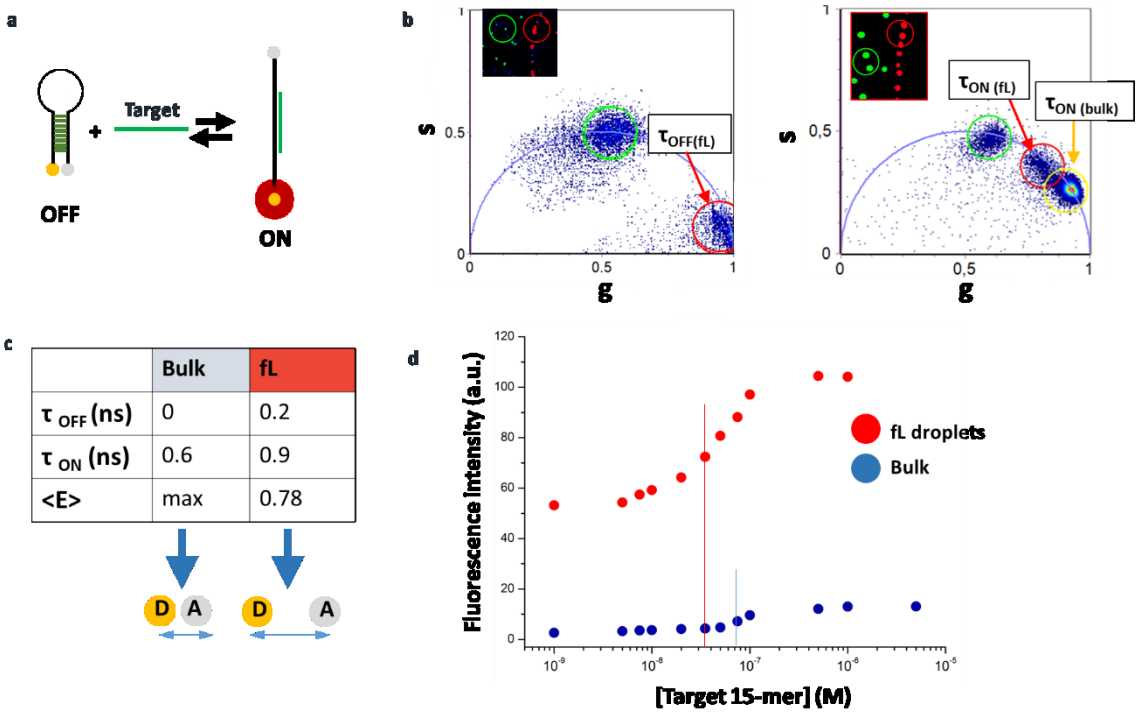

Figure 5.9: Enhanced functionality of DNA Molecular machines. (a.) Switching mechanism of a model DNA machine by action of DNA target sequence. (b.) Phasor plots of DNA machine in OFF (panel at left), and in ON-state (panel at right). As expected, τ increases when DNA machine is in ON-state in fL-scale droplets. (c.) Table comparing τ_{ON}, τ_{OFF}, Fret Efficiency $\langle E \rangle \approx (\tau_{OFF}/\tau_{ON}) - 1$. (d.) Fluorescence intensity plot of DNA machine as a function of DNA target concentration showing approximately 10-fold enhanced switch to ON-state when confined.

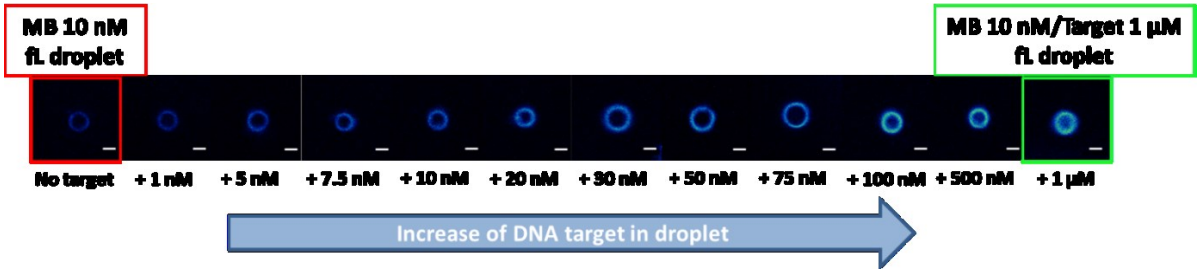

Figure 5.10: Fluorescence confocal images of single fL droplets of DNA molecular beacon (MB 10 nM) at increasing DNA Target15-mer concentration (from 1 nM to 1 µM). Scale bar 2 µm.

Such peculiar behaviour of DNA machine under confinement can likely be ascribed to single strand elongation phenomena which occur in DNA molecules under surface confinement in presence of crowding agents under ψ (polymer and salt induced)-phase elongation/condensation[29] (**Fig. 5.11**).

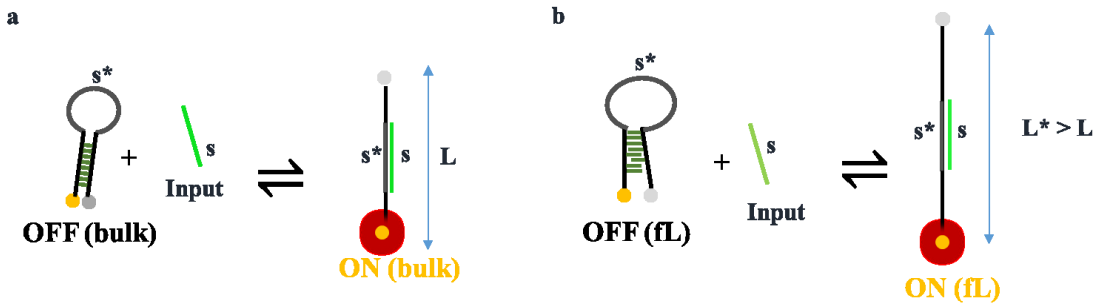

Figure 5.11: DNA machine conformation in a) bulk and b) fL system.

Variation of DNA conformation in confinement is due to anisotropic osmotic pressure between the in PEG-PPG rich interface with oil phase and the drop bulk[30]. As previously reported, interface with oil phase is depleted from DNA molecules since it is mostly occupied by PEG-PPG copolymer. The concentration gradient of PEG-PPG will result in a non-compensated osmotic pressure transverse to the droplet interface. The osmotic pressure is able to keep away DNA from oil interface and concentrates DNA in the adsorbate layer, resulting in an increased molecular density and an increase in the free energy due to intramolecular excluded volume interactions. This finally leads to elongated DNA strand parallel, as demonstrated by coarse grained Brownian dynamics simulations[30]. Conformation elongation of DNA machine causes lower FRET between fluorophore and quencher and also larger molecular scale fluctuations that make τ sensitive to local solution viscosity - in accordance with the Förster–Hoffmann equation[23]. In other words, higher elongation causes higher **τ**, similarly to what happens to elongated chromatin which shows higher **τ** in decondensed regions in cells[31]. According to Brownian-based numerical models[30], elongation of DNA molecules in presence of synergic confinement and crowding effects should bring to 10-15% elongation which is in accord with our data.

The results of this study suggest that the design of aqueous fL droplets by a “spike-like” jetting waveform can lead to the assembly of a unique self-assembled aqueous confinement platform at a water-oil interface in presence of crowding agents that can outperform naturally occurring crowding phenomena in sub-cellular scale compartments. For the first time, molecular self-assembling is carried out in aqueous femtoliter-scale droplets in order to produce synergic effects of confinement and crowding leading to superior functionality of a DNA molecular machine. Our approach could be a step towards fabricating compartments for molecular confinement with tailored properties.

Bibliography

1. Rabe, K. S., Müller, J., Skoupi, M. & Niemeyer, C. M. Cascades in Compartments: En Route to Machine-Assisted Biotechnology. *Angew. Chemie Int. Ed.* **56,** 13574–13589 (2017).
2. Huan-Xiang Zhou,1 Germán Rivas, 2 and Allen P. Minton. Macromolecular Crowding and Confinement: Biochemical, Biophysical, and Potential Physiological Consequences. *Annu. Rev. Biophys.* **37,** 375–397 (2008).
3. Kuchler, A., Yoshimoto, M., Luginbuhl, S., Mavelli, F. & Walde, P. Enzymatic reactions in confined environments. *Nat Nano* **11,** 409–420 (2016).
4. Miyazaki, M., Chiba, M., Eguchi, H., Ohki, T. & Ishiwata, S. Cell-sized spherical confinement induces the spontaneous formation of contractile actomyosin rings in vitro. *Nat Cell Biol* **17,** 480–489 (2015).
5. Hansen, M. M. K. *et al.* Macromolecular crowding creates heterogeneous environments of gene expression in picolitre droplets. *Nat Nano* **11,** 191–197 (2016).
6. Braunschweig, A. B., Huo, F. & Mirkin, C. A. Molecular printing. *Nat Chem* **1,** 353–358 (2009).
7. Park, J.-U. *et al.* High-resolution electrohydrodynamic jet printing. *Nat Mater* **6,** 782–789 (2007).
8. Ferraro, P., Coppola, S., Grilli, S., Paturzo, M. & Vespini, V. Dispensing nano-pico droplets and liquid patterning by pyroelectrodynamic shooting. *Nat Nano* **5,** 429–435 (2010).
9. Grilli, S. *et al.* Active accumulation of very diluted biomolecules by nano-dispensing for easy detection below the femtomolar range. *Nat Commun* **5,** (2014).
10. Stringari, C. *et al.* Phasor approach to fluorescence lifetime microscopy distinguishes different metabolic states of germ cells in a live tissue. *Proc. Natl. Acad. Sci.* **108,** 13582–13587 (2011).
11. Lam, H. Y. G. and X. S. and T. E. and B. K. L. and Y. C. Reduction of droplet volume by controlling actuating waveforms in inkjet printing for micro-pattern formation. *J. Micromechanics Microengineering* **19,** 55010 (2009).
12. James, A. J., Vukasinovic, B., Smith, M. K. & Glezer, A. Vibration-induced drop atomization and bursting. *J. Fluid Mech.* **476,** 1–28 (2003).
13. Zhang, Y., Zhu, B., Liu, Y. & Wittstock, G. Hydrodynamic dispensing and electrical manipulation of attolitre droplets. *Nat. Commun.* **7,** 12424 (2016).
14. Eggers, J. Universal pinching of 3D axisymmetric free-surface flow. *Phys. Rev. Lett.* **71,** 3458–3460 (1993).
15. H.Dong, Carr, W. W. & Morris, J. F. An experimental study of drop-on-demand drop formation. *Phys. Fluids* **18,** 72102 (2006).
16. Arrabito, G. & Pignataro, B. Solution Processed Micro- and Nano-Bioarrays for Multiplexed Biosensing. *Anal. Chem.* **84,** 5450–62 (2012).
17. Symes, M. D. *et al.* Integrated 3D-printed reactionware for chemical synthesis and analysis. *Nat Chem* **4,** 349–354 (2012).
18. Dixon, C., Lamanna, J. & Wheeler, A. R. Printed Microfluidics. *Adv. Funct. Mater.* **27,** n/a-n/a (2017).

19. Arrabito, G. *et al.* Monitoring few molecular binding events in scalable confined aqueous compartments by raster image correlation spectroscopy (CADRICS). *Lab Chip* (2016). doi:10.1039/C6LC01072E

20. Sekitani, T., Noguchi, Y., Zschieschang, U., Klauk, H. & Someya, T. Organic transistors manufactured using inkjet technology with subfemtoliter accuracy. *Proc. Natl. Acad. Sci.* **105,** 4976–4980 (2008).

21. Chang, C.-H. & Franses, E. I. Adsorption dynamics of surfactants at the air/water interface: a critical review of mathematical models, data, and mechanisms. *Colloids Surfaces A Physicochem. Eng. Asp.* **100,** 1–45 (1995).

22. Miller, R. *et al.* Dynamics of protein and mixed protein/surfactant adsorption layers at the water/fluid interface. *Adv. Colloid Interface Sci.* **86,** 39–82 (2000).

23. Berezin, M. Y. & Achilefu, S. Fluorescence Lifetime Measurements and Biological Imaging. *Chem. Rev.* **110,** 2641–2684 (2010).

24. Chen, R. F. & Knutson, J. R. Mechanism of fluorescence concentration quenching of carboxyfluorescein in liposomes: Energy transfer to nonfluorescent dimers. *Anal. Biochem.* **172,** 61–77 (1988).

25. Levitt, J. A. *et al.* Fluorescence Anisotropy of Molecular Rotors. *ChemPhysChem* **12,** 662–672 (2011).

26. Hawe, A., Sutter, M. & Jiskoot, W. Extrinsic Fluorescent Dyes as Tools for Protein Characterization. *Pharm. Res.* **25,** 1487–1499 (2008).

27. Iio, T., Itakura, M., Takahashi, S. & Sawada, S. 9-(Dicyanovinyl) Julolidine Binding to Bovine Brain Calmodulin. *J. Biochem.* **109,** 499–502 (1991).

28. Shipovskov, S. *et al.* Water-in-Oil Micro-Emulsion Enhances the Secondary Structure of a Protein by Confinement. *ChemPhysChem* **13,** 3179–3184 (2012).

29. Zhang, C., Shao, P. G., van Kan, J. A. & van der Maarel, J. R. C. Macromolecular crowding induced elongation and compaction of single DNA molecules confined in a nanochannel. *Proc. Natl. Acad. Sci.* **106,** 16651–16656 (2009).

30. Jones, J. J., van der Maarel, J. R. C. & Doyle, P. S. Effect of Nanochannel Geometry on DNA Structure in the Presence of Macromolecular Crowding Agent. *Nano Lett.* **11,** 5047–5053 (2011).

31. Spagnol, S. T. & Dahl, K. N. Spatially Resolved Quantification of Chromatin Condensation through Differential Local Rheology in Cell Nuclei Fluorescence Lifetime Imaging. *PLoS One* **11,** e0146244 (2016).

6 Dip Pen Nanolithography of oligonucleotides on glass and flexible substrate

This chapter reports a general methodology to dispense and anchor single-stranded oligonucleotides by Dip Pen Nanolithography (DPN) on two different solid surfaces, glass and nylon, in form of ordered arrays[1,2].

The work starts by the cooperation with the prof. Alessandro Desideri of University of Roma Tor Vergata, which recently launched a research project on the creation of a diagnostic kit to determine whether a given organism is subject to malaria, based on studies on the role of the parasite *Plasmodium* for the detection of malaria, previously published in collaboration with the Danish research team led by prof. Birgitta Knudsen of the University of Aarhus in Denmark[3,4].

The research was conducted on the DNA sequences, designed in the laboratory by the research group of prof. Knudsen (University of Aarhus). Sequences of single-stranded DNA were hybridized in our laboratories through the techniques of microarrays.

We optimized oligonucleotides printing conditions on nylon substrate as follows. DPN operation needs ultralow amounts of DNA (as low as 0.5 µL, 10 - 1 µM concentration) for printing thousands of spots in a single run so reducing material consumption[5]. The printed oligonucleotides were hybridized with a fluorescence-labelled complementary probe to allow the detection of the signal and quantify DNA after DPN deposition (**Fig. 6.1**).

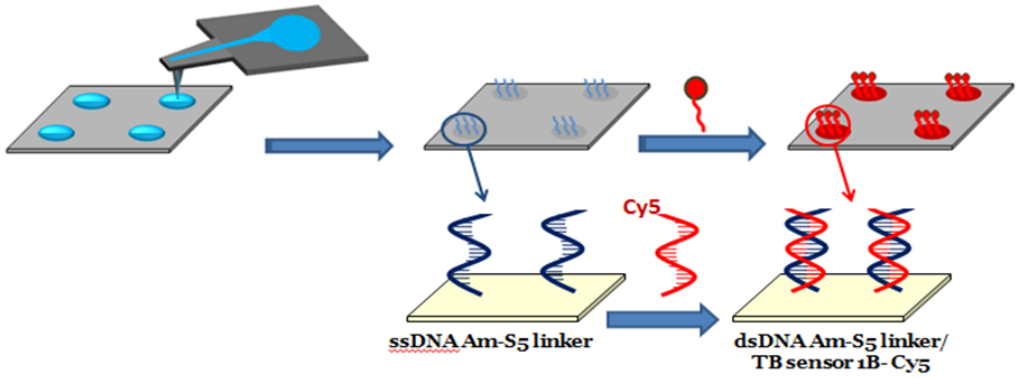

Figure 6.1: Schematic representation to print single-strand DNA sequence on solid support and hybridize to a complementary DNA sequence.

6.1 Materials and Methods

6.1.1 DNA oligonucleotides sequences

Am-S5 linker

Sequence (5' to 3'): [AmC6F]AGA AAA ATC CAG ACG CTC ACT GAG CGG AAG CTT CAG

TB sensor 1B-Cy5

Sequence (5' to 3'): [Cyanine5]CAG TGA GCG TCT GGC TGA AGC TTC CGC T

Am-S5 linker sequence has an amino group at the 5'(Am) for the covalent anchoring to surfaces functionalized with epoxy groups or aldehyde.

TB sensor 1B-Cy5 sequence is the complementary sequence of Am-S5 linker labelled with the fluorescent dye Cyanine5 (Cy5). The traits underlined in both chains are complementary regions that will bind during the hybridization reaction.

Oligonucleotide sequences were designed at the Birgitta Knudsen group (University of Aarhus, Denmark) and purchased at Sigma-Aldrich.

6.1.2 Purification and characterization of sequences

Before depositing, accurate DNA sequences analysis was performed to purify and measure the exact concentration when dissolved in aqueous solution.

First, all sequences were purified by means of a process of exclusion chromatography which involves the use of columns NAP5/NAP10 (GE Healthcare) to trap any impurities present in the DNA sample (typically organic compounds and metal ions). The stationary phase of the NAP columns is a Sephadex^{TM} resin gel, the mobile phase consists of Millipore H_2O.

Initially, the oligonucleotide is diluted in 500 µL of water. The sample is transferred to NAP 5 and eluted with 1000 µL of water. NAP 5 and NAP 10 are placed over each other so that the liquid released from the NAP column 5 is collected within NAP 10. Two further eluations are performed with 750 µL of water each. The final sample of 1500 µL is treated with a centrifugal micro-heater NB 503 CIR Micro-cenvac, at 5000 rpm for 8 hours at 35 °C, to evaporate the collected water during the chromatography process, retaining only the sample of purified DNA. Once the mobile phase solvent was evaporated the resulting DNA pellet was solubilized in 5 µL of 0.1 TE buffer.

The TE buffer is initially prepared at 1M concentration by mixing 1 ml of tris-HCl 1M at pH 8 with 0.2 ml of EDTA at 0.5 M (Ethylenedioaminotetraacetic acid > 98%, Fluka analitical).

The tris-HCl solution was previously prepared by reacting Tris (Tris(hydroxymethyl)aminomethane

≥ 99.8% Sigma Aldrich) with Hydrochloric acid (HCl 12 M to 37%, Carlo Erba). The desired pH value is obtained with HCl addition.

Finally, a sample of buffer solution is diluted 10 times to obtain a 0.1 M TE buffer.

After the purification procedure, the concentration of oligonucleotides is determined through absorbance measurements, with a UV-vis spectrophotometer (Specord S600 of the Analytic Jena), at 260 nm, i.e. the value in which the nitrogenous bases of the oligonucleotide sequence absorb. For these analysis, 1 µL of the purified DNA solution was diluted with water until 1 ml to reach the optimal concentration range for the measure.

The molar extinction coefficient ε for Am-S5 linker sequence is 359.7 $mM^{-1}\cdot cm^{-1}$; for TB sensor 1B-Cy5 is equal to 254.5 $mM^{-1}\cdot cm^{-1}$.

In addition, for the TB sensor 1B-Cy5 sequence a fluorimetric characterization was performed with

a Horiba Jobin Yvon spectrophotometer (FLUOROMAX-1), thanks to the presence of fluorophore Cyanine 5. The excitation and emission values, 650 nm and 670 nm respectively, has been selected. The fluorescence spectrum exhibited an emission peak at 670 nm confirming the presence of fluorophore in the molecule. For quantitative determination, a UV spectrum was obtained by measuring the absorbance of the nitrogenous bases at 260 nm. The results obtained will be shown and discussed in the next section.

6.1.3 Preparation of printing surface

Two different surfaces were used for microarray preparation: epoxy-functionalized glass on which the oligonucleotide is covalently bonded by the amine group at 5' of the sequence, and nylon surfaces in which deposited DNA is immobilized for electrostatic interactions.

Optical microscopy slides (Excell, ISO 8037 / I, 26 mm x 76.1 mm, 1.2 mm thick) are used as glass surfaces. First washing with absolute ethanol (98%, Fluka Analitical) is carried out to remove impurities and organic residues. In order to make the surface hydrophilic, an ozone cleaning process is performed (UV Ozone Cleaner - ProCleanerTM, Bioforce Nanosciences) for 30 minutes. After the cleaning process, the slide is treated in a Petri dish for 5 hours at room temperature with a 90% ethanol and 10% APTES solution ((3-Aminopropyl)triethoxysilane 99% Sigma Aldrich); (**Fig. 6.2 a)**). So the ammino-silanized slide is washed with acetone (99%, Fisher) and then ethanol, dried for 15 minutes at 110 °C and stored at -20 °C overnight. Subsequently, two slides are contacted with each other (sandwich method) using a PBAG solution (poly(Bisphenol A-co-epichlorohydrin), glycidyl end-cappen, Sigma Aldrich**, Fig. 6.2 b)**) in acetone (1:1 ratio) and stored at room temperature for one night. Finally, the two slides are separated, washed with acetone and used for the printing process[6]. In **figure 6.2 c)** the schematic sequence of functionalization of glass surface procedure is shown.

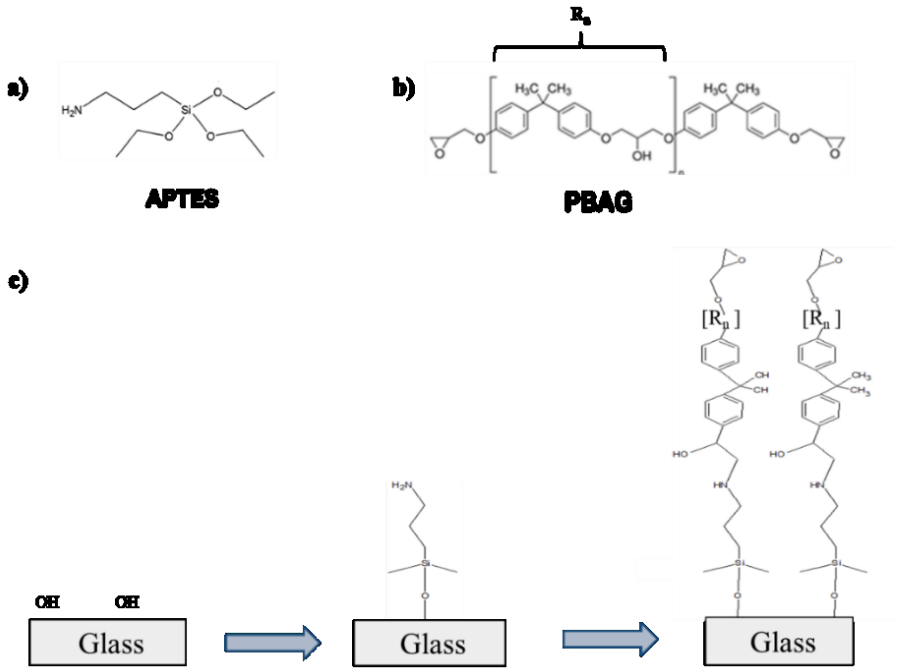

Figure 6.2: a) APTES (3-Aminopropyl)tryethoxysilane; b) poly(Bisphenol A-co-epichlorohydrin), glycidyl end-cappen; c) Schematic representation of glass functionalization procedure.

For deposition on nylon surfaces, nylon sheets (Amersham Hybond-N+ Ge Healthcare Lifesciences, Hyblot) were used. These sheets have a positive charge and are used for Southern Blot techniques in which DNA sequences, separated by electrophoretic methods, are transferred for qualitative and quantitative analysis. The presence of positive charge allows electrostatic interaction with DNA sequences. Since nylon support is ready for use, no preliminary operation is required. After the deposition of DNA sequence, surface UV crosslinking is carried out using UVC 500 Hoefer Ultraviolet Crosslinker.

6.1.4 DNA oligonucleotides deposition

The deposition of single-stranded oligonucleotide sequences was carried out by the Dip Pen Nanolithography (Nano eNabler™ Molecular Printing System of BioForce Nanoscience, **Fig. 6.3**), a contact printing method based on the Atomic Force Microscopy to dispense femtoliter scale drops of solution on solid supports with a microfluidic deposition system. The spot size on micrometer and nanometer scales heavily depends on factors such as time of contact between tip and surface, humidity, and viscosity of molecular ink.

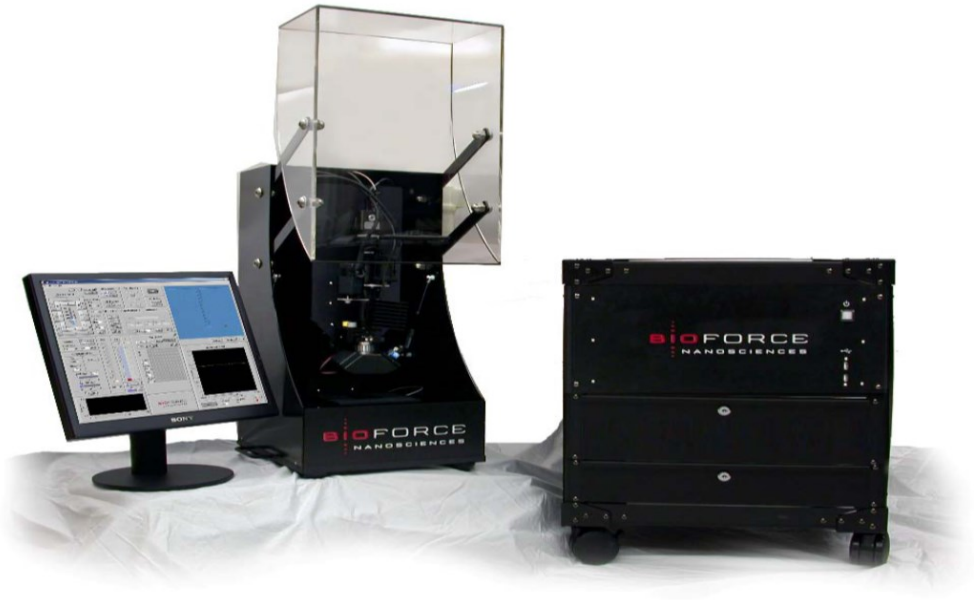

Figure 6.3: Nano eNabler^{TM} Molecular Printing System of BioForce Nanoscience.

A small amount of ink, is placed on a reservoir, it flows by capillary effect within a microchannel and when the tip is in contact with the receiving surface is deposited (**Fig. 6.4**). The microfluidic system described is called "Surface Patterning Tool", SPT. For the experiments have been used SPT microchannels with a width of 30 microns.

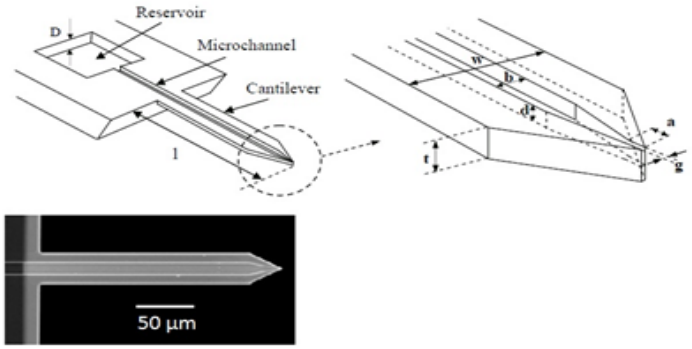

Figure 6.4: Surface Patterning Tool.

On the tip of the SPT, (which has been previously treated with ozone for 30 minutes to make its surface hydrophilic), an ink containing the DNA sample with additives needed to create the optimum hydration and viscosity conditions for printing is loaded.

5 µL of solution containing AmS5linker 100 µM were prepared, with the addition of PEG1000 (Sigma Aldrich) and glycerol (99.5% Sigma Aldrich) in three different PEG1000/glycerol ratios as summarized in the following table:

Ink 1	***Ink 2***	***Ink 3***
5% PEG 1000	5% PEG 1000	5%PEG 1000

10% Glycerol	30% Glycerol	50% Glycerol
0.05 TE buffer	0.05 TE buffer	0.05 TE buffer
DNA 100µM	DNA 100µM	DNA 100µM
H_2O	H_2O	H_2O

Table 6.1: Inks components.

For each type of ink oligo-spots microarray have been made using different contact times, from 0.1 to 10 seconds, and different values of relative humidity, 50%, 60% and 70%.

The systematic study to determine the optimal printing conditions for the realization of spots on glass is discussed in the next chapter. When the printing process is finished, the glass surface is stored at room temperature overnight.

Regarding the deposition of AmS5linker on nylon, solutions containing different concentrations of DNA (between 0-100 µM) were prepared by adding PEG1000 (5%) and glycerol (10%-30%) to determine the effect of viscosity and concentration on the efficiency of DNA deposition.

6.1.5 Hybridization protocols

The hybridization reactions required the following three buffers:

- MESTBS: prepared by mixing 20 mM tris-HCl, 150 mM NaCl (98%, Sigma Aldrich), 4.5% milk powder (which reduces non-specific interactions; Fluka Analitical), 5 mM EDTA (used to chelate the metals necessary for the nucleases activity), 0.2% NaN_3 (sodium azide being a preservative avoids degradation phenomena; 99%, Sigma Aldrich) and finally 1mg/ml of DNA herring sperm (standard used to significantly reduce non-specific interactions; Sigma Aldrich). The buffer is brought to pH 7.35 by using the pH meter.
- TETBS: prepared by mixing 20 mM tris-HCl, 150 mM NaCl, 5 mM EDTA and 0.05% Tween-20 (to significantly reduce non-specific interactions; Sigma Aldrich). Finally, the buffer is brought to pH 7.5.
- DNA hybridization spotting buffer: prepared by mixing the TE buffer with 300 mM NaCl and bringing the pH to 7.5.

The glass slide is washed for 30 minutes with the MESTBS buffer and, for another 15 minutes, with the TETBS buffer. 50 µL of TB sensor sequence solution (100 nM in TETBS buffer) is released on the Am-S5 linker microarrays. The hybridization reaction is carried out at room temperature within a humidity chamber for about 1 hour. Subsequently, the surface is washed with PBS (phosphate buffer solution, pH 7.4).

As for hybridization on nylon, a protocol suggested by the Danish research team was used. Before hybridization, washings were performed with the MESTBS and TETBS buffers. 50µL of 100 nM TB sensor solution dissolved in the DNA hybridization buffer are placed where the arrays were

printed. The hybridization reaction is carried out for 1 hour at 50 °C within the centrifugal micro-heater chamber. Subsequently, the sample is washed with the same hybridization buffer.

In both cases, microarrays are observed either through the DPN camera and with a ChemiDoc™ MP Imaging microarray scanner (Bio-Rad), by energizing the Cy5 probe in the red 695-655nm cpn filter "Red epi filter". Array images after hybridization are exported in .tiff format and analyzed by the imageJ software (a program that allows you to measure radius, perimeter and area by pixel counting).

6.2 Results and Discussion

6.2.1 Oligonucleotides concentration

The concentration of the oligonucleotide is determined through absorbance measurements, obtaining an absorption peak at 260 nm, value in which there is absorption by the nitrogen bases of the oligonucleotide. For the TB Sensor 1B-Cy5 sequence is observed another peak at around 650 nm indicating the fluorophore absorption. For Am-S5 linker DNA sequences a concentration of 380 µM is obtained; for TB sensor 1B the concentration of solution is 300 µM. The UV-vis spectra are reported in **figure 6.5**.

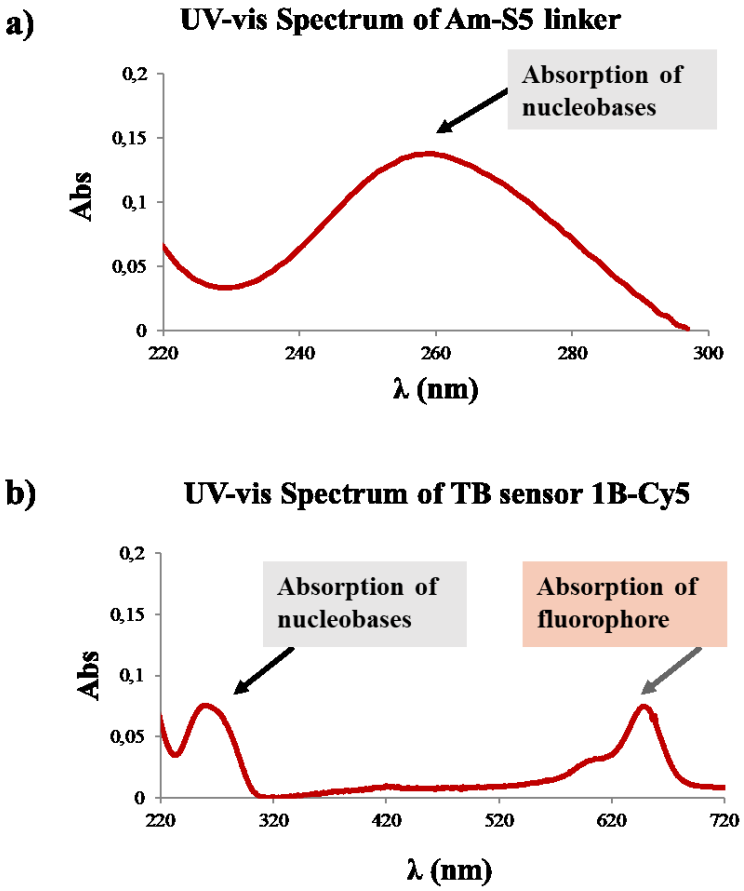

Figure 6.5: UV-vis spectra of a) Am-S5 linker and b) TB sensor 1B-Cy5.

6.2.2 Systematic study for the realization of oligo-spots on functionalized glass surfaces

Using the three formulations previously indicated with relative humidity of 50%, 60% and 70%, and contact times of 0.1 s, 1 s, 3 s, 5 s, 10 s was conducted a systematic study for the realization of spots on glass to determine the optimal printing conditions.

Each of the following images (captured with the DPN's high resolution camera) shows spots of Am-S5 linker spaced 50 μm, deposited at different contact times and different humidity conditions.

Ink 5/10 (5% PEG 1000, 10% glycerol)

The deposition of the ink made with 5% PEG1000 and 10% glycerol (Ink 5/10), at different contact times, from 0.1 to 10 seconds, and relative humidity of 50%, 60% and 70%, lead to the following results:

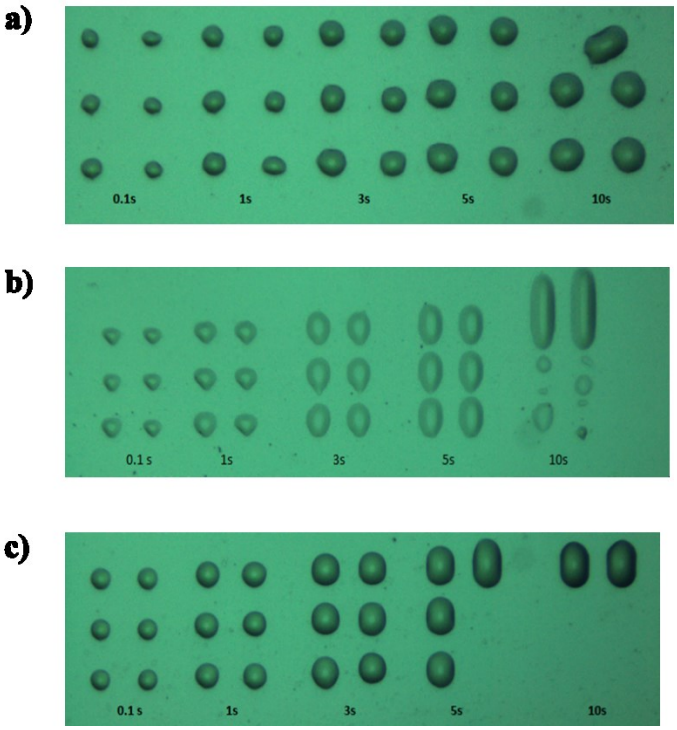

Figure 6.6: Spots deposition of Ink 5/10 at a) 50% RH, b) 60% RH, c) 70% RH, at different contact times.

Under 50% humidity conditions (**Fig. 6.6 a)**), the spots have a fairly regular and circular shape. At 10s the amount of liquid released by the tip of the DPN is such that there is coalescence and thus loss of resolution. At 60% RH (**Fig. 6.6 b)**) none of the spots has a regular shape; most likely this is due to irregularities during deposition. At 70% RH (**Fig. 6.6 c)**) the spots are fairly regular up to a 3s contact time. Different spots at 5s and 10s are not visible for the same coalescence phenomenon seen above for high contact times.

The table shows the mean diameters measured for each contact time and each humidity condition, in addition to its standard deviations and variance coefficients (expressed in percentage terms).

	RH 50%				RH 60%				RH 70%		
Time (s)	Diam.(µm)	St. Dev.	CV		Diam.(µm)	St.Dev.	CV		Diam.(µm)	St.Dev.	CV
0.1	13,631	0,352	2,6%		-	-	-		19,594	0,709	3,6%
1	16,105	0,947	5,8%		-	-	-		24,324	0,375	1,5%
3	19,560	0,042	4,2%		-	-	-		28,603	0,97	3,4%
5	22,625	0,033	3,3%		-	-	-		31,254	0,716	2,3%
10	26,295	0,017	1,7%		-	-	-		-	-	-

Table 6.2: Spots data for Ink 5/10.

No data are obtained for spots realize with a humidity of 60% and for spots at 10 s as a contact time at 70% humidity. Following graph shows the linear correlation between the average diameters measured for each contact time, on the ordinate, and the square root of the contact time, along the abscissa, in the condition of relative humidity of 50% and 70%.

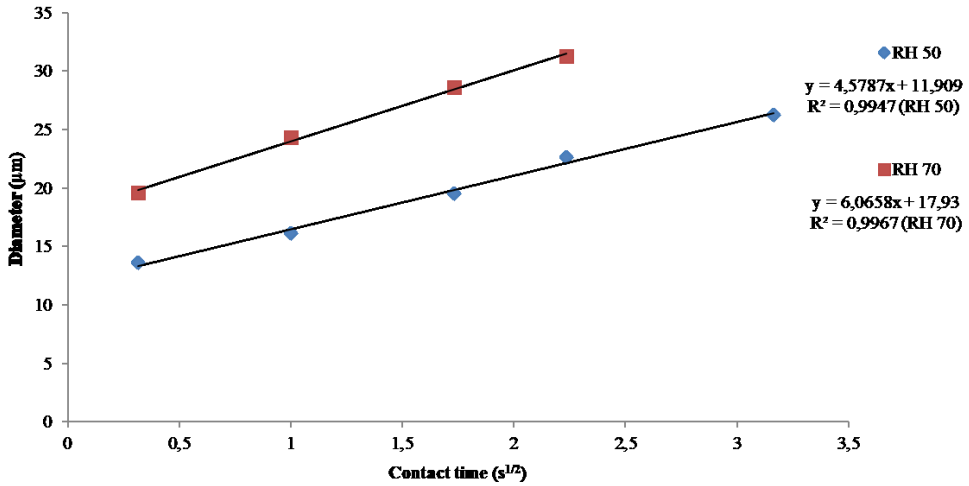

Figure 6.7: Linear contact time-diameter correlation for Ink 5/10. The results are shown at 50% and 70% relative humidity.

So, the ink 5/10 forms fairly regular spots both under high viscosity conditions, RH 50%, and low viscosity, RH 70%. As the humidity increases, the average diameter of the spot is increased, due to the fact that higher humidity (i.e. the greater amount of water present in the deposition environment) leads to a decrease in the viscosity of the deposited liquid, thus to a greater fluidity and greater size spots. A better response is obtained at 50% of humidity, despite a minor correlation, since it cannot print spots at high contact times.

Ink 5/30 (5% PEG 1000, 30% glycerol)

For the ink made with 5% PEG 1000 and 30% glycerol (Ink 5/30) the following arrays were printed:

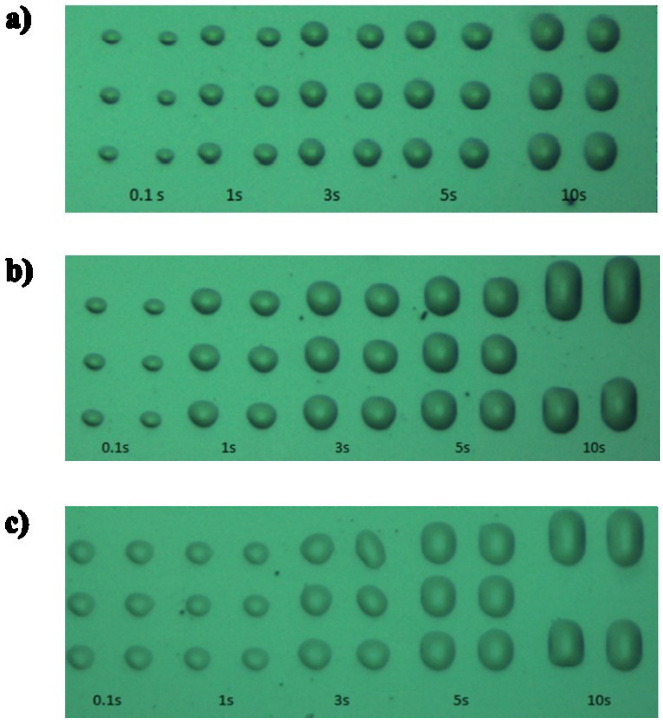

Figure 6.8: Spots deposition of Ink 5/30 at a) 50% RH, b) 60% RH, c) 70% RH, at different contact times.

At 50% RH (**Fig. 6.8 a)**), spots with a circular shape are obtained at both low and high contact times. At 60% RH (**Fig. 6.8 b)**), spots with an optimal shape are obtained up to a 5s contact time, at 10 s the spot has an elongated shape due to the diffusion of the fluid released from the tip of the DPN. The fluid tends to spread along the area where the cantilever is present due to its remarkable hydrophilicity which increases the adhesion forces with the fluid. At 70% RH (**Fig. 6.8 c)**) the spots have irregular shapes at 5s and 10s for the same reason.

Table 6.3 shows the values of the diameters measured for each set of spots at different contact times and different humidity. The graph in **figure 6.9** shows the linear correlation between spot size and contact time.

	RH 50%				RH 60%				RH 70%		
Time (s)	Diam.(µm)	St. Dev.	CV		Diam.(µm)	St.Dev.	CV		Diam.(µm)	St.Dev.	CV
0.1	12,739	0,881	6,9%		17,821	0,393	2,2%		22,052	0,902	4,1%
1	15,060	0,604	4%		24,568	0,53	2,1%		20.897	0.479	2.2%
3	20,285	0,998	4,9%		28,518	0,244	0,8%		27,333	0,716	2,6%
5	22,580	0,854	3,7%		30,267	0,847	2,8%		-	-	-
10	28,440	1,311	4,6%		-	-	-		-	-	-

Table 6.3: Spots data for Ink 5/30.

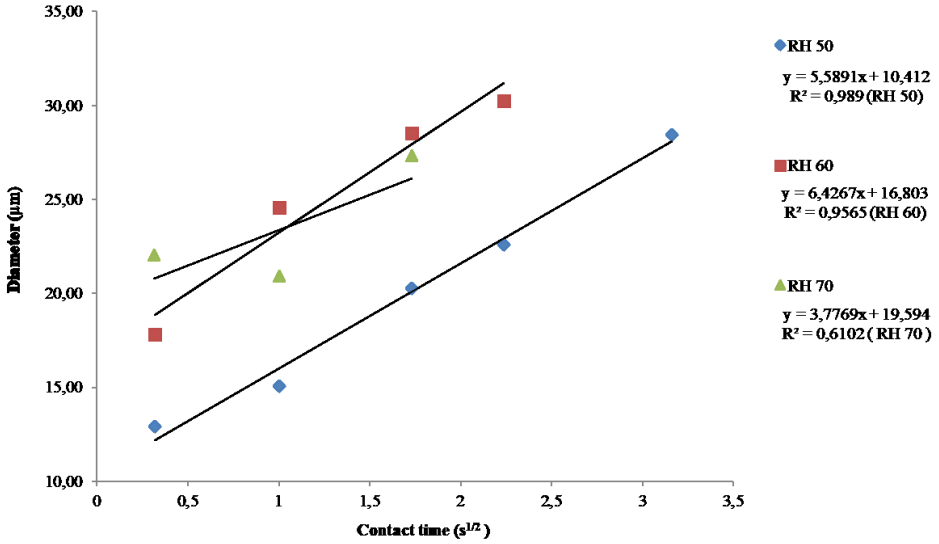

Figure 6.9: Linear contact time-diameter correlation for Ink 5/30. The results are shown at 50%, 60% and 70% relative humidity.

Regarding spot printing conditions at 50% and 60% of relative humidity, good correlations are obtained. At 70% RH, however, there is no good correlation, due to an irregularity observed in spots deposited at 1s contact time. So, the lowest humidity RH 50% leads to spots with more regular size and therefore is preferable to the deposition than the higher humidity.

Ink 5/50 (5% PEG 1000, 50% glycerol)

Finally, the ink prepared with PEG1000 5% and glycerol 50% (Ink 5/50) are analyzed. The spots obtained at RH 50, RH 60 and RH 70 are as follows:

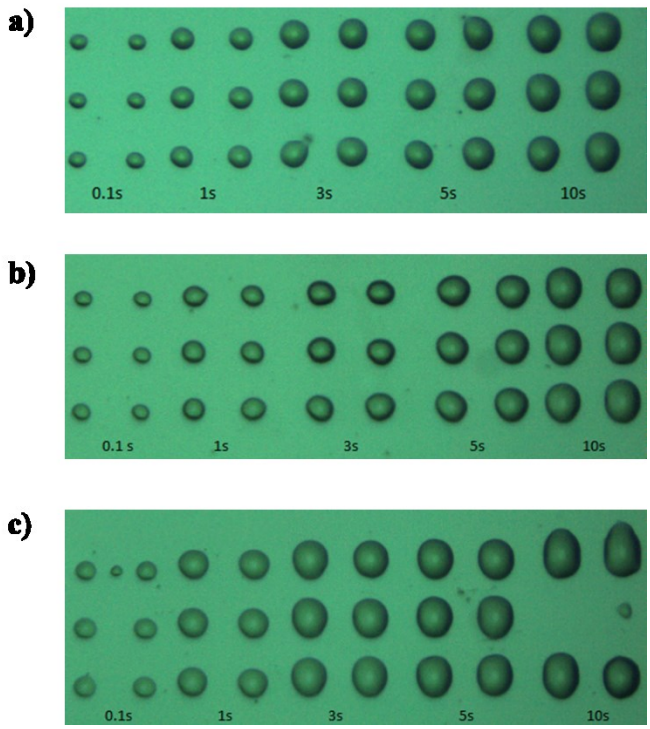

Figure 6.10: Spots deposition of Ink 5/50 at a) 50% RH, b) 60% RH, c) 70% RH, at different contact times.

Spots observation shows that deposited spots have a fairly regular shape at all humidity printing conditions (**Fig. 6.10**). In particular, at 70% RH it is observed that spots, starting at 3s contact time, seem to reach almost constant size, as will be shown later by the graph of linear correlation. Additionally, at 70% RH we observe the same irregular shape for 10s contact time. The measured data for each set of spots and the respective correlation lines are shown in **table 6.4** and **figure 6.11**.

	RH 50%				RH 60%				RH 70%		
Time (s)	Diam.(μm)	St. Dev.	CV		Diam.(μm)	St.Dev.	CV		Diam.(μm)	St.Dev.	CV
0.1	13,648	0,636	4,6%		12,964	0,267	2%		16,772	0,893	5,3%
1	18,297	0,715	3,9%		16,997	1,013	5,9%		24,043	0,483	2%
3	22,587	1,546	6,8%		21,19	1,122	5,2%		29,297	0,451	1,5%
5	24,457	1,772	7,2%		26,146	0,774	2,9%		30.412	0,523	1,7%
10	28,624	0,457	1,6%		29,377	0,373	1,2%		-	-	-

Table 6.4: Spots data for Ink 5/50.

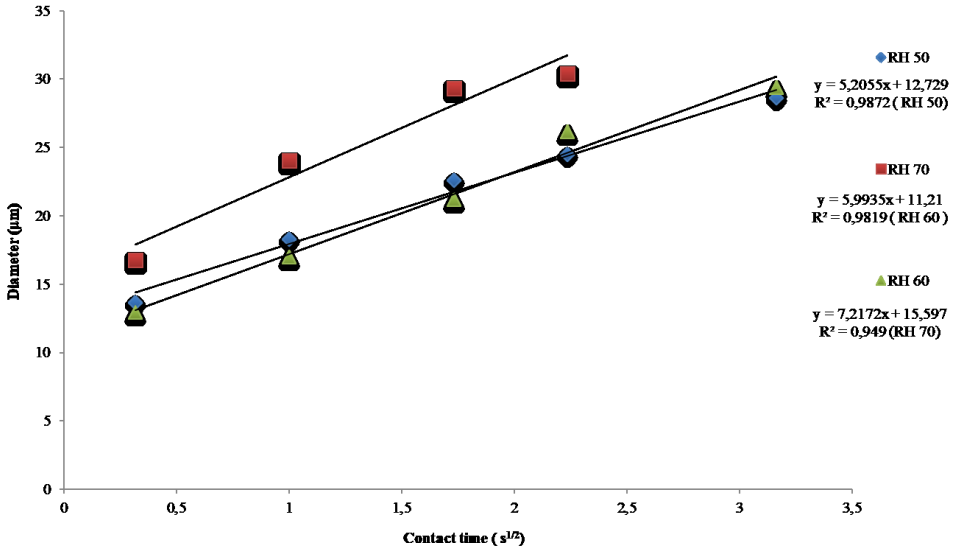

Figure 6.11: Linear contact time-diameter correlation for Ink 5/50. The results are shown at 50%, 60% and 70% relative humidity.

As the humidity increases, the fluid viscosity decreases and hence the size of the spot will tend to increase. The straight lines obtained at 50% and 60% RH tend to intersect, meaning that there are contact times in which the spot obtained at 60% will be similar to that obtained at 50%. Instead for 70% RH it is shown that the size of the spot reaches a plateau at high contact times (3s).

From the analysis at different printing condition it can be concluded that all the three formulations allow to deposit drops of diameters between 10 and 30 µm containing an oligonucleotide sequence in aqueous solution in presence of glycerol and PEG1000. The highest concentration of glycerol (50%) leads to spot with often irregular shape at all humidity condition. Concentrations of glycerol of 10% and 30% lead to more circular and regular spots, (except for 60% RH with 10% glycerol and 70% RH with 30% glycerol), with a good correlation between diameter of spot and square root of contact time. Coalescence between the spots is observed at high contact times for almost all inks. Overall, the best results are observed at 50% and 60% of relative humidity, while at 70% RH, the amount of fluid deposited by SPT is excessive leading to coalescence between adjacent spots and complete loss of resolution and reproducibility. At high humidity, the diameter of the spot reaches a plateau at high contact times (3s), because the fluid transport is mainly governed by the surface tension than the viscosity, as the surface tension tends to slightly reduce the spot enlargement[2]. It is important to note that high concentrations of glycerol, and hence greater drop viscosity, are known to lead to a decrease in the amount of DNA that would covalently bond to the glass surface due to the higher viscosity of the oligonucleotide solution.

On the basis of these data the formulation 5/30 is chosen as a useful compromise between spot morphology and the minimum amount of glycerol required, at relative humidity equal of 50% and lower contact times (0.1 to 3 seconds) which allow to obtain regular spot with a good morphology.

6.2.3 Hybridization reaction on glass

In order to proceed with the hybridization reaction, a 10x10 matrix of Am-S5 linker 100 uM spots spacing 500 μm is fabricated, employing the ink 5/30 at 50% RH and using a contact time of 3s. After treatment with MESTBS and TETBS blocking buffers, the single-strand DNA was hybridized with a fluoro-labelled complementary sequence TB sensor 1B Cy5 100 nM. The hybridization reaction is conducted at room temperature in a humid chamber for about an hour. Subsequently, the surface is washed with PBS buffer.

The observation of the hybridization result is carried out with a microarray scanner (**Fig. 6.12**).

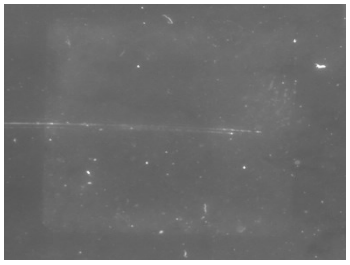

Figure 6.12: Hybridization reaction on glass surface.

The signal detection systems for DNA deposited on glass revealed no presence of spots, indicating a possible failure of the hybridization.

Possible reasons of failure of the experiment may be:

- failure in the DNA link to the surface;
- non-specific binding of the Cy5 labelled DNA on the epoxy surface;
- poor sensitivity of the instrument to reveal a hybridization signal coming from a monolayer of DNA double-strand (corresponding to about 106 molecules for a spot of 40 μm in diameter).

6.2.4 Spot fabrication and hybridization on nylon substrate

We have shown the possibility to efficiently deposit oligonucleotides by Dip Pen Nanolithography (DPN) onto glass surfaces. We have also deposited oligonucleotides on nylon substrate for the fabrication of biochips on flexible supports with the possibility to easily degradate after use. The immobilization of the DNA strand within the nylon matrix is electrostatic and will occur between the positive charge of the nylon and the negative charge given by the phosphate groups present in the DNA. In addition, by exposing the nylon membrane having spots of DNA under UV light, DNA strands will be covalently immobilized within the matrix of nylon. Since nylon is a polymeric material, made of fibers, the amount of DNA that can be immobilized in the nylon is greater than that which is deposited on glass.

Initially, it was necessary to optimize the formulation for depositing the oligonucleotides by means of DPN on the nylon surface. Solutions were prepared containing AmS5 linker at different

concentrations, from 0 to 100 uM with addition of PEG1000 (5%) and glycerol (10% -30%). Surprisingly, the presence of PEG does not allow any deposition of DNA; the solution present in the SPT is not released on the nylon surface even at high contact times (> 20 s). Conversely, a less viscous formulation containing only glycerol (10% to 30%) in millipore water allows depositing the oligonucleotides. Humidity is very important. At 50% RH the spots release is possible, but difficult and only for long contact time with the surface. At higher humidity (70%), the release of the spot is easier with a less pressure from the SPT needed. This can be explained by the fact that the release of the spot on these support is basically driven by electrostatic interactions and relatively less by diffusion or surface tension. Fluid viscosity plays an important role: the increase in humidity and consequently the fluidity of the oligonucleotide solution greatly improves the efficiency of the deposition. The filament of AmS5 linker is deposited in microarray format at various concentrations (0.1 µM, 1 µM, 10 µM, and 100 µM), and crosslinking is performed by UV radiation to fix the DNA on the surface. The efficient deposition is obtained at 10-1 µM oligonucleotide concentrations, 70% relative humidity and 30% glycerol, with circular spots of diameter in the range of 30 - 60 microns in function of the dwell time (from 1 to 20 seconds), (**Fig. 6.13**).

The size of the spots on the nylon surface was approximately determined through an optical characterization with the ImageJ software. For the low contact times the spot diameter dimension is about 35 µm, whereas for high contact times the diameter shows a value between 50-60 µm.

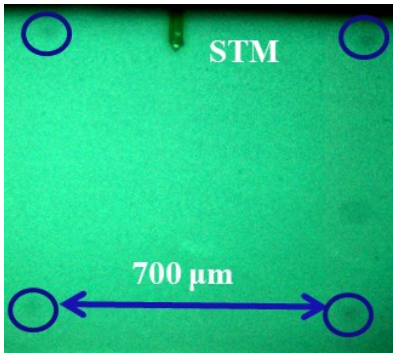

Figure 6.13: Optical image of four AmS5 linker spots (10 µM) deposited on nylon at 70% RH and contact time of 20 s. The spots are spaced 700 µm. Within the rectangle the SPT system is reported.

Following the appropriate treatment with MESTBS and TETBS buffers, a TB sensor 1B-Cy5 solution (100 nM) in DNA hybridization buffer is prepared and transferred on each nylon sheet (80 µL). The hybridization is conducted for 1 hour at 50 °C. Subsequently, the sample is washed with the same hybridization buffer. The signal detection is carried out using a microarray scanner by exciting the probe Cy5 in the range 695-655 nm (**Fig. 6.14**).

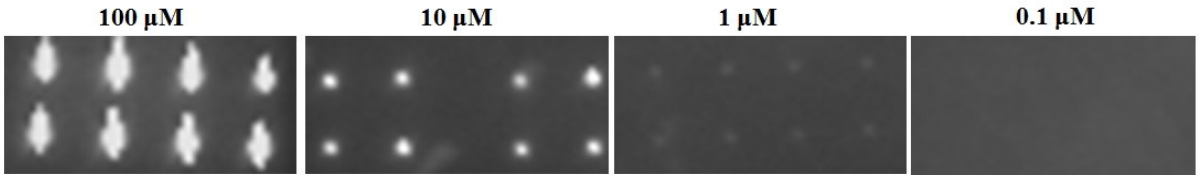

Fig. 6.14: Signal detection of Am-S5 linker spots, at different concentration, on nylon substrate.

Double-strand DNA are visible from AmS5 linker concentrations greater than 1 µM. The deposition at 100 µM leads to spots of irregular shape, probably due to uncontrolled fluid diffusion from SPT following deposition. The average intensity per spot is approximately 31000 ± 3060 (after background subtraction). Spots of optimum shape are obtained at 10 µM and 1 µM (although not clearly visible, a circular shape can be observed). In the latter case, an average intensity of 1070 ± 791 was obtained. At the 10 µM concentration regular and circular spots are obtained. For this case, spots with different contact times (1s - 20s) were also made. The spot intensity increases in diameter according to the contact time, following a linear trend (R^2 = 0.98957, shown in **figure 6.15**), proving that an increased amount of AmS5 linker is deposited for greater contact times. The background value -16062.1 ± 391.5 is subtracted to the DNA spots intensity values.

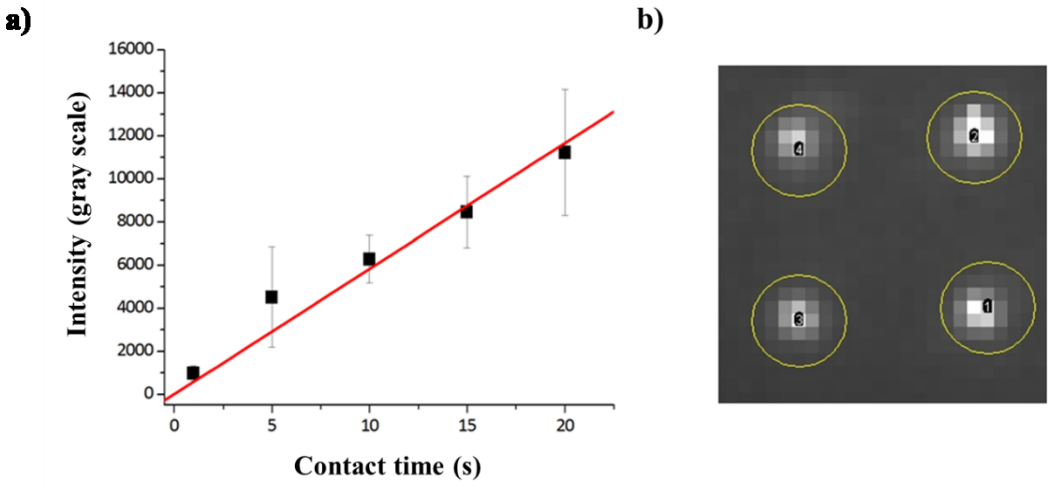

Figure 6.15: a) Average intensity signal (reported as the spot intensity on gray scale) according to the contact time for the 10 µM Am-S5 linker deposition. B) image from ImageJ software showing spots after hybridization (20s contact time).

The future step of the work will be the modification of biochips to detect the Malaria-causing Plasmodium parasites through studies on Plasmodium topoisomerase I activity onto nylon substrates for the diagnostic chips fabrication.

So, in conclusion, flexible supports such as nylon allow the fabrication of low-cost and cheap biochips, and are potentially ideal for the creation of systems disposable in the "Point-of-Care" diagnosis.

Bibliography

1. Martinez, A. W., Phillips, S. T., Whitesides, G. M. & Carrilho, E. Diagnostics for the Developing World: Microfluidic Paper-Based Analytical Devices. *Anal. Chem.* **82,** 3–10 (2010).
2. Arrabito, G. *et al.* Biochips for Cell Biology by Combined Dip-Pen Nanolithography and DNA-Directed Protein Immobilization. *Small* **9,** 4243–4249 (2013).
3. Juul, S. *et al.* Droplet Microfluidics Platform for Highly Sensitive and Quantitative Detection of Malaria-Causing Plasmodium Parasites Based on Enzyme Activity Measurement. *ACS Nano* **6,** 10676–10683 (2012).
4. Zuccaro, L. *et al.* Rolling circle amplification-based detection of human topoisomerase I activity on magnetic beads. *Anal. Biochem.* **451,** 42–44 (2014).
5. Arrabito, G. & Pignataro, B. Solution Processed Micro- and Nano-Bioarrays for Multiplexed Biosensing. *Anal. Chem.* **84,** 5450–62 (2012).
6. Arrabito, G. & Pignataro, B. Inkjet printing methodologies for drug screening. *Anal. Chem.* **82,** 3104–3107 (2010).

Conclusions

The main result of this thesis is the design of integrated solution based approaches for assembling biochips of stable small aqueous compartments that, coupled with a confocal detection method, allow for the development of unprecedented devices for programming and studying few molecular and intermolecular events. Remarkable is the possibility to investigate on a chip the effect of the nanoscale confinement on the molecular and intermolecular behaviour as well as on the performance of molecular machines.

In particular, binding assays have been demonstrated by the CADRICS methodology allowing for investigating molecular diffusion parameters of biomolecules in scalable artificial "cellular-like" compartments. Protein binding assays have been executed in aqueous liquid phase and thus, they can be extended to more delicate proteins since no immobilization on solid supports is required. Reagent consumption per single droplet is minimal in comparison to recently reported methods, especially for assays conducted in aqueous liquid phase. Here it has been shown a proof-of-concept of this method by Alexa 647 dye and the model protein binding assay Biotin/Streptavidin. This approach can be easily generalized to multiplexed biomolecular assays in droplet microarrays by dispensing simultaneously, in multichannel formats, different aqueous inks, so that such CADRICS chip can screen a large number of different protein/ligand couples or different concentrations of the same protein/ligand couple.

On the other side, these findings can constitute an important basis for more elaborated investigations of the influence of volume confinement on protein binding and intermolecular interactions. In fact, it is possible to explore different conditions like surfactants of various molecular structures in order to stabilize aqueous compartments up to femtoliter fractions.

In this regard, it has been developed a novel printing approach to produce stable fL-scale aqueous droplets inside mineral oil in absence of electrolytes by sub-nozzle resolution Inkjet Printing. Inside such fL aqueous compartments, molecules spontaneously assemble in regular "ring-patterns" (hundreds of nm thick), in which solute-solvent and solvent driven solute-solute interactions are modified with respect to the bulk case as demonstrated by variation of fluorescence life time of environmental-sensitive molecules. The results of this study suggest that the design of aqueous fL droplets by a "spike-like" jetting waveform can lead to the assembly of a unique self-assembled aqueous confinement platform at a water-oil interface in presence of crowding agents that can outperform naturally occurring crowding phenomena in sub-cellular scale compartments. Remarkably, synergic effects of confinement and crowding lead to superior functionality of a DNA molecular machine. Understanding diffusion phenomena and binding or other intermolecular events in reduced size conditions and/or introducing higher viscosity ink formulations may allow recreating confinement and molecular crowding effects as is the situation of sub-cellular compartments in living cells.

Since for the first time few molecular events are detected on engineered artificial platforms, we believe that such methodologies are expected to have immediate impact in the fields of biochips, synthetic biology, drug screening and nanobiotechnology. A future perspective is the characterization of the enzymatic activity of a model system in crowded and confined environment. In particular, we want to investigate the effect of the annular confinement upon the CYP2E1-catalysed reaction rate. CYP2E1 is a cytochrome P450 phase I metabolism enzyme whose expression in mithocondria is specifically connected to physiopathological situations. Preliminary results have shown that the product reaction fluorescence in annular confinement leads to a lower lifetime because of the crowded environment and that fluorescence intensity increases in time reaching higher values for annular confinement in comparison to bulk case. Investigation of enzymatic kinetics leads to an unprecedented behaviour with respect to previous confinement reports. This can be interpreted, classically, as if annulus permits to eliminate uncompetitive inhibition, or more correctly, as if CYP2E1 is more concentrated in the annulus with respect to bulk, giving rise to an enhanced kinetics.

Another important result of this thesis is the set-up of a strategy for the fabrication of DNA biochips on solid support, such as modified glass surfaces, and flexible substrate, such as nylon, by Dip Pen Lithography. There has been developed strategies to deposit and anchor oligonucleotides on solid surfaces in form of ordered matrices. In particular, flexible supports such as nylon, are low-cost systems and are potentially ideal for the creation of systems disposable in the "Point-of-Care" diagnosis. The development of a solid knowledge-platform on these topics is important for the realization of a novel class of high-density, low-cost, and high-throughput “printed” devices and biochips on sub-micrometric and sub-cellular scale, for applications in biomedical and pharmacological field.

Acknowledgments

Giunta alla conclusione del dottorato di ricerca è arrivato il tempo di fare un bilancio relativo non solo a questi ultimi tre anni, ma al mio intero percorso universitario, che è partito nel 2007 e mi ha portato quotidianamente a vivere esperienze umane e lavorative di grande crescita.
Ho scelto volutamente di scrivere i ringraziamenti in italiano perché se da un alto ho voluto dare al lavoro di tesi un'impronta prettamente scientifica, dall'altro, in queste ultime pagine, c'è poco di "accademico", ci sono esperienze e sensazioni che ricorderò per tutta la vita.
Questi 10 anni li ho trascorsi divisa tra la mia famiglia, il mio ragazzo (da poco mio marito), i parenti e gli amici da un lato, l'università, le coinquiline, i colleghi e i professori dall'altro. Entrambi i fronti hanno fatto parte di me e mi hanno accompagnata per lungo tempo.
Ho vissuto tutti gli aspetti dell'essere studente universitario, da quelli meno piacevoli, come il timore prima di un esame, l'ansia di non essere all'altezza, la paura di non farcela e di deludere chi crede in te, a quelli più piacevoli come la condivisione con i colleghi delle paure di cui parlavo prima che di colpo sembravano svanire, la consapevolezza che se credi in te puoi farcela, la felicità per il buon esito di un esame e il senso di liberazione dopo aver raggiunto quegli obiettivi tanto agognati, la laurea triennale, la laurea magistrale, l'abilitazione professionale.
Comunque, l'esperienza che mi ha segnata più di tutte è stata proprio quella del dottorato, una sfida quotidiana nella quale sei chiamato a scontrarti ripetutamente con difficoltà, problemi da risolvere, ostacoli che sembrano insormontabili. Ma anche in questo caso, con dedizione, studio, applicazione e una buona dose di pazienza, ti rendi conto che nulla è impossibile e che forse troppo spesso sottovaluti le tue capacità. Ho imparato a non scoraggiarmi, a credere maggiormente in me stessa, ad affrontare con serenità i compiti che sono chiamata a svolgere, a rispettare il pensiero e i modi di fare delle persone che lavorano con me, a fare squadra. Questo non solo grazie alle mie capacità, ma anche al sostegno di coloro i quali hanno già affrontato questo stesso percorso e sono stati per me punto di riferimento e insegnanti speciali, i professori e i colleghi. Ho la certezza che tutto ciò che ho imparato in questi anni non mi sia servito solo in ambito universitario, ma sia stato per me fonte di crescita personale e costituisca un bagaglio di esperienze e lezioni di vita che mi aiuteranno ad affrontare le problematiche di ogni giorno.
A questo punto non posso non ringraziare il professore Bruno Pignataro, che è stato il mio tutor del dottorato e con cui ho iniziato il lavoro di ricerca già dalla tesi magistrale, grazie al quale mi è stato possibile accedere al mondo della ricerca scientifica. Il più grande insegnamento che ho appreso da lui è che bisogna essere ambiziosi, non mollare mai e puntare in alto, consapevoli dei limiti propri di un piccolo gruppo di ricerca, ma sempre pronti a migliorare e a lanciarsi in nuove sfide.
Un ringraziamento veramente sentito va al Dott. Giuseppe Arrabito. Non sarei giunta fino a qui senza il suo costante aiuto. Tutto ciò che ho imparato in questi tre anni lo devo soprattutto a lui, che

con il suo amore sconfinato per la ricerca e la sua costante dedizione nell'aiutare il prossimo, è riuscito a trasmettermi passione, conoscenze e buoni principi.
Un grazie alla mia collega Clara, collega e compagna di stanza, con la quale mi sono costantemente confrontata sostenendoci reciprocamente, e con la quale ho condiviso molti momenti di spensieratezza e allegria che hanno reso meno pesanti le lunghe giornate in laboratorio.
Non potrei non ringraziare le persone e i gruppi di ricerca con cui abbiamo collaborato in questi anni, senza i quali non si sarebbero ottenuti tali risultati. Perché, ad oggi, alla base della scienza e delle nuove ricerche di frontiera vi è soprattutto l'interdisciplinarità degli argomenti affrontati e, di conseguenza, la collaborazione fra gruppi con diverse e sviluppate competenze in vari ambiti scientifici e tecnologici.
Inizio con la professoressa Valeria Vetri, del gruppo di Biofisica dell'Università degli Studi di Palermo, che ha creduto in me fin da subito e per questo non smetterò mai di ringraziarla. Mi ha sempre incoraggiata anche quando io stessa credevo poco nelle mie capacità. Mi ha dato libero accesso ai suoi laboratori e alle strumentazioni, come se facessi parte del suo gruppo di ricerca. Da lei ho imparato davvero tanto; la sua grinta e passione per il lavoro non possono lasciare indifferenti e finiscono per coinvolgerti e stimolarti a migliorare.
Un altro sentito ringraziamento va al professore Maurizio Leone, facente parte dello stesso gruppo di Biofisica, la cui collaborazione con il gruppo del professore Pignataro va avanti da anni e ha portato ad importanti risultati in campo scientifico e tecnologico. La nascita presso l'Università di Palermo dell'ATeN Center, (Advanced Technologies Network Center), si deve soprattutto al loro impegno in collaborazione con altri professori dell'Università di Palermo. È proprio presso i laboratori presenti nel CHAB (Center for Human Health. Advanced Biotechologies), uno dei due poli dell'ATeN Center, che sono stati condotti gli esperimenti oggetto del presente lavoro di tesi.
Importante la collaborazione con il professore Francesco Ricci del dipartimento di Scienze e Tecnologie Chimiche dell'Università di Tor Vergata, e Sandro Cosconati del dipartimento di Scienze e Tecnologie Ambientali, Biologiche e Farmaceutiche dell'Università degli Studi della Campania Luigi Vanvitelli, nell'ambito del progetto PRIN 2012, dal titolo *Pursuing new horizons for cancer therapy through the integration of innovative high-throughput drug-screening and rational drug-discovery*, che ha portato allo sviluppo di nuove metodologie di stampa e detezione su microarray come la CADRICS. Inoltre, grazie al Prof. Francesco Ricci che ci ha fornito le macchine molecolari, DNA Molecular Beacon e Target, è stato possibile studiare il comportamento di tali elaborati sistemi biomolecolari in compartimenti da fL. In particolare, un grazie al Dott. Alessandro Porchetta, collaboratore del Prof. Ricci, per i continui confronti sulle tematiche relative alle macchine molecolari e su come impostare e portare avanti gli esperimenti impiegando questi sistemi.
Ringrazio anche il prof. Alessandro Desideri, del dipartimento di Biologia dell'università di Roma Tor Vergata, e la professoressa Birgitta Knudsen, dell'università di Aarhus in Danimarca, per aver

avviato un progetto così interessante nell'ambito della realizzazione di biochip su supporti low cost per la detezione di patologie quali la malaria, e di aver coinvolto l'università di Palermo in tale ambiziosa ricerca. In maniera analoga, un grosso ringraziamento va alla professoressa Patrizia Cancemi, del dipartimento di Scienze Biologiche di Palermo, senza la quale non sarebbe stato possibile svolgere le operazioni di detezione col microarray scanner e il crosslinker degli spot di DNA. Importante il contributo dato dal prof. Salvatore Feo, del dipartimento di Scienze Biologiche, sempre disponibile quando era necessario un confronto per quanto riguarda la metodologia da applicare per le reazioni di ibridazione sia sulla superficie di vetro che di nylon.

A questo punto sento il bisogno di ringraziare veramente tanto la mia famiglia, i miei genitori, le mie sorelle, i miei cognati e cognate, i miei suoceri, i nonni e gli zii, fino ad arrivare agli amici più stretti che mi hanno sempre sostenuta, fatta sentire importante, ma anche sopportata e supportata nei momenti di nervosismo e fragilità. Su di loro avrei tanto da dire, ma non sarebbe mai abbastanza per tutto quello che hanno fatto e continuano a fare per me. Non siete soltanto voi ad essere orgogliosi di me, sono soprattutto io ad esserlo di voi.

Infine, non posso che ringraziare te Angelo, a cui ho dedicato questa tesi di dottorato.

Per ringraziarti non so davvero da dove cominciare, se non dal dedicarti il GRAZIE più importante, grazie per tutto quello che hai fatto per me in questi meravigliosi 11 anni, grazie per tutto ciò che sei e che rappresenti per me.

Concludo questa lunga pagina di ringraziamenti con la speranza di continuare questo percorso nell'ambito della ricerca scientifica, consapevole del fatto che qualunque sarà la mia prossima esperienza lavorativa avrò con me un bagaglio ricco di competenze, capacità, ambizioni, oltre che di principi e valori umani.